UNIVERSITY OF CALIFORNIA, MERCED

Determination of Temperature and Concentration from Radiometric Measurements in Combustion Systems

by

Tao Ren

A dissertation submitted in partial satisfaction of the
requirements for the degree of
Doctor of Philosophy

in

Mechanical Engineering

Committee in charge:
Professor Michael F. Modest, Chair
Professor Gerardo C. Diaz
Professor Yanbao Ma
Professor Roummel F. Marcia

Spring 2015

The dissertation of Tao Ren is approved:

Michael F. Modest, Chair	Date
Gerardo C. Diaz	Date
Yanbao Ma	Date
Roummel F. Marcia	Date

University of California, Merced

To my parents

Acknowledgments

First of all, I would like to sincerely thank my advisor Professor Michael F. Modest. Without his constant guidance over the years, this project would not have been possible. I was inspired and enlightened by his profound knowledge, acute insights, deep understanding of the philosophy of research, sense of humor and most importantly, meticulous attention to details.

I would like to thank my dissertation committee, Professor Gerardo C. Diaz and Professor Yanbao Ma from Mechanical Engineering, Professor Roummel F. Marcia form Applied Mathematics for their time, insightful comments and constructive guidance that significantly improved this dissertation.

I also would like to express my appreciation to my previous and current labmates and colleagues at UC Merced. Dr. Jian Cai and Dr. Shenghui Lei offered me valuable advices when I began my research and life at Merced. The wonderful two years with previous labmates Todd A. Reeder are certainly memorable. I also want to thank my current colleagues Dr. Somesh Roy, Mr. Wenjun Ge and Mr. Chaojun Wang for all the collaborations and helps.

For the past few years back in China, I have been so lucky to work with great scholars both at XJTU and HUST. As my bachelor thesis advisor, Professor Yaling He (XJTU) and Master thesis advisor, Professor Shuhong Huang (HUST), they both inspired me with their sense of responsibility, rigorous scientific spirit; they led me to the journey of scientific research. Special thanks goes to Professor Huaichun Zhou at Tsinghua University, without his recommendation, I would not have a chance to know Dr. Modest and accomplish all of this in the past four years.

The support from National Science Foundation Grant No. CBET-0966627 is gratefully acknowledged. I also would like to thank the numerous fellowship awards from UC Merced, financial support and training from being research and teaching assistant at UC Merced.

Last but not least I want to express my gratitude to my parents. Both of them came from impoverished backgrounds and neither of them have been to college. They sacrificed a lot to raise me with a sense of responsibility, a deep understanding the meaning of hard work and a optimal attitude for appreciation of life. They are always being a constant source of love and encouragement for me.

Curriculum Vitae

Education

- Ph.D. in Mechanical Engineering. University of California, Merced (UCM). Merced, CA, USA. Aug. 2011-May 2015
- M.S. in Thermal Engineering. Huazhong University of Science and Technology (HUST). Wuhan, Hubei, China. Sept. 2008-Mar. 2011
- B.S. in Thermal and Power Engineering. Xi'an Jiaotong University (XJTU). Xi'an, Shaanxi, China. Sept. 2004-July 2008

Publications

1. T. Ren and M. F. Modest. Optical determination of temperature and species concentration for homogeneous turbulent gas medium. submitted to *International Journal of Heat and Mass Transfer*
2. T. Ren and M. F. Modest. Temperature profile inversion from carbon-dioxide spectral intensities through Tikhonov regularization. *Journal of Thermophysics and Heat Transfer*, in press
3. T. Ren, M. F. Modest, A. Fateev, and S. Clausen. An inverse radiation model for optical determination of temperature and species concentration: development and validation. *Journal of Quantitative Spectroscopy and Radiative Transfer*, 151(0):198209, 2015
4. X. Y. Zhao, D. C. Haworth, T. Ren, and M. F. Modest. A transported probability density function/photon Monte Carlo method for high-temperature oxy-natural gas combustion with spectral gas and wall radiation. *Combustion Theory and Modelling*, 17(2):354381, 2013
5. T. Ren and M. F. Modest. Hybrid wavenumber selection scheme for line-by-line photon Monte Carlo simulations in high-temperature gases. *Journal of Heat Transfer*, 135(8):084501-084501, 2013

Honors

Graduate Dean's Dissertation Year Fellowship, UC Merced	2015
Mechanical Engineering Bobcat Award, UC Merced	2014
MEAM Graduate Fellowship Award, UC Merced	2013
MEAM Travel Fellowship Award, UC Merced	2013
UC Mercd Graduate Summer Fellowship Award, UC Merced	2012

Contents

List of Figures

List of Tables

Nomenclature and Abbreviations

A	truncating or apodizing function
$\mathbf{a}$	state vector for Kalman filter
$\mathbf{B}$	gradient vector
F	objective function, state transition matrix for Kalman filter
$\mathcal{F}$	Fourier transform operator
f	nonlinear function
g	nonlinear function
G	correction number
h	elements of Hessian matrix
$\mathbf{H}$	Hessian matrix
I	spectral intensity, W/cm^2 sr cm^{-1}
$\mathbf{I}$	identity matrix
$\mathbf{K}$	Kalman's gain matrix
L	gas path length, cm
N	number of data for one case
$\mathbf{n}$	measurment noise
P	total pressure, bar
$\mathbf{P}$	covariance matrix for Kalman filter
$\mathbf{Q}$	covariance matrix for Kalman filter
$\mathbf{R}$	smoothing matrix, covariance matrix for Kalman filter
Res	FTIR resolution, cm^{-1}
PxL	pressure path length, bar cm
s	length along path, cm
$\mathbf{s}$	input vector for Kalman filter
T	temperature, K
t	total time interval, s
t_e	turbulence integral time scale, s
u	turbulent scalar
U	standard deviation for the turbulent scalar
$\mathbf{v}$	processing noise
x	concentration by volume
Y	measured transmissivity/intensity data
z	mirror offset, cm

$\vec{z}$	parameter vector

Greek Symbols

β	percentage of turbulence fluctuation
γ	regularization term of objective function
ϵ	residual for intensity, W/cm^2 sr cm^{-1}
η	wavenumber, cm^{-1}
θ	turbulence effects from spatial correction
κ	absorption coefficient, cm^{-1}
κ_P	pressure-based Planck-mean absorption coefficient, (cm bar)$^{-1}$
λ	regularization parameter
μ	scaling factor for Levenberg-Marquardt method
ρ	residual term of objective function
σ	experimental uncertainty
τ	transmissivity
χ	turbulence optical thickness
Γ	instrument line shape (ILS), pixel response function (PRF)
Δ	FTIR retardation, cm
Λ	turbulence integral length scale, cm

Subscripts

b	Blackbody
c	convolution
i, n	spacial index
j, m	spectral index

Abbreviations

FTIR	Fourier transform infrared spectrometer
ILF	instrument line function
LBL	line-by-line
LIF	laser-induced fluorescence
OTFA	optically thin fluctuation assumption
PDF	probability density function
PRF	pixel response function
rms	root mean square value
SNR	signal-to-noise ratio
TRI	turbulence-radiation interactions

Abstract

Determination of Temperature and Concentration from Radiometric Measurements
in Combustion System
by
Tao Ren
Doctor of Philosophy
in
Mechanical Engineering
University of California, Merced
Professor Michael F. Modest, Chair

Despite that combustion diagnostics have reached high levels of refinement, it remains difficult to make quantitatively accurate nonintrusive measurements of temperature and species concentrations in realistic combustion environments. The goal of the present study is to develop nonintrusive spectral radiation tools to allow efficient high-fidelity determination of temperature and species concentrations in laminar and turbulent combustion systems. Temperature and concentrations are deduced from medium-to-coarse resolution measurements of spectral transmissivity and emitted intensity for homogeneous gas media, nonhomogeneous gas media and turbulent systems considering the turbulence radiation interaction (TRI).

For a homogeneous gas medium, by minimizing the differences between measured and predicted transmissivity spectra, an inverse radiation model is developed to retrieve temperature and species concentrations simultaneously using the the Levenberg-Marquardt optimization method. This model has been validated by experimental measurements. The developed inverse radiation model is used to determine the optimal wavenumber range and resolution by retrieving temperature and species concentrations from a homogeneous gas column for a wide range of temperatures and concentrations. Multiple factors, including spectral region, spectral resolution, temperature and concentration range, and susceptibility to systematic error and random error have been considered. Results are obtained for homogeneous mixtures containing CO_2, H_2O or CO with N_2.

In nonhomogeneous gas media, transmissvities are not sensitive to temperature and concentration distributions, making it impossible to reconstruct temperature and species concentrations fields from transmissivity spectra. Another inverse calculation model is developed using measured line-of-sight emitted spectral intensity data to retrieve temperature profiles. Because intensity spectra are also not sensitive to concentration profiles, this model can only deduce the temperature profile together with an average concentration. Due to the ill-posedness of this inverse problem, additional conditions or criteria are needed to be imposed to determine the most realistic solution. Most regularization methods transform an ill-posed inverse problem into a well-behaved one by adding auxiliary information based on desired or assumed characteristics. Tikhonov regularization imposes smoothness to the solution by adding a regularization term. Tikhonov regularization has been shown to be suitable for solving these ill-posed problems, but it is difficult to select an appropriate regularization parameter, especially for nonlinear problems. A new regularization selection

method based on the theory of the discrepancy principle and the L-curve criterion is proposed and shows good generality for different temperature profile inversions. Several types of temperature profiles are retrieved accurately using this method.

For a turbulent system, the nonlinear interaction between turbulence and radiation has profound effects and cannot be neglected when developing inverse radiation tools. In the presence of TRI, temperature and concentration can never be measured directly. An inverse radiation model considering how turbulence and radiation interact along the detector's line-of-sight has been developed to deduce time-averaged and root-mean-square (rms) values of temperature and concentrations as well as the turbulent length scale from the time-averaged transmissivity and its rms spectrum for a single turbulent gas as well as a turbulent gas mixture.

Chapter 1

Introduction

1.1 Background

Advanced optical diagnostics and multiscale simulation tools will play central roles in the development of next-generation clean and efficient combustion systems, as well as upcoming high-temperature alternative energy applications. High-fidelity experimental diagnostics will be required to validate advanced numerical models, and both are needed to guide the move toward nonpetroleum-derived fuels, higher operating temperature and pressures, etc. Although combustion diagnostics have reached a high level of refinement, it remains difficult to make quantitatively accurate measurements of species concentrations, soot, and temperature in realistic combustion environments. In turbulent reacting flows turbulence-radiation interactions (TRI) significantly alter radiometric signals, effectively making it impossible to "measure" temperature and concentrations with today's tools. To validate reacting flow codes it is standard practice to compare temperature and concentration "measurements" with values predicted from the codes.

As long as there has been research in the field of combustion and other applications involving heat transfer, researchers have attempted to measure temperature, reaction rates, species concentrations, heat fluxes, etc., in situ. Until recently, this meant using intrusive techniques that invariably altered the flow and heat transfer fields, such as thermocouples for temperature, gas chromatographs for concentrations, etc. During the past few decades many nonintrusive optical techniques have been developed. For example, single- and multi-color pyrometers have been employed to measure temperature [1, 2], Rayleigh and Raman scattering are used as powerful combustion diagnostic tools for laboratory flames [3–9], laser-induced fluorescence (LIF) was used to determine concentration and/or temperature of certain gaseous species [10–13], extinction of a laser beam was employed to determine soot volume fractions [14–16], etc.

The optical pyrometer infers temperatures based on the received thermal radiation from a target and comparing it with the blackbody emission, which has been used for flame [17] and coal particle [18] temperature measurements. However, in these applications, pyrometer measurements do not reflect the temperature at any location, nor the average temperature along the line-of-sight because of nonlinear dependence of radiation emission on temperature [19]. In a turbulent combustion system, the correlation of temperature and species concentration has to be determined to complete the turbulent information, but previous pyrometers measurements were mainly restricted to time-

averaged “point” measurements of temperature [20]. Laser-based techniques, such as Raman scattering, Rayleigh scattering and laser-induced fluorescence, are ideal for combustion diagnostics, and are particularly useful for studying turbulent processes due to their capability of conducting spatially and temporally resolved measurements [21, 22]. These methods are able to provide nonintrusive, in situ measurements with spatial resolution of less than 0.1 mm and temporal resolution of the order of 10 ns [20]. However, Raman and Rayleigh scattering measurements require a high power laser source and clean laboratory conditions, due to the low sensitivity of these method, which limits the applications to laboratory measurements. The uncertainties in temperature measurement utilizing Raman spectroscopy were discussed by Laplant et al. [23]. The range and accuracy for Raman scattering are approximately 20–2230 °C and 7%, respectively. Laser-induced fluorescence is the optical emission from atoms or molecules that have been excited to higher energy levels by absorption of laser radiation. The level of fluorescence is known to vary with the concentration or the temperature and several other parameters. It is used to measure concentration and local temperature in flames by exciting molecules and atoms in specific species, for example, NO, SiO, OH, N_2, and O_2 [24]. This method also requires a laser source with high average power. It was extensively used for combustion diagnostics, but mainly for laboratory flames [3–9]. The range of application of LIF is between 200 K and 3000 K and the accuracy of the method is approximately 5% at 2000 K [24].

Among the numerous combustion diagnostic tools, the infrared emission and transmission spectroscopy techniques are especially attractive due to strong rotational or vibrational transitions of combustion species in the infrared region, separable and specific transitional bands for different species and simplicity of emission and transmission measurements [25–27]. The spectra from a flame or combustion chamber may be recored with line-of-sight emission or transmission spectroscopy, and temperature and species concentrations can be retrieved along the line-of-sight. With proper tomography techniques, while the combustion fields can be reconstructed [28–31]. In order to evaluate the temperature and species concentration, the measured spectrum was fitted to a theoretical model, which involves information of molecular parameters, such as transitional line strengths, shapes and widths. A number of molecular spectroscopic databases [32–34] are available for infrared spectra predictions, which makes this method even more attractive. However, very few studies has been done for turbulent combustion diagnostics using infrared emission and transmission spectroscopy due to the difficulty of predicting turbulent radiation accounts for nonlinear effects from TRI.

1.1.1 Emission and Transmission Spectroscopy

Emission and/or transmission spectroscopy of a combustion gas can reveal its temperature and concentration, but very few researchers [35–37] have done preliminary studies exploiting the dependence of spectral absorption coefficients of combustion gases on temperature and species concentration. The spectral intensity along a line-of-sight within a nonscattering medium, as seen by a detector at $x = L$, as shown in Fig. 1.1, is given by [38]

$$I_\eta = I_{0\eta} e^{-\int_0^L \kappa_\eta ds} + \int_0^L \kappa_\eta I_{b\eta} e^{-\int_s^L \kappa_\eta ds'} ds \tag{1.1}$$

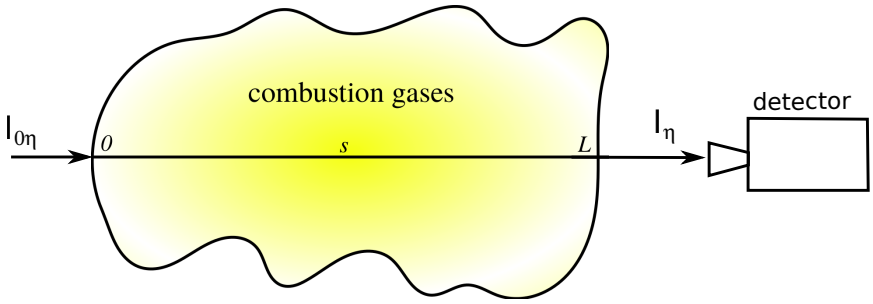

Figure 1.1: Schematic diagram of the physical system

where κ_η is the spectral absorption coefficient at wavenumber η (which depends on temperature and concentration), $I_{b\eta}$ is the local blackbody intensity of the medium and $I_{0\eta}$ is external irradiation entering the gas column $0 \leq s \leq L$ at $s = 0$. The column transmissivity is defined as

$$\tau_\eta(s \to L) = e^{-\int_s^L \kappa_\eta ds'} \tag{1.2}$$

Eq. (1.1) simplifies to

$$I_\eta = I_{0\eta}\tau_\eta(0 \to L) + \int_0^L \kappa_\eta I_{b\eta} \frac{d\tau_\eta(s \to L)}{ds} ds \tag{1.3}$$

For a homogeneous column

$$I_\eta = I_{0\eta}\tau_\eta(0 \to L) + I_{b\eta}\left(1 - \tau_\eta(0 \to L)\right) \tag{1.4}$$

Equation (1.4) can be rewritten as

$$\tau_\eta(0 \to L) = \frac{I_\eta - I_{b\eta}\left(1 - \tau_\eta(0 \to L)\right)}{I_{0\eta}} \tag{1.5}$$

Equations (1.4) and (1.5) allow two measurements, which are emission from the gaseous medium I_η and are transmission of external irradiation τ_η, and they are depend on temperature and concentration. For a system which has n radiating species, including temperature, there are $n + 1$ unknowns that need to be determined from transmission or emission measurements. In principle, emission measurements, transmission measurements, or both, can be conducted at infinitely many different spectral locations to parametrically resolved temperature and concentration fields.

Griffith et al. [39, 40] were the first to recognize that measurements of the transmission or emission of rotational spectral lines of a gas can reveal its temperature. In their experiment [39] they measured the spectral transmissivity of a CO-air mixture contained in a heated cell. Using an FTIR spectrometer at moderate (0.5 cm^{-1}) resolution they fit their spectra to theoretically calculated ones, corrected for the instrument line function [41], using nonlinear least-square fits. With cell conditions ranging from 90 to 190 °C and various pressures, their deduced temperatures showed an

averaged error of 1.8 °C compared with thermocouple measurements, but with maximum errors of up to 20 °C at higher temperatures, due to a lack of precise knowledge of line width dependence on temperature. In their later experiment [39], they used pure CO_2 and similar cell conditions as for the CO experiments, but a finer resolution of 0.29 cm^{-1} and a nonlinear least-square fit for the integrated transmission minima. By using only high signal-to-noise spectra and many spectral scans they extracted temperatures to within a maximum departure of about 2.0 °C from thermocouple measurements. Disadvantages of the method are unacceptably long data acquisition times (1 hr), transmission (as opposed to simpler emission) measurements, and susceptibility to noise.

The first ones to apply FTIR spectroscopy to an actual laminar diffusion flame appear to have been Best et al. [42, 43], who combined tomography and FTIR transmission and emission spectra to extract temperature, concentration and soot volume fraction fields. Not much detail was given, except that low resolution (32 cm^{-1}) scans were used, an axisymmetric field was assumed, and temperature uncertainty of ± 50 °C was claimed (no secondary technique for validation/comparison was employed). The first ones to use the new high-resolution spectroscopic database HITRAN [44–47] appear to have been Hilton et al. [48, 49], who used high-resolution spectroscopy (0.25 cm^{-1}) to study a smoke stack plume and laboratory-scale methane flame [48], as well as a gas turbine exhaust [49]. Little explanation was given on whether or how temperatures were determined for these presumably turbulent conditions; however, species concentration profiles were extracted by observing individual lines of different species, and by scanning the detector across the flame, which was assumed to be axisymmetric. No errors or uncertainties were given.

The group around Lallemand used both high-resolution [50] and medium-resolution [51] synthetic axisymmetric emission spectra to reconstruct temperature and concentration profiles. In [50] reconstruction was done by ratioing two isolated CO lines, using several inversion schemes that exploit the axisymmetric geometry. As Griffiths [39] before them, they noticed that this approach is very sensitive to experimental noise. In their medium-resolution work they attempted to recover temperature and CO_2 concentration values from axisymmetric synthetic spectra as well as a laminar premixed flame, with thermocouple data for the latter for comparison. The CO_2 4.3 μm band was used, which may be less than ideal because of its high opacity. However, for this small, optically thin flame the recovered temperature followed measured values qualitatively well (to about ± 100 °C)

FTIR emission spectroscopy to deduce temperature and species concentrations in high pressure solid propellant flames was attempted by Thynell et al. [52, 53], also using medium-resolution measurements (2 cm^{-1}). Some attempt was made to recover limited nonisothermality in a "mixing region." Finally, Soufiani et al. [26] did a detailed study of FTIR emission spectroscopy, using high-resolution and medium-resolution data. The spectral data were downgraded to a coarse resolution of 25 cm^{-1} and used to deduce temperatures as well as water vapor and carbon dioxide concentration via a least-squares technique; CO concentration was found by rotioing individual spectral lines similar to Lallemand's work [50]. Temperature profiles were obtained from the downgraded data and were found to be within ± 75 °C of experiment. They were also able to retrieve temperatures from the high-resolution CO lines, but again noted a strong susceptibility to noise.

All multispectral diagnostic techniques discussed so far have employed FTIR spectroscopy. Such devices can provide spectral scans in a wide range of resolutions and of great accuracy, but to obtain a spectrally resolved measurements with good signal-to-noise ratio takes 10s of seconds

for low-resolution narrow-band scans to hours for high-resolution full-spectrum measurements. As such the application of FTIR is limited to very stable (laminar) systems, while FTIR spectroscopy has been applied to turbulent plumes [48, 49] to measure mean temperature, it is very questionable that this is possible (due to the relatively slow modulation of the FTIR signal). Very few attempts have been made to date to obtain time-resolved multi-spectral signals from turbulent systems, because–to obtain snapshots of a turbulent flowfield–exposure time must be of order of 0.1ms or less. Richardson et al. [54, 55] were perhaps the first to attempt such measurements,using a 32-elements InSb linear array detector fitted with a grating monochromator. Their device was able to collect a 32-spectrum signal over 160 μs, storing 250 samples for each detector element. This resulted in an equivalent FTIR resolution of 32 cm^{-1} when collecting a sample of 250 cm^{-1} with a signal-to-noise ratio of about 50. No transient sample was considered. Their improved second device was able to hold 2048 full spectra collected every 16 μs. No reconstruction of temperature, etc., was attempted. Mid-infrared radiation measurements from a turbulent nonpremixed/partially premixed jet flame and plume were made by Gore et al. [56, 57] with a high speed infrared camera and an InSb detector. At each location, 6400 images were collected to ensure that the turbulence statistic of the radiation intensity were converged. Three bandpass filters (2.58 ± 0.03 μm, 2.77 ± 0.12 μm, 4.34 ± 0.1 μm) were used to measure the radiation from water vapor and from carbon dioxide. A spectrally integrated signal over the band-pass filter was measured. Most recently, an imaging Fourier-transform spectrometer [58] was used to probe a turbulent nonpremixed jet flame. Such device is a hyperspectral imager that combines a Michelson interferometer with a staring (distinct from scanning) infrared focal-plane array. It was claimed that the high-speed broadband imagery comprising each interferometric measurement contains information about the fluctuation statistics.

In order to resolve turbulent fluctuations, a fast spectrometer is required. Potential commercial spectrometers include rapid-scan FTIR, ultra-rapid-scan FTIR, step-scan FTIR, and fast infrared array spectrometer. In rapid-scan FTIR, by increasing the speed of the moving mirror, the fast FTIR can achieve approximately 110 spectra per second at low (16 cm^{-1}) spectral resolutions. The scan rate is limited by the time required to reverse the direction of the moving mirror. Rapid-scan FTIR is thus fundamentally limited in the temporal resolution that can be achieved. Various interferometer modifications have been suggested for further increasing scanning speed by switching from translation motion of the mirror to rotational movement. A design introduced by Manning and co-workers in 1999 [59] includes a rotating highly polished aluminum disk as the rotating optical element. This so-called ultra-rapid scan FTIR can achieve high speeds of 1000 spectra per second. However, obtaining one spectrum in one (ultra-rapid scan) or tens (rapid-scan) of milliseconds is not fast enough for resolving turbulent fluctuations. By contrast with rapid-scan FTIR and ultra-rapid-scan FTIR, the step-scan technique allows monitoring of temporal progress of very fast events (nanoseconds). However, step-scan spectrometers obtain high temporal resolution in a rather different manner: spectral information can only be obtained for highly-repeatable events over a long period of time [60], i.e., step-scan cannot be used to probe chaotic turbulence spectra. The fast infrared array spectrometer now available as ES200 (previous model ES100 [61]) from Spectraline is a fast imaging spectrometer that can provide the spectral radiation intensity in the mid-IR region. It does not require reproducible sampling of data for time-resolved data acquisition. The useful spectral range of the ES200 is from 1.3 μm to 4.8 μm. The radiation intensity that is incident on the entrance slit is split into its spectral components using a refractive element. 256 narrow

bands within the spectral range are obtained, using a 256-element linear PbSe array detector, and its response at room temperature in the 1.3 μm to 4.8 μm spectral region is better than 2μs. This essentially freezes the process being studied, with each spectrum being obtained at a speed of 10280 Hz. The ES200 and its previous model ES100 have been extensively used to obtain radiation spectra in fully turbulent flames [62–64] and show good capability for resolving turbulent fluctuations. Later measurements, carried out with this high-speed infrared array spectrometer, provide a plethora of data for the otherwise well-documented Sandia Workshop flames [65, 66], and for a sooty ethylene air diffusion flame [67], even though many simplifying assumptions were made in the interpretation of those data.

1.1.2 Infrared Spectral Bands for Combustion Gases

The rovibrational bands of combustion gases in the infrared lend themselves to spectroscopic measurements. Depending on the temperature of the external source (for transmission measurements) or the combustion gas (for emission measurements), the wavelengths from about 0.6 μm to 12 μm are of interest. However, because of transmission limits of optical windows, through which combustion systems must be monitored, and limited detector ranges, wavelengths beyond 6 μm tend to be less useful. Even for the wavelength range from 0.6 μm – 6 μm, the spectra for combustion gases contain mostly "spectral windows," since only a few rovibrational bands exist. As an example, Fig. 1.2 shows the line-by-line (LBL) absorption coefficient spectrum for three different combustion species at total pressure of 1 bar, temperature of 1000 K and concentration of 10%.

The LBL absorption coefficient exhibits the precise line shape of the the absorption coefficient. While the fine resolution has a very distinct structure, which can be exploited for inversion, this fine structure is subject to theoretical uncertainty, such as calculated values for line strengths, shapes and widths. Fine resolution is also more susceptible to experimental noise, and requires large collection times. Figure 1.3 shows the smoother averaged shapes of absorption coefficients for the CO_2 4.3 μm and 2.7 μm spectral bands at three different temperatures. These coarse-resolution spectra with diminishing structures of line shapes still show very distinct temperature trends, which make reconstruction of temperature possible.

However, what can be actually measured is not absorption coefficient but emission or transmission spectra. As shown in Fig.1.4 for the CO_2 4.3 μm band at 1000 K and a concentration of 10% (with 90% N_2), for these conditions the emitted intensity reaches blackbody (BB) emission (at the same temperature) for a large part of the spectrum, similarly, a large part of the transmissivity spectrum tends toward zero. In the presence of high concentrations the CO_2 4.3 μm band becomes highly saturated for a homogeneous gas medium, which masks some of the spectral information, making reconstruction of temperature less accurate and less efficient. While for a nonhomogeneous gas medium, the saturated part of the spectrum provides precise information at the boundaries and with a wide band, temperature profiles can be retrieved more accurate. Similar pictures are shown for the CO_2 2.7 μm band, the H_2O 2.7 μm band and the CO 4.7 μm band in Figs. 1.5, 1.6 and 1.7, respectively. These are relatively strong bands for the combustion species and are possible candidates for emission and/or transmission spectroscopy studies.

A number of gas property databases are available for infrared spectrum predictions, such as HITRAN 2008 [32] and HITEMP 2010 [33], which contain LBL information for many gas species.

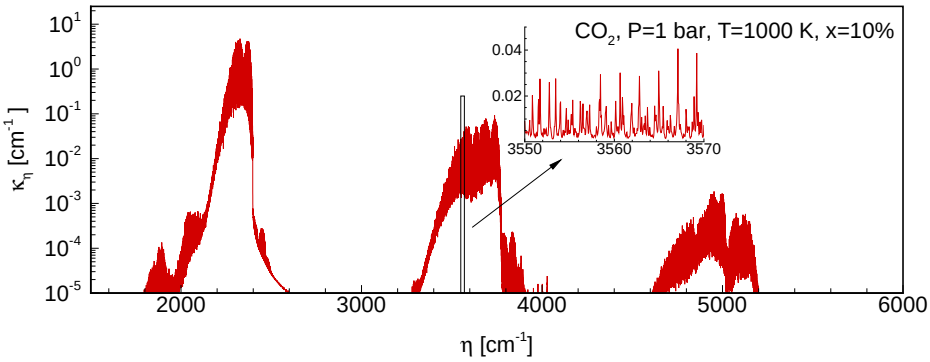

(a) Absorption coefficient spectrum for CO_2

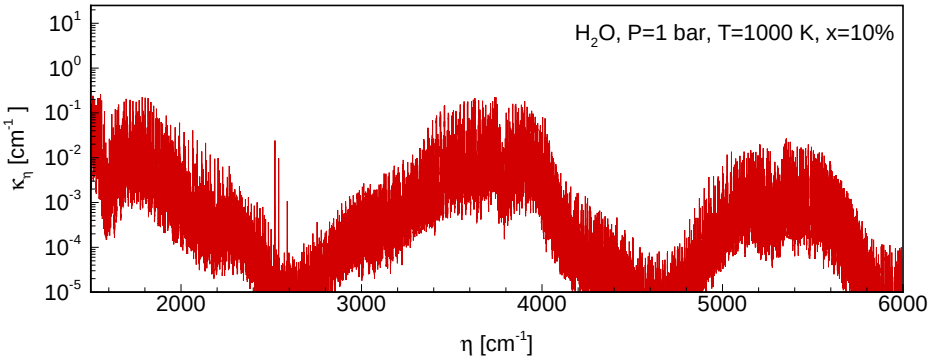

(b) Absorption coefficient spectrum for H_2O

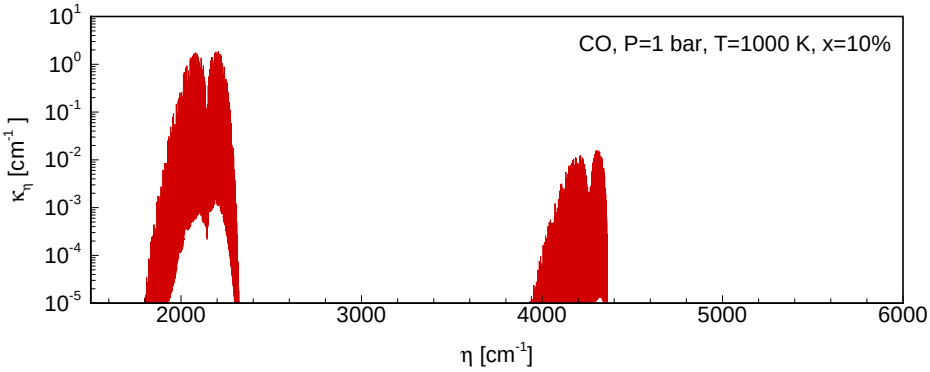

(c) Absorption coefficient spectrum for CO

Figure 1.2: Spectral absorption coefficients for combustion gases

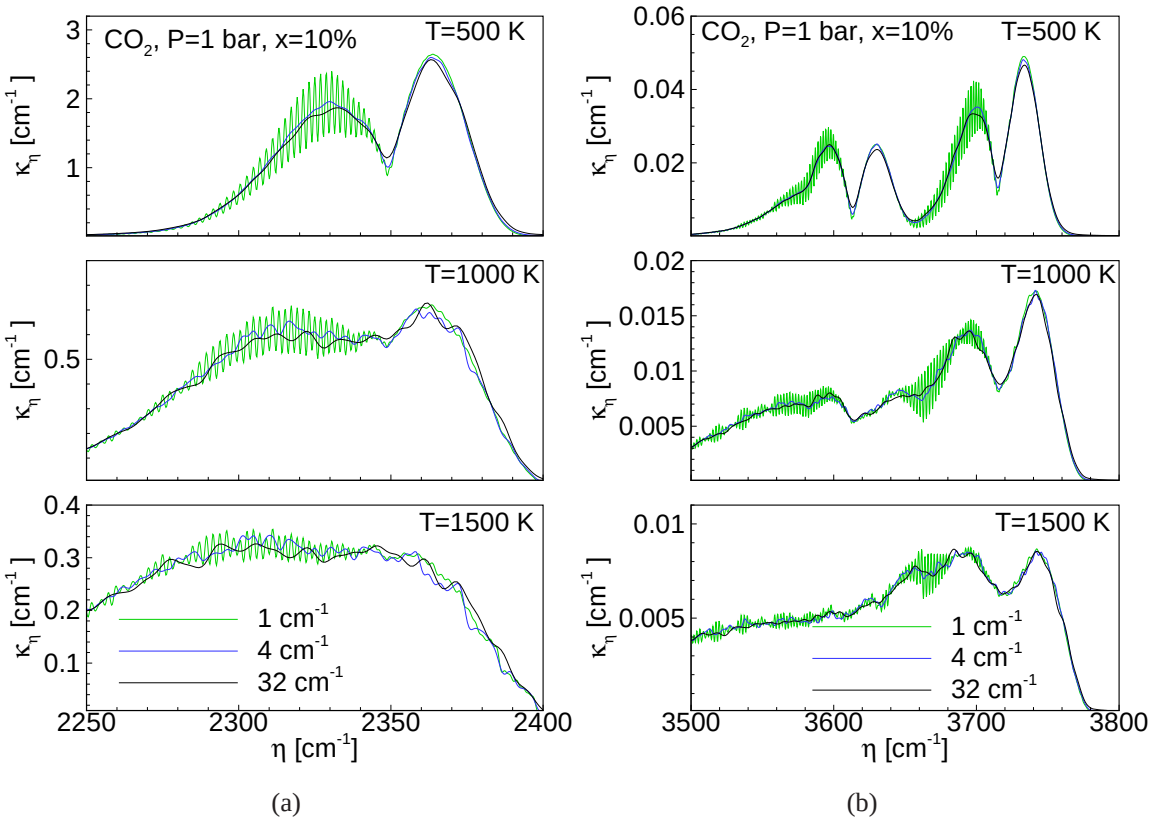

Figure 1.3: Spectral absorption coefficient at varying resolutions and temperatures: (a) the CO_2 4.3 μm band; (b) the CO_2 2.7 μm band.

HITEMP 2010 is limited to only 5 species (CO_2, H_2O, CO, NO and OH), but contains data for "hot lines," which become active at high temperature. In the updated HITEMP 2010 CO_2 parameters were calculated from CDSD-1000 [68]. The database was extensively tested against measured medium-resolution spectra of CO_2 [69, 70] for the 15, 4.3, 2.7, and 2.0 μm bands at temperatures of 300, 600, 1000, 1300, and 1550 K and measured high-resolution spectra of CO_2 in the 15, 4.3 and 2.7 μm bands at temperatures up to 1773 K [71]. The database was also tested against measured medium-resolution spectra of H_2O [72] for the 6.3, 2.7 and 1.8 μm bands at temperatures of 600, 1000, and 1550 K and measured high-resolution spectra of H_2O in the 2.7 and 1.8 μm bands at temperatures up to 1673 K [73]. Good agreement between measured and calculated spectra was found.

1.1.3 Inverse Analysis of Radiometric Data

Optical diagnostics based on radiometric measurements is concerned with reconstructing the spatial distribution of temperature, species concentrations and other parameters inside absorbing

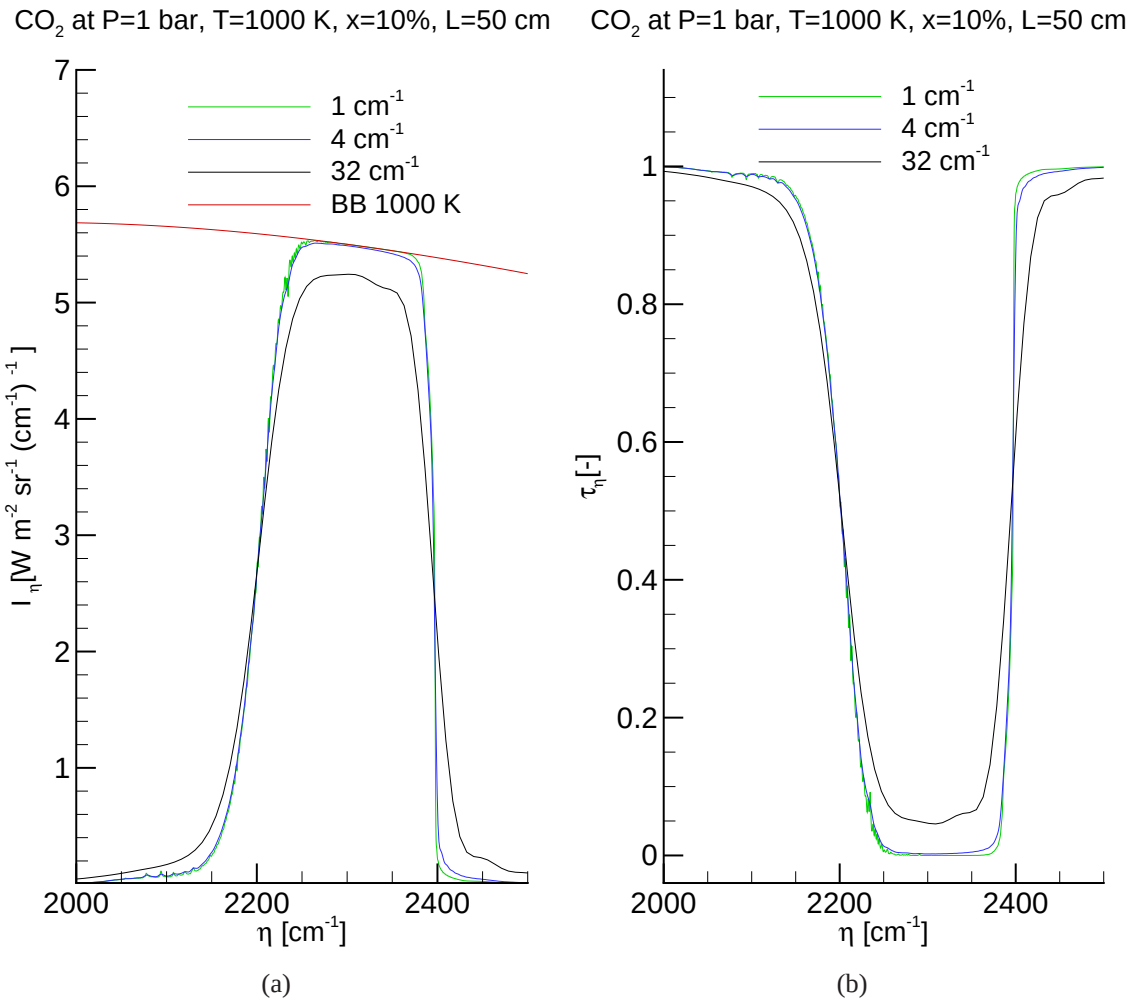

Figure 1.4: Emitted spectral intensity spectrum and transmissivity spectrum for the CO_2 4.3 μm band at varying resolutions of a 50 cm long CO_2 gas column at temperature of 1000 K and concentration of 10%: (a) emitted spectral intensity; (b) transmissivity.

combustion gases. These retrieval techniques based on radiative measurements are known as inverse radiative heat transfer analyses [38]. First, a forward model is required to predict the detector reading as a function of the retrieval parameters of the system. Second, an objective function is formulated which represents the difference between the predicted and measured data. And third, an inverse model is used to provide updated system parameters by minimization of the objective function [74, 75]. The most robust methods for minimizing the objective function have proved to be gradient-based [76]. Steepest descent is the simplest method and can guarantee convergence, but it is known to have a very slow convergence rate [77]. Quasi-Newton methods are alternatives

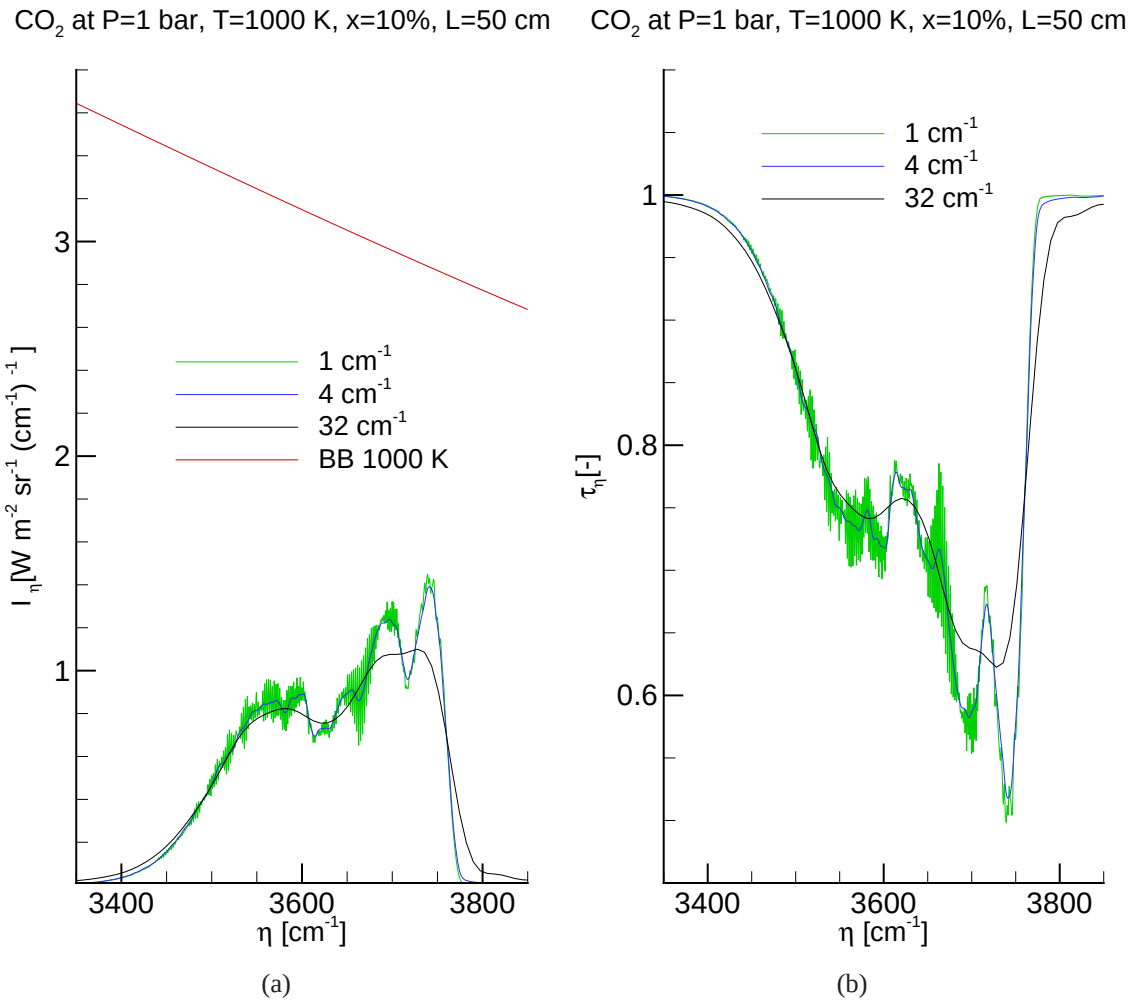

Figure 1.5: Emitted spectral intensity spectrum and transmissivity spectrum for the CO_2 2.7 μm band at varying resolutions of a 50 cm long CO_2 gas column at temperature of 1000 K and concentration of 10%: (a) emitted spectral intensity; (b) transmissivity.

to Newton's method, which are used to find local minima of the objective functions avoiding to calculate the exact Hessian matrix [38, 77], which can be extremely expensive sometimes. In this method, at each iteration the objective function is approximated by a quadratic function and takes a step toward the minimum of the quadratic function. If the objective function is quadratic or near-quadratic, the local minimum can be found in very few steps. One of the disadvantages is that this method does not guarantee convergence. Unlike the steepest descent method, the search direction for two searching steps may happen to be parallel. The idea of conjugate gradient method is to keep memory of the previous direction and pick a next search direction orthogonal to all previous ones

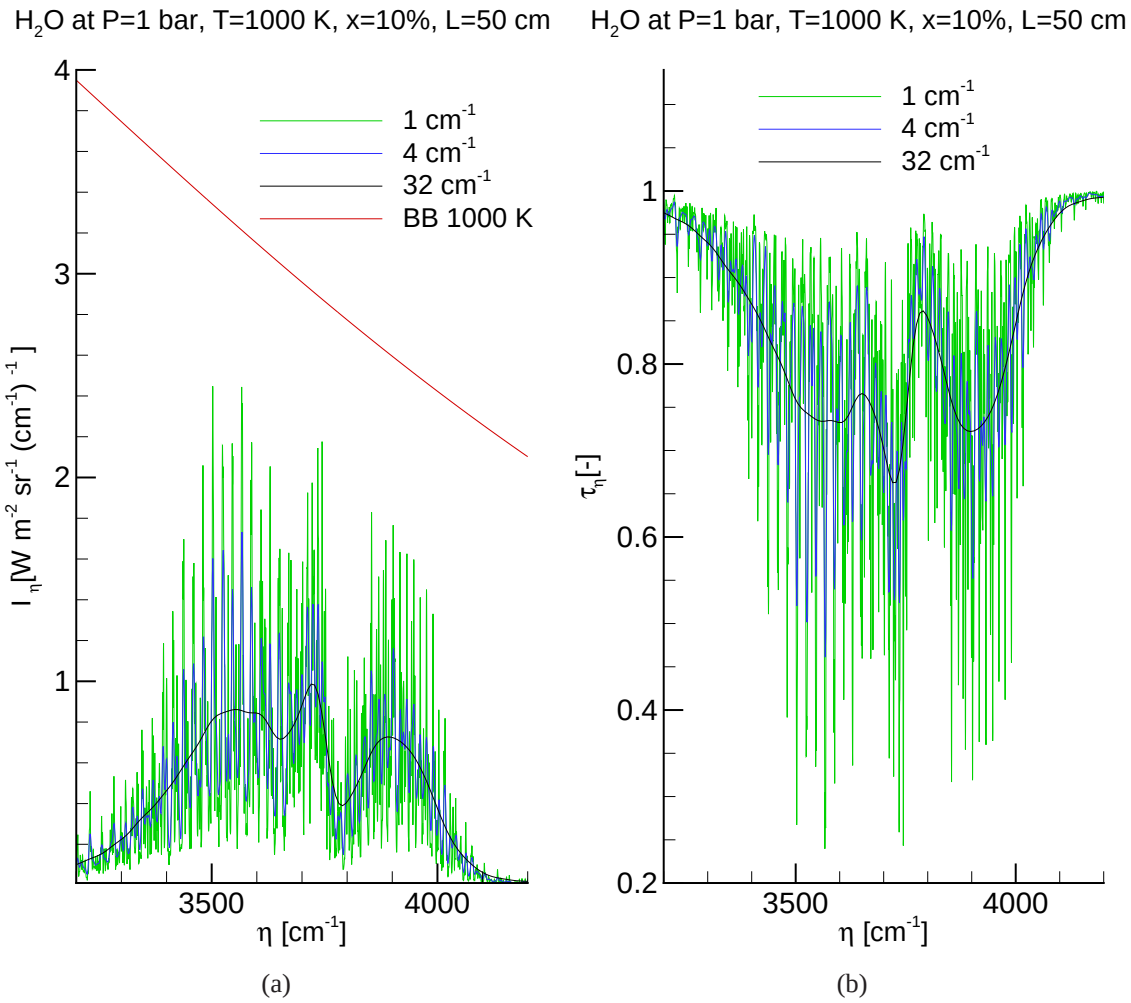

Figure 1.6: Emitted spectral intensity spectrum and transmissivity spectrum for the H_2O 2.7 μm band at varying resolutions of a 50 cm long H_2O gas column at temperature of 1000 K and concentration of 10%: (a) emitted spectral intensity; (b) transmissivity.

with adequate step size. However, calculation of the adequate step size may be time consuming. By increasing the value of each diagonal term in the Hessian matrix for Newton's method to avoid inverting a near-singular matrix, the Levenberg-Marquardt was developed. An nonnegative scaling factor for increasing the diagonal term is adjusted at each iteration. If an iteration gives insufficient reduction, this factor can be increased, and it blend more toward the simple gradient descent method. Whereas if reduction of the objective function is rapid, a smaller value can be used and the method become Newton's method. This method is well-known to have a fast convergence rate and also the convergence can be guaranteed [78].

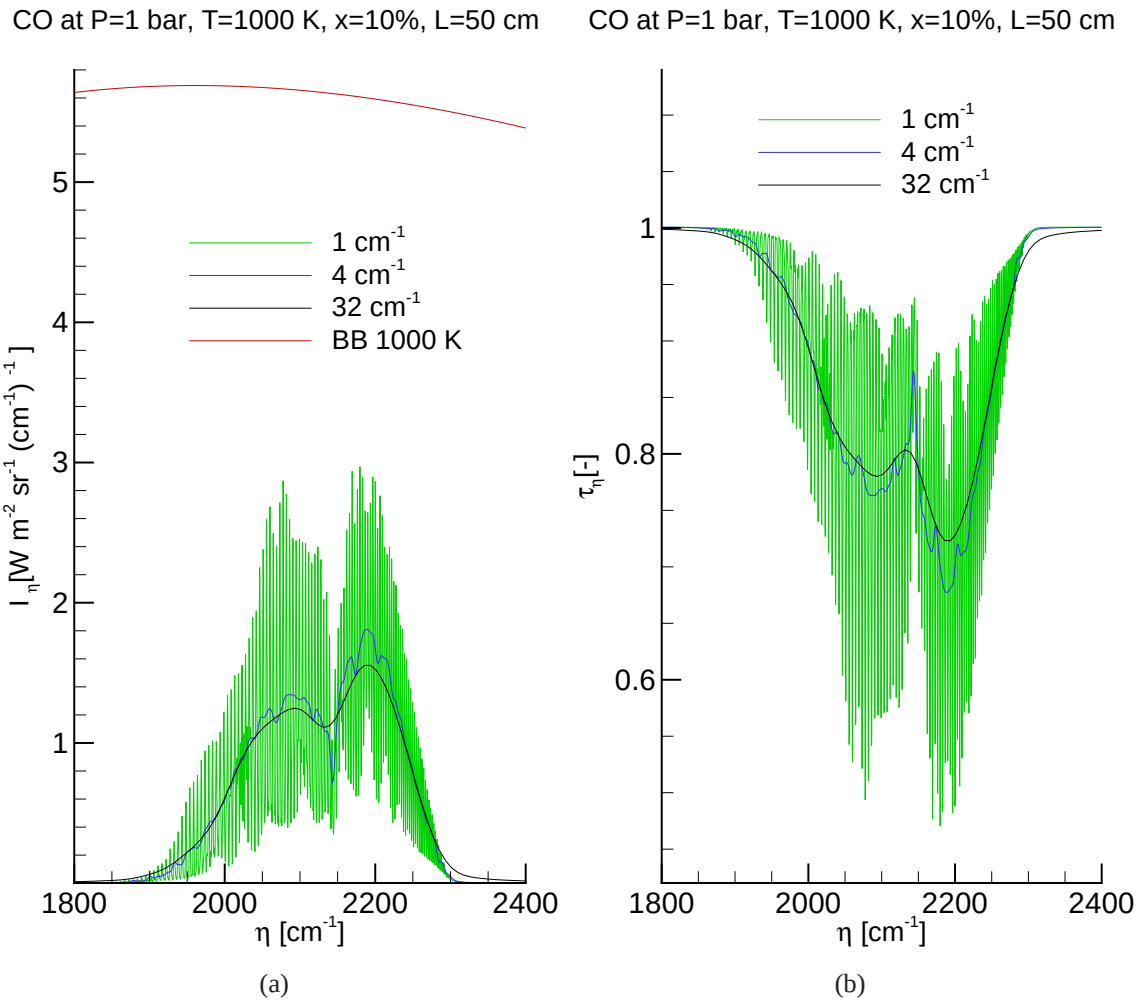

Figure 1.7: Emitted spectral intensity spectrum and transmissivity spectrum for the CO 4.7 μm band at varying resolutions of a 50 cm long CO gas column at temperature of 1000 K and concentration of 10%: (a) emitted spectral intensity; (b) transmissivity.

Hommert et al. [79] tried to retrieve line-of-sight temperature and/or concentrations for a symmetric laminar CH_4/air diffusion flame by spectral emission measurements. A forward calculation model was developed that relates the emitted spectral intensity to the local temperature and species concentrations. The measured spectral intensities were synthesized from the forward calculation model with the assumed profiles, which were used to conduct analytical experiments to investigate the usefulness of this method. In their later experimental verification [80], a study was conducted in which CO_2 with N_2 temperatures varying from 700 to 1350 K over a 25 cm path were produced in an electrically heated furnace. Temperature and concentration profiles were predefined

as polynomial functions and the coefficients of the polynomials were determined with a gradient based optimization routine. However, the tested temperature profiles were either linear or second order polynomials, which may not be the case for line-of-sight flame temperature profiles, since the maximum flame temperatures do not always occur at axial position. It was also indicated that detailed concentration profile determination is not suitable for their proposed method. In order to retrieve temperature profiles accurately, an approximate concentration distribution was specified for the emitting species.

Lim et al. [81] linearized the radiative transfer equation (RTE) in conjunction with the maximum likelihood estimation to deconvolute the spectral emitted intensities for temperatures and concentrations. The spectral emitted intensity was approximated as a linear function of temperature, soot concentration and two major combustion species (CO_2 and H_2O) concentrations. Coefficients for the linearized function were obtained from the RADCAL database [82], a narrow-band database. The method was first verified using synthetic spectral data points in the 1.3 to 4.8 μm spectral interval. At the same time, the spectral radiation intensities emitted from a one-dimensional McKenna burner [83] was measured at multiple wavelengths using the high-speed mid-infrared spectrometer ES100 [61]. The estimated gas temperature and concentrations obtained using this method are very close to those obtained with thin filament pyrometry and theoretical calculations.

Although temperatures and species concentration were retrieved using transmission [39, 40] or emission [79–81, 84] measurements in a number of ways, these results were not accurate enough due to the lack of an accurate radiation prediction model and robust inverse algorithms. Song et al. [85–88] developed a spectral remote sensing technique to reconstruct CO_2 temperature profiles based on radiative intensity measurements for the CO_2 4.3 μm band. A correlated-k-based weighted-sum-of-gray-gases narrow band model [89] was employed to predict the emitted intensity from the CO_2 4.3 μm band, since it has been optimally modeled for this band. Song et al. tested two inversion algorithms: the modified constrained inversion method (MCIM), and the base function-based inversion method (BFIM). The MCIM works well for good starting points while the BFIM only works well if an appropriate base function is selected. By combining these two methods, they came up with a new method called BFIM-based MCIM (BCIM). First a base function is selected for the BFIM and preliminary inverse result is obtained with the BFIM. This result is then used as the starting points for the MCIM. In the proposed MCIM algorithm, Tikhonov regularization was applied to enforce some degree of smoothness on the solution to mitigate the ill-posedness of this problem. This method is considered to be applicable, with good accuracy and capability, to inverse problems in large-scale furnaces. However, empirical values for the regularization parameter were employed and, therefore, this algorithm lacks generality.

The optical diagnostics described so far all deal with a single line-of-sight, and require a prescribed spatial profile for temperature and concentration. The earliest attempts to relax this restriction focused on axisymmetric flames, in which optical data were collected at uniformly-spaced, parallel lines-of-sight. These data are related to an unknown radial distribution by Abel's equation, an ill-posed Volterra equation of the first-kind, or in discrete form of an ill-conditioned matrix equation. The ill-conditioning amplifies small amounts of measurement noise into large variations in the desired field variable, and become worse as the spacing between axial data points is refined.

The most common approach used to deconvolve axisymmetric flames in the combustion literature is the Abel three point inversion [90], which works by smoothing the data in the axial direction

but does not treat the underlying ill-posedess of Abel's equation directly, thereby limiting the accuracy and stability of the solution. Very recently Tikhonov regularization has been applied to this problem [91,92]. In this approach, an extra set of equations that promotes a smooth solution is added to the ill-conditioned matrix equation. Results obtained by Tikhonov-stabilized deconvolution are more resilient to experimental noise, and in contract to the Abel three point inversion, deconvolution accuracy improves as the axial measurements are refined.

Deconvolution of line-of-sight data from nonaxisymmetric flames requires more elaborate tomography algorithms, which are either based on Fourier transforms, or algebraic reconstruction. Taking a Fourier transform of Eq. (1.1) with respect to the unknown absorption coefficient makes its unknown distribution an explicit and continuous function of the optical data. But since data are only known over a discrete set of angles and axial locations, a filtering function must be used to reconstruct the image out of low frequency components while neglecting high frequencies that likely correspond to noise. Unfortunately, this approach requires dense and uniformly spaced axial and angular measurements exceeding the available optical access in most experiments. Even in experiments that have the required optical access, multiangle measurements are usually made by rotating the optics or the tomography field, disallowing time-resolved deconvolution. In algebraic reconstruction, on the other hand, the tomography field is split into pixels of presumed uniform properties. This discretization leads to an ill-conditioned and rank-deficient matrix equation that can be solved using the Tikhonov method described above. Algebraic reconstruction requires far fewer beams compared to Fourier transform based method, and they need not have a regular arrangement. This makes them well-suited for applications that permit limited optical access to the flow field, as is the case in many practical combustion devices. For example, Terzija et al. [93] used an irregular arrangement of 32 infrared beams, coupled with a regularized algebraic reconstruction algorithm to measure the time-varying fuel-air concentration distribution within the cylinder of an internal combustion engine.

For turbulent fields, the conditions along a line-of-sight of a high-speed detector, for any given snapshot in time, are far too complicated to be reconstructed from spectroscopic data. One must have knowledge of the flowfield, and of how turbulence and radiation interact along the detector's line-of-sight, to deduce mean and rms values of temperature and concentrations.

1.1.4 Effects of Turbulence on Radiation and Radiometric Diagnostics

For a turbulent system, it has long been recognized that the nonlinear interaction between turbulence and radiation (TRI) has profound effects on turbulent combustion [94–98]. The radiative signal from combustion gases is influenced by nonlinear interaction with turbulence. In the presence of TRI, temperature and concentration can never be measured directly, but must be deduced using knowledge of turbulence structures or employing TRI models. Similarly, the radiative intensity hitting a detector is influenced by the nonlinear interaction with turbulence. The time-averaged signal of Eq. (1.4) is given by

$$\begin{aligned}\langle I_\eta \rangle &= I_{0\eta}\langle \tau_\eta(T,x)\rangle + \langle I_{b\eta}(T)\left(1-\tau_\eta(T,x)\right)\rangle \\ &\neq I_{0\eta}\tau_\eta(\langle T\rangle,\langle x\rangle) + I_{b\eta}(\langle T\rangle)\left(1-\tau_\eta(\langle T\rangle,\langle x\rangle)\right)\end{aligned} \tag{1.6}$$

i.e., the mean signal cannot be evaluated in terms of the mean scalars $\langle T \rangle, \langle x \rangle$. Thus, temperatures and concentrations can never be measured directly in a turbulent field in the presence of TRI, but must be deduced using knowledge of turbulence structures or employing turbulence–radiation interaction models.

Experimental investigations by Faeth and Gore [65–67, 99–109] and probability density function (PDF) based calculations [110–114] have shown that TRI always increases the heat loss from a flame, and this additional heat loss can reach 60% of the total and more, leading to a reduction in the local gas temperature of 200 °C or more. Therefore, the radiative signal hitting a detector is influenced by the nonlinear interaction with turbulence. The TRI effects, although acknowledged and qualitatively understood over the last three decades or so, are extremely difficult to model. Most work in TRI has been devoted to the study of turbulence on total radiative heat transfer emitted by a hot medium. A rather different challenge is accurate modeling of the correlation between local instantaneous radiation intensity along the optical path and local absorption coefficients [115]. Most works have neglected this correlation based on the suggestion and arguments given by Kabashnikov and Myasnikova [116] that, if the mean free path for radiation is much larger than the turbulence length scale, then the local intensity is governed by fluctuations far away, and thus should be only weakly correlated with local absorption coefficient fluctuations. This assumption appears to be valid over most of the gas spectrum for small-scale, lower-sooting flames and is known as the optically thin fluctuation assumption (OTFA), but questionable for very strong spectral lines. Ko et al. [117] developed a spectral remote sensing method to retrieve mean temperature and concentration from spectral turbulent intensities using the CO_2 4.3 μm band by applying the OTFA. For their proposed method, it is claimed that the coupled temperature/concentration fluctuation amplitudes and mean values can be successfully inverted from optically measured intensity spectra. However, only retrieved mean temperature/concentration profiles along the path were presented and not much detail was given for the inverse method. Unlike modeling TRI on spectral intensity, TRI on transmissivity can be accurately modeled by assuming the pdf shape of the absorption coefficient. An early study by Foster [118] showed that calculation of the mean transmissivity from a turbulent flame must take turbulent fluctuations into account. Coelho [115] showed that, in the presence of turbulent fluctuations, the turbulent fluctuation of the absorption coefficient increases the transmissivity of the medium if the pdf of the absorption coefficient is Gaussian and his observation is in agreement with the theoretical findings of Foster [118].

1.2 Objectives

The goals of the current research are to develop new radiation tools to accurately deduce temperatures and species concentrations from radiometric measurements in laminar and turbulent combustion systems. In summary, the following are the objectives:

- Construct an updated line-by-line (LBL) absorption coefficient database based on the spectroscopy database HITEMP 2010 for several combustion species.
- Conduct instrument lineshape analysis for FTIR spectrometer by experiments to evaluate the validness of using ideal FTIR instrument lineshape functions for predicting lower resolution radiative spectra.

- Develop inverse radiation tools to deduce temperature and concentrations from medium- and low-resolution measurements of line-of-sight transmissivities for a homogeneous gas media. Validate this model by experimental measured transmissivity data for CO_2 and H_2O.

- Conduct a systematic investigation to determine what spectral range measured at what resolution for what species leads to the most accurate reconstruction of the underlying temperature and concentration fields based on the developed inverse radiation tools.

- Develop an inverse radiation model for reconstruction of temperature and concentration profiles for nonhomogeneous gas media. Due to the ill-posedness of the inverse problem, additional conditions or criteria need to be imposed to determine the most realistic solution.

- Further develop the inverse radiation tools for the more difficult diagnostics in turbulent systems to retrieve time-averaged temperature and species concentrations, their rms values and turbulent length scales from radiometric measurement in combustion system.

1.3 Outline of the Chapters to Follow

Chapter 2 will present the development and validation of an inverse radiation model for optical determination of temperature and species concentration of homogeneous gas media. Based on the model developed in Chapter 2, a systematic investigation of optimal spectral parameters (wavenumber and resolution) for determination of combustion gas temperature and concentration will be presented in Chapter 3. In Chapter 4, temperature profiles and average concentration inversions from CO_2 spectral intensities through Levenberg-Marquardt optimization and Tikhonov regularization will be presented. A new regularization parameter selection scheme will be proposed. In Chapter 5, an outline for retrieving mean and rms values for temperature and concentration from time-averaged measurements of turbulent transmissivities and their rms values will be presented. Chapter 6 will conclude this dissertation by summarizing important conclusions made in this work and proposing some research topics which may be important for the future.

Chapter 2

Inverse Radiation Model for Homogeneous Media

2.1 Introduction

As a start, inverse radiation tools for homogeneous gas media are developed to deduce temperature and species concentration from higher to lower-resolution measurements of line-of-sight transmissivities. A number of inverse techniques have been used for temperature or concentration inversion. Several inverse radiation algorithms like the Quasi-Newton method [77], Conjugate Gradient Method [38] and the Levenberg-Marquardt method [78] have been applied. As discussed in the previous section, the Levenberg-Marquardt method is well-known to have a fast convergence rate and also the convergence can be guaranteed. From many transmissivity inversions, we found the Levenberg-Marquardt inverse scheme to be relatively reliable to retrieve temperature and concentration along single lines-of-sight, and to be more accurate and requiring less computational effort. Therefore, the Levenberg-Marquardt method is employed in the scheme described below. The inverse model is validated by retrieving temperatures and species concentrations from experimental medium-resolution CO_2 and H_2O transmissivity data obtained previously [69–73] for a wide range of temperatures and species concentrations.

2.2 Inverse Radiation Model Development

2.2.1 Forward Calculation

A forward calculation model is developed to calculate medium-to-coarse resolution transmissivities for a given pressure path length, gas concentration and temperature, and is incorporated into the inverse calculation model (see next section) to provide predicted transmissivities. For a homogeneous gas path, the spectral transmissivity is given by

$$\tau_\eta(T, x) = e^{-\kappa_\eta(T,x)L} \tag{2.1}$$

where κ_η is the absorption coefficient calculated from the HITEMP 2010 LBL database, and L is gas path length.

In optical measurements of combustion gases, transmissivity spectra can be obtained with a Fourier transform infrared (FTIR) spectrometer. To obtain the final spectrum, a Fourier transform (FT) must be performed on the interferogram. Because of the finite range of the interferometer's moving mirror the interferogram does not extend to infinity, effectively causing the interferogram to be multiplied by a truncating function. By the convolution theorem, the FT of two functions multiplied together can be described as the convolution of the transforms of each individual function,

$$\mathcal{F}(f \cdot g) = \mathcal{F}(f) * \mathcal{F}(g), \tag{2.2}$$

where $*$ denotes convolution, for functions f and g, the convolution is defined as,

$$(f * g)(t) = \int_0^\infty f(\tau) g(t-\tau) \mathrm{d}\tau \tag{2.3}$$

Eq. (2.2) meaning that the output of any FTIR is convolved with the FT of the truncating function $A(z)$, which is unity between $-\Delta$ and $+\Delta$, and zero at all other points, that is,

$$A(z) = \begin{cases} 1 & -\Delta \le z \le \Delta \\ 0 & z > |\Delta| \end{cases} \tag{2.4}$$

where z is the distance traveled by the moving mirror and Δ defines the limits of the mirror, commonly termed the FTIR retardation.

In order to make more information to be resolved in the final spectrum, truncating functions may be weighted by so-called apodization functions. For triangular apodization,

$$A(z) = \begin{cases} 1 - \left|\frac{z}{\Delta}\right| & -\Delta \le z \le \Delta \\ 0 & z > |\Delta| \end{cases} \tag{2.5}$$

The Fourier transform (FT) of the triangular apodization function is the instrument line function (ILF). A Mattson infinity HR series FTIR used by Bharadwaj and Modest [69,70,72] uses triangular apodization. In order to use their experimental data to validate the model, the ILF Γ of this FTIR is used in the present study,

$$\Gamma(\eta) = \Delta \mathrm{sinc}^2(\pi\Delta\eta) = \Delta \frac{\sin^2(\pi\Delta\eta)}{(\pi\Delta\eta)^2} \tag{2.6}$$

where Δ is commonly termed the FTIR retardation.The nominal resolution (Res) of an FTIR is generally defined as $1/\Delta$ [119]. Because retardation cannot be infinitely large, FTIRs can only obtain finite resolution and the resolution can be adjusted by changing the retardation of the moving mirror. However, the relationship between retardation and resolution may be defined in different ways [120]. The Mattson infinity HR series FTIR used by Bharadwaj and Modest [69, 70, 72] has a retardation of $\Delta = 0.666/Res$ and the ILF of this FTIR is used in the present study to compare against Bharadwaj and Modest's measurements [69,70,72], as well as convolved medium-resolution

data from Fateev and Clausen's [71, 73] transmissivity measurements. Then Eq. (2.6) becomes

$$\Gamma(\eta) = \frac{0.666}{Res}\text{sinc}^2\left(\frac{0.666\pi}{Res}\eta\right) \tag{2.7}$$

After transmissivity spectra are convolved with the ILF $\Gamma(\eta)$, they become,

$$\tau_{\eta c} = \int_0^\infty \tau(\eta')\Gamma(\eta - \eta')d\eta' \tag{2.8}$$

As the convolution theorem states, the convolution of two functions equals the inverse Fourier transform of the product of the Fourier transforms of the two functions, or

$$\tau_{\eta c} = \mathcal{F}^{-1}\left[\mathcal{F}(\tau)\cdot\mathcal{F}(\Gamma)\right] \tag{2.9}$$

2.2.2 Inverse Calculation

The present study is limited to homogeneous gas layers of N_2+CO_2 or N_2+H_2O mixtures and, therefore, only two parameters need to be determined from inverse algorithms, temperature and concentration. By minimizing an objective function, gas temperature and concentration will be deduced. The objective function represents the difference between the predicted and measured transmissivities, i.e.,

$$F = \sum_{i=1}^{I}\left(\frac{\tau_i - Y_i}{\sigma_i}\right)^2 = F(\mathbf{z}) \tag{2.10}$$

where τ_i is the predicted transmissivity spectrum from forward calculations, Y_i is the measured transmissivity spectrum, σ_i^2 is the experimental uncertainty of the data points and $\mathbf{z} = (x, T)^T$ is the parameter vector. The goal of inverse calculations is to minimize this function by properly guessing the parameter vector until the best match between the measured transmissivity spectrum Y_i and predicted transmissivity spectrum τ_i is achieved. In the present study, the Levenberg-Marquardt method is applied in the inverse radiation calculations. In this method, the parameter vector $\mathbf{z}$ is gradually increased by a small value $\delta\mathbf{z}$,

$$\mathbf{z}_{new} = \mathbf{z}_{old} + \delta\mathbf{z} \tag{2.11}$$

with

$$\delta\mathbf{z} = -\mathbf{H}'^{-1}\mathbf{b} \tag{2.12}$$

and the vector $\mathbf{b} = \nabla F(\mathbf{z})$ is the gradient vector of F with respect to $\mathbf{z}$, and $\mathbf{H}'$ is a matrix with elements

$$h'_{ij} = \begin{cases} (1+\mu)h_{ij} & i = j \\ h_{ij} & i \neq j \end{cases} \tag{2.13}$$

where the h_{ij} are the elements of the Hessian matrix $\mathbf{H} = \nabla^2 F(\mathbf{z})$.

The nonnegative scaling factor, μ, is adjusted at each iteration. If reduction of the objective function is rapid, a smaller value can be used, whereas if an iteration gives insufficient reduction, μ can be increased. If $\delta\vec{z}$ gets sufficiently small, the iteration will stop and the parameter vector $\vec{z}$ will

be obtained. The Levenberg-Marquardt method increases the value of each diagonal term of the ill-conditioned Hessian matrix **H** (regularization), to mitigate the ill-posedness of the problem. Details for the computational algorithm using the Levenberg-Marquardt method can be found in [78, 121, 122]. the procedure for retrieving all the parameters is summarized as follows

1. Assume a starting point $\mathbf{z}_0$.
2. Compute objective function $F(\mathbf{z}_0)$.
3. Pick a safe (relatively large) value for μ.
4. Solve $\delta\mathbf{z}$ using Eq. (2.12).
5. If $F(\mathbf{z}+\delta\mathbf{z}) \geq F(\mathbf{z})$, increase μ, go back to 4.
6. If $F(\mathbf{z}+\delta\mathbf{z}) < F(\mathbf{z})$, decrease μ, update $\mathbf{z}$ by $\mathbf{z}+\delta\mathbf{z}$ and go back to 4.
7. Stop iteration when $|\delta\mathbf{z}|$ gets sufficiently small

2.3 Transmissvity measurements for CO_2 and H_2O

Bharadwaj and Modest performed measurements of CO_2 and H_2O transmissivity at temperatures up to 1550 K and with a resolution of 4 cm^{-1} using a drop tube mechanism and FTIR spectrometer [69, 70, 72]. The gas temperature was measured by a thermocouple and a gas delivery system was used to supply mixtures of N_2+CO_2 and N_2+H_2O. By controlling the flow rate of N_2 and CO_2 or N_2 and H_2O, the desired mole fraction of CO_2 or H_2O in the test cell was obtained. CO_2 concentrations were measured by ball flow meters and H_2O concentrations were measured by an Agilent series micro gas chromatograph. The reader is referred to [69, 70] and [72] for more details on the experiment.

High-resolution transmissivity measurements have been made by Fateev and Clausen with an atmospheric-pressure high-temperature flow gas cell (HGC), Fig. 2.1, for CO_2 at temperatures up to 1773 K [71] and H_2O at temperatures up to 1673 K [73]. The gas cell was designed as a flow gas cell with a so-called "laminar flow window", where care was taken to obtain a uniform gas temperature profile and a well defined path length. "Laminar flow window" is not an actual window and its not an aerodynamic lens. A laminar flow window forms by two opposite gas flows that meet each other and escape the cell through a narrow gap between the left/right buffer and the central parts of the cell, Fig. 2.1. Arrows in Fig. 2.1 show directions of the gas flows.

It consists of three different parts: a high-temperature sample cell with a length of 0.533 m and two "buffer" cold gas parts on the left- and the right-hand sides of the hot sample cell. The buffer parts are filled with a UV/IR-transparent (purge) gas (e.g., N_2), whereas the central sample cell can be filled with the gas under investigation (e.g., N_2+H_2O/CO_2). The aperture of the sample cell is kept small (i.e., a diameter of 0.015 m) in order to reduce heat transfer by radiation from the sample cell and to reduce the risk of collapse of well-defined flows in the laminar flow windows. The laminar flow windows also function as a radiation shield. Similarly, apertures placed at the ends between the laminar flow windows and the cold windows reduce the heat losses by radiation

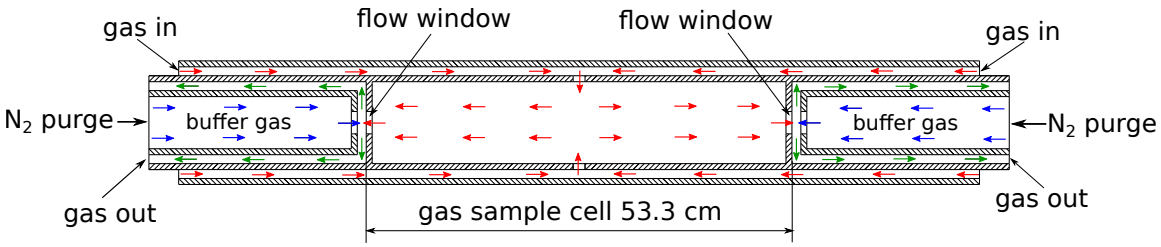

Figure 2.1: High-temperature flow gas cell (HGC) used in the experiments [71, 73]. Arrows show directions of the gas flows. See text for more explanation.

and convection by breaking down the vortices created by the thermal gradient in the buffer sections. High-quality alumina ceramics were used in order to minimize hetero-phase reactions and to avoid contact of the sample gas with any hot metal parts. A uniform temperature profile is obtained by heating the gas cell with a dedicated three-zone furnace in order to compensate for the heat loss at the ends of the gas cell. The sample gas is preheated. Flows of the gases in the sample cell and in the buffer parts are kept at about the same flow rates. The outer windows placed at the ends of the buffer parts are replaceable. In all experiments, KBr-windows have been used. The gas flow through the HGC maintains a highly uniform and stable temperature in the range 23 °C to 1500 °C. The temperature uniformity over 0.45 m in the sample cell was found to be better than ± 1 °C (the maximum and minimum temperature values T_{max} and T_{min} measured by a calibrated thermocouple along the central zone of the cell show $T_{max} - T_{min} \leq 1\,°C$), or on average ± 0.5 °C.

High-resolution IR-absorption measurements were performed with an FTIR-spectrometer (Nicolet model 5700) equipped with DTGS and InSb IR-detectors. The nominal resolution of the FTIR, $\Delta\eta$, was set to 0.125 cm^{-1} and was sufficient in order to observe in fine-structure absorption bands features of CO_2 and H_2O molecules.

A highly stable calibrated blackbody operating at 800 °C was utilized as an IR light source for absorption and reference measurements. After passing through the HGC, the IR light beam was restricted by a variable aperture to minimize possible surface effects from the HGC with another pass through an aperture (Jacquinot-stop) mounted on the outer part of the Nicolet spectrometer operated in the external light source mode. More detail about the experimental setup can be found in [71]. Experiments have been performed with various mixtures of N_2+CO_2 (1-100 %) and N_2+H_2O (8-40 %) at a flow rate about 2 l/min. Different CO_2 concentrations were obtained by flow mixing of N_2 with either pre-mixed N_2+CO_2 (1%, 10%) or CO_2 (100%) gases at different N_2:N_2+CO_2 (1%, 10%) or N_2 : CO_2 (100%) ratios at temperatures from 1000 K up to 1773 K. Calibrated mass-flow controllers were used to control the gas flows. More detail can be found in [71]. For H_2O IR-absorption measurements an accurate HAMILTON syringe pump system [123] with a water evaporator was used in order to produce controlled N_2+H_2O (8-40%) mixtures for temperatures up to 1673 K. Transmissivity spectra of CO_2 and H_2O were calculated from four interferograms measured with N_2 and N_2+CO_2 (or H_2O) with and without IR light source as described in [71], Eq. (1). To make these data comparable with Bharadwaj and Modest's experimental transmissivity data and to make the inverse calculation more efficient, the high-resolution data were convolved to

medium-resolution (nominal resolution $\Delta\eta = 4$ cm^{-1}).

In this study, the CO_2 and H_2O transmissivity data measured by Bharadwaj and Modest [69, 70, 72] with medium-resolution ($\Delta\eta = 4$ cm^{-1}) at lower temperatures (below 600 K) are used as inputs for the inverse calculation model. For temperatures of 1000 K and beyond, medium-resolution ($\Delta\eta = 4$ cm^{-1}) data, which are convolved from the high-resolution CO_2 and H_2O transmissivities of Fateev and Clausen's [71, 73], are used as inputs. For Bharadwaj and Modest's measurements, the uncertainty in temperature is claimed to be < 2% at all temperatures. The experimental uncertainty for measurement of CO_2 concentration by the flow meter is 5% of maximum flow meter range [124] (the error can be very high for measuring small CO_2 concentration). The gas chromatograph used for measuring H_2O concentrations is accurate to 5% [72]. In Fateev and Clausen's measurements, temperatures and gas concentrations were claimed very accurate and due to design of the cell and laminar flow arrangement the concentration profile is highly uniform along the cell [125]. However, as shown in Fig. 2.1, small fluctuations of sample gas path length are also possible due to thermal expansion of the gas cell ceramics with temperature. It is estimated that the optical path length is increased by 0.7 cm or 1.3% when raising the temperature from ambient to 1600 °C [125].

2.3.1 Validation for Convolution of Convolution

Figure 2.2 shows spectral transmissivities for a N_2-CO_2 mixture containing 10% CO_2 at 1 bar and a temperature of 1000 K for small part of the 4.3 μm band. As an example, the band with a nominal resolution of 0.125 cm^{-1} exhibits the distinct line shape of all stronger lines. While the fine resolution has a very distinct structure, which can be exploited for inversion, it is also subject to theoretical uncertainty, such as calculated values for line strengths, shapes and widths. Fine resolution is also more susceptible to experimental noise, and requires large collection and computational times. After convolving to a medium resolution (here shows 4 cm^{-1}), smoother averaged shapes with less data points are obtained.

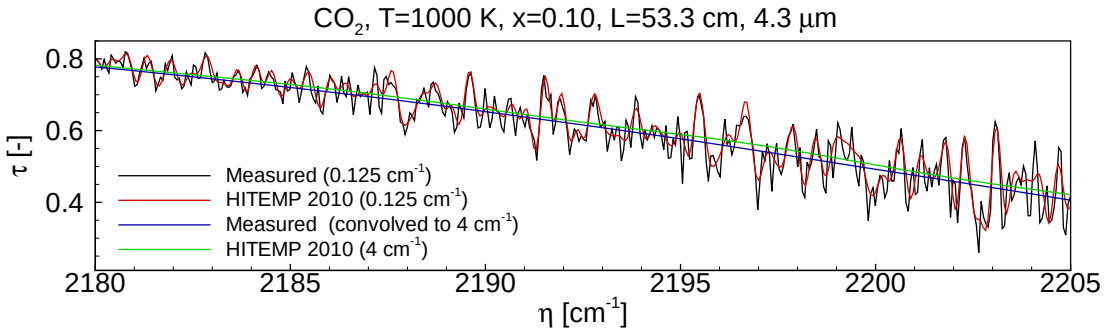

Figure 2.2: Comparison of measured transmissivity with calculated transmissivity for lower wavenumber parts of CO_2 (10%) 4.3 μm band at 1000 K

The experimental data measured by Fateev and Clausen [71, 73] were recorded as interferograms. In order to calculate spectra, an inverse Fourier transform is performed with a certain

apodization function. In their experiments, a boxcar apodization function corresponding to a nominal resolution of 0.125 cm^{-1} was used, meaning the ILF is a *sinc* function. These high-resolution spectra are further convolved with Eq. (2.7) to convert the spectra into medium-to-coarse resolution data. Accordingly, the forward calculations need to consider the effects of the boxcar apodization function as well as the triangular apodization function. This means Eq. (2.9) in the forward calculations needs to be changed to,

$$\tau_{\eta c} = \mathcal{F}^{-1}\left[\mathcal{F}(\tau) \cdot \mathcal{F}(\Gamma_1) \cdot \mathcal{F}(\Gamma_2)\right] \tag{2.14}$$

where Γ_1 is a *sinc* function with nominal resolution of 0.125 cm^{-1} and Γ_2 is a $sinc^2$ function with medium-to-coarse nominal resolution, i.e. 1, 2, 4, 8, 16 and 32 cm^{-1}.

It is found that Eqs. (2.14) and (2.7) are almost identical for calculating medium-to-coarse resolution transmissivities. Because of the big difference between the nominal resolutions of these two ILFs, as shown in Fig. 2.3 (a) for the *sinc* function with nominal resolution of 0.125 cm^{-1} and the $sinc^2$ function with nominal resolution of 1 cm^{-1}, the *sinc* function with nominal resolution of 0.125 cm^{-1} has negligible impact on Eq. (2.14). This can be seen in Fig. 2.3 (b): the convolution of the two ILFs are almost identical to the $sinc^2$ function with nominal resolution of 1 cm^{-1}. Very minor differences are observed at the primary peaks and valleys. For other medium-to-coarse resolutions, the differences are even smaller. Therefore, Eq. (2.7) remains valid for forward calculations.

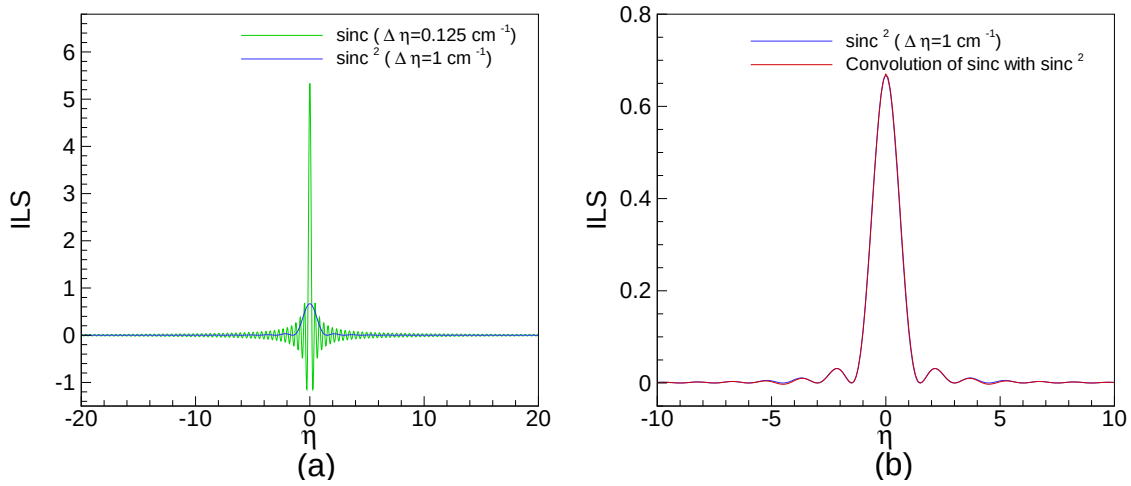

Figure 2.3: (a), Comparison of the *sinc* function with nominal resolution of 0.125 cm^{-1} and the $sinc^2$ function with nominal resolution of 1 cm^{-1}. (b), Comparison of convolutions between the two ILFs and $sinc^2$ function with nominal resolution of 1 cm^{-1}.

Table. 2.1 shows the comparison of inverse results using fine-resolution (0.125 cm^{-1})) and medium-to-coarse resolutions (1, 2, 4, 8, 16 and 32 cm^{-1}) transmissivity data for the CO_2 2.7 μm and 4.3 μm bands for temperature and concentration of 1000 K and 0.10, respectively. As shown in

the table, the fine-resolution data do not give better results than medium-to-coarse resolution data and the resolutions variation from 1-32 cm^{-1} do not have significant effect on the inverse results. Coarse resolutions have fewer data points and require less collection and computational time, so coarse-resolution spectra should be used for optical diagnostics. However, in the present study, the experimental transmissivities measured by Bharadwaj and Modest [69, 70, 72] have resolution of 4 cm^{-1}. In order to use these data to validate the model, the resolution of 4 cm^{-1} is used. Accordingly, Fateev and Clausen's experimental transmissivities are convolved to a medium resolution of 4 cm^{-1} to make them comparable with Bharadwaj and Modest's measurements.

Table 2.1: Comparison of inverse calculation results using Fateev and Clausen's transmissivity spectra [71] at fine and medium-to-coarse resolutions for CO_2 at 1000 K and concentration at 0.1

Test condition (1000 K,0.10)		Retrieved T (K)	Retrieved x	Error for T (%)	Error for x (%)
L=53.3 cm, 2.7 μm	0.125 cm^{-1}	1024.07	0.1072	2.41	7.22
	1 cm^{-1}	992.32	0.1072	-0.77	7.18
	2 cm^{-1}	986.97	0.1069	-1.30	6.87
	4 cm^{-1}	990.84	0.1076	-0.92	7.64
	8 cm^{-1}	988.17	0.1077	-1.18	7.70
	16 cm^{-1}	993.96	0.1065	-0.60	6.52
	32 cm^{-1}	993.31	0.1070	-0.67	6.97
L=53.3 cm, 4.3 μm	0.125 cm^{-1}	989.07	0.1099	-1.09	9.86
	1 cm^{-1}	995.36	0.1064	-0.46	6.35
	2 cm^{-1}	996.24	0.1061	-0.38	6.07
	4 cm^{-1}	995.48	0.1065	-0.45	6.49
	8 cm^{-1}	994.17	0.1066	-0.58	6.60
	16 cm^{-1}	996.30	0.1055	-0.37	5.52
	32 cm^{-1}	998.46	0.1049	-0.15	4.94

2.3.2 Carbon Dioxide

Two CO_2 spectral bands at 2.7 and 4.3 μm were tested. The test conditions and inverse results are summarized in Tables 2.2 to 2.7.

First, medium-resolution (4 cm^{-1}) data at lower temperatures for 300 K and 600 K measured by Bharadwaj and Modest were used. As shown in Figs. 2.4-2.7, the measured data include error bars, which are the experimental standard deviations of six different sets of transmission spectra. Table 2.2, Figs. 2.4 and 2.5 show the inverse results and transmissivities comparison for 300 K. As shown in Fig. 2.4, there are only small differences among the the measured, nominal and retrieved spectra for 2.7 μm band if CO_2 concentration $x = 0.01$, but large errors occur when retrieving CO_2 temperature and concentration. Because the pressure path length (PxL) for this case is very small, transmissivities approach unity for large parts of the band and absorption is so weak that the signal-to-noise ratio (SNR) is very small, making the inverse results very sensitives to noise. This may explain why the inverse errors both for temperature and concentration are relatively large. If the pressure path length (PxL) increases, the SNR also increases, and errors for temperature and concentration become smaller. However, there are still some differences at the band center for $x = 0.05$

and $x = 1.00$ as indicated in Fig. 2.4 and errors for concentration inversion are relatively large. This can be explained by the fact that experimental transmissivities near the band wings appear to be higher than unity (see insert in Fig. 2.4), which may be due to a wavenumber-dependent base line offset in the experimental data; On the other hand, for the $x = 0.05$ case ball-type flow meters were used to measure CO_2 concentration in Bharadwaj and Modest's measurements, and the experimental uncertainty for the flow meter is 5% of maximum flow meter range [124]. Nevertheless, retrieved transmissivities overlap with the measured data very well (as compared to the nominal data), indicating that the inverse radiation technique may be superior to a ball flow meter to determine CO_2 concentrations. Table 2.2 also includes inverse results for the CO_2 4.3 μm band, for which the retrieved temperature and concentration are very accurate; this is also shown in Fig. 2.5. For the pure CO_2 case inversion was aided by not allowing unphysical values for concentration. The retrieved spectrum perfectly overlaps with the nominal spectrum as well as the measured data.

Table 2.2: Inverse calculation results using Bharadwaj and Modest's transmissivity spectra [69, 70] for CO_2 at 300 K

Test condition (300 K)		Retrieved T (K)	Retrieved x	Error for T (%)	Error for x (%)
L=20 cm, 2.7 μm	x=0.01	233.10	0.0078	-22.30	-22.00
	x=0.05	289.73	0.0426	-3.42	-14.88
	x=1.00	312.84	0.8381	4.28	-16.19
L=20 cm, 4.3 μm	x=0.01	306.21	0.0102	2.07	1.50
	x=0.05	300.40	0.0477	0.13	-4.64
	x=1.00	308.71	0.9808	2.90	-1.92

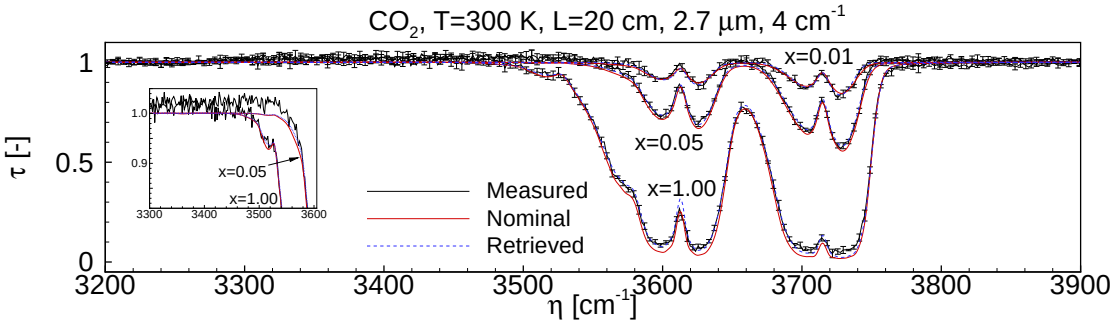

Figure 2.4: Comparison of retrieved transmissivity with measured transmissivity and nominal transmissivity calculated at the given temperature T=300 K for CO_2 2.7 μm band

Table 2.3 shows the inverse results for 600 K. It indicates that, if the CO_2 2.7 μm band is employed at atmospheric pressure, temperatures and concentrations will be retrieved more accurately for larger concentration, or more importantly, for larger pressure path lengths PxL. On the other hand, if the CO_2 4.3 μm is employed at atmospheric pressure, temperatures and concentrations will be retrieved more accurately for a small pressure path length. As shown in Fig. 2.6 for $x = 0.01$, the

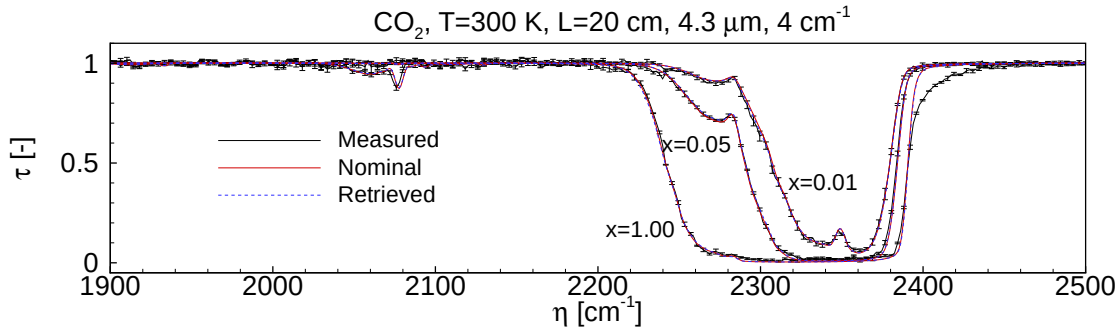

Figure 2.5: Comparison of retrieved transmissivity with measured transmissivity and nominal transmissivity calculated at the given temperature T=300 K for CO_2 4.3 μm band

Table 2.3: Inverse calculation results using Bharadwaj and Modest's transmissivity spectra [69, 70] for CO_2 at 600 K

Test condition (600 K)		Retrieved T (K)	Retrieved x	Error for T (%)	Error for x (%)
	x=0.01	650.36	0.0114	8.39	14.20
L=40 cm, 2.7 μm	x=0.05	607.42	0.0502	1.24	0.44
	x=1.00	588.79	1.0000	-1.87	0.00
	x=0.01	587.59	0.0100	-2.07	-0.10
L=40 cm, 4.3 μm	x=0.05	552.75	0.0624	-7.88	24.80
	x=1.00	585.65	1.0000	-2.39	0.00

CO_2 2.7 μm band is relatively weak at small concentrations,i.e., transmissivities will approach unity for this band and make the ill-posed radiation problem worse. For large PxL, as shown in Table 2.3 for the $x = 0.05$ and $x = 1.00$ cases, the results improve considerably. For the CO_2 4.3 μm band, it is seen that transmissivities tend toward zero for large parts of the band if concentration becomes large enough. Thus, for relatively high CO_2 concentrations, the CO_2 4.3 μm band will not be a good candidate to reconstruct temperatures and concentrations.

As mentioned before, higher temperature (1000 K, 1473 K, 1550 K, 1773 K) transmissivity data for CO_2 were measured at relatively high-resolution (nominal resolution $\Delta\eta = 0.125$ cm^{-1}) [71]. Normally the measurements were done twice, and reproducibility is very good (below 0.5% of difference). Baseline stability is about 0.002 [125]. The experimental uncertainties on transmissivity measurements were estimated to be within 5% at a unity transmissivity value [71]. After convolving these data into medium-resolution data, most of the random experimental noise is smoothed out. Examples for temperatures at 1000 K, 1473 K, 1550 K and 1773 K are shown in Figs. 2.8 to 2.18.

Temperatures are retrieved more accurately than concentrations using the CO_2 2.7 μm or 4.3 μm transmissivity bands at all temperatures, as shown in Tables 2.4 and 2.7. For the $x = 1.00$ cases, large differences are observed over the band center between the retrieved transmissivities and the measured one if the CO_2 2.7 μm band is employed, as shown in Figs. 2.8 and 2.17. Errors occur

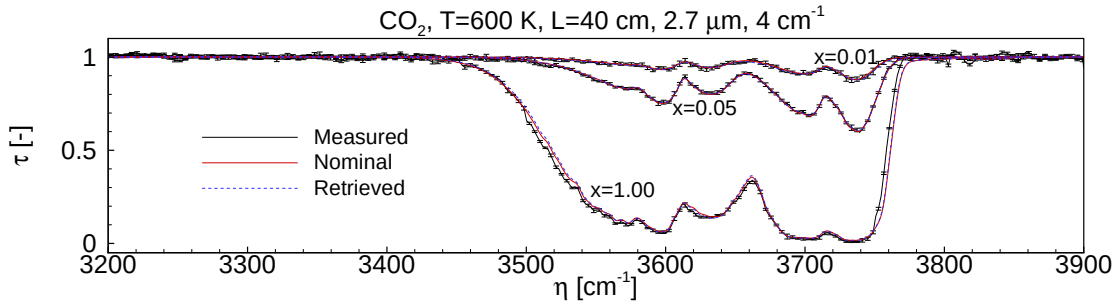

Figure 2.6: Comparison of retrieved transmissivity with measured transmissivity [69, 70] and nominal transmissivity calculated at the given temperature T=600 K for CO_2 2.7 μm band

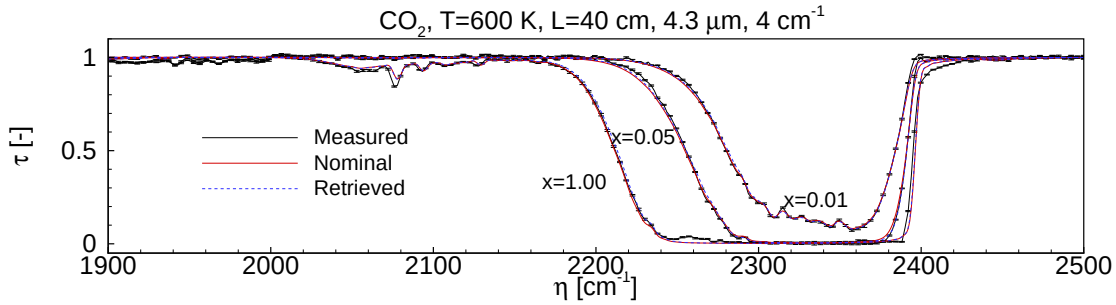

Figure 2.7: Comparison of retrieved transmissivity with measured transmissivity [69, 70] and nominal transmissivity calculated at the given temperature T=600 K for CO_2 4.3 μm band

when retrieving CO_2 temperature and concentration, but retrieved spectra are in good agreement with measured data for all the cases except for pure CO_2. For pure CO_2, limiting the retrieved concentrations to ≤ 1 makes retrieved temperatures higher than the nominal temperatures. The retrieved concentrations are larger than the nominal concentrations, which may indicate the actual pressure path length PxL (probably gas path length L due to the "soft" seal for the gas cell) is larger than the nominal pressure path length in the experiments or alternatively, HITEMP 2010 overestimates transmissivity (i.e., underestimates absorption coefficient) in these regions. Two independent measurements from Bharadwaj and Modest [70] and Fateev and Clausen [71] at temperatures 1000 K and 1550 K as shown in Figs. 2.9 and 2.15 respectively, both show HITEMP 2010 overestimates transmissivity at the CO_2 2.7 μm band center (Fateev and Clausen's [71] original data have a gas path length of 53.3 cm: in these figures they are scaled to 40 cm and 50 cm accordingly). This indicates these differences may be caused by incorrectly extrapolated intensities or missing hot lines in the HITEMP 2010 database. For the CO_2 4.3 μm band, although HITEMP 2010 also may overestimate transmissivities at the band center, transmissivities tend toward zero if concentration becomes large enough, which diminishes deviations between measured and nominal transmissivities at the

Table 2.4: Inverse calculation results using Fateev and Clausen's transmissivity spectra [71] for CO_2 at 1000 K

Test condition (1000 K)		Retrieved T (K)	Retrieved x	Error for T (%)	Error for x (%)
L=53.3 cm, 2.7 μm	x=0.01	975.62	0.0102	-2.44	2.30
	x=0.10	990.84	0.1076	-0.92	7.64
	x=1.00	1026.61	1.0000	2.66	0.00
L=53.3 cm, 4.3 μm	x=0.01	997.03	0.0106	-0.30	6.10
	x=0.10	995.48	0.1065	-0.45	6.49
	x=1.00	1005.94	1.0000	0.59	0.00

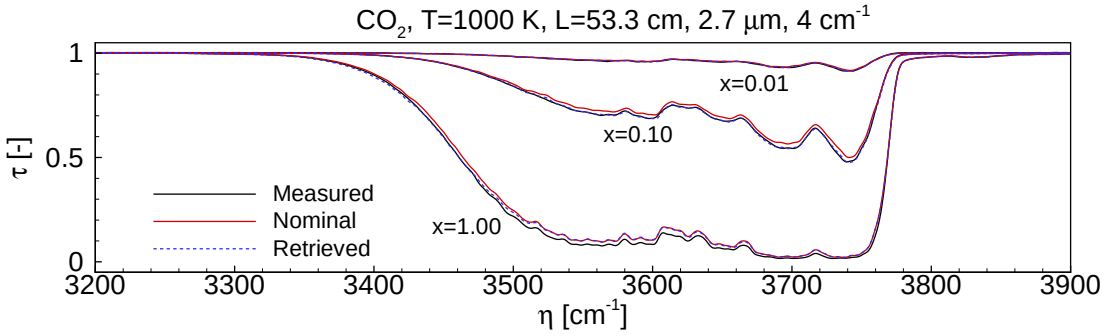

Figure 2.8: Comparison of retrieved transmissivity with measured transmissivity [71] and nominal transmissivity calculated at the given temperature T=1000 K for CO_2 2.7 μm band

band center. However, the deviations become more significant in the lower wavenumber range for the CO_2 4.3 μm band when temperatures are higher and concentrations larger. Two independent measurements at 1550 K for pure CO_2 show that HITEMP 2010 may overestimate transmissivity at this temperature also, as shown in Fig. 2.16, again perhaps due to missing lines or lines with incorrect strength in the database. Due to the fact that all retrieved concentrations are higher than the nominal concentrations and since accurate pre-mixed gases were used with "soft" seals at the ends, the actual gas path lengths may have been higher than 53.3 cm. However, despite measurement errors in the experiments or shortcomings of the database, temperatures can be retrieved fairly accurately and the errors for retrieved temperature are less than 4% for temperatures lower than 1550 K. For the even higher temperature of 1773 K, the deviations become larger, this causing retrieved temperatures to be less accurate than lower temperature data, as shown in Figs. 2.17, 2.18 and Table. 2.7.

Although errors occur when retrieving temperature and concentration from measured CO_2 transmissivity spectral data, the retrieved transmissivity spectra are in good agreement with the measured data. The mismatches between the measured and calculated transmissivities based on HITEMP 2010 are identified.

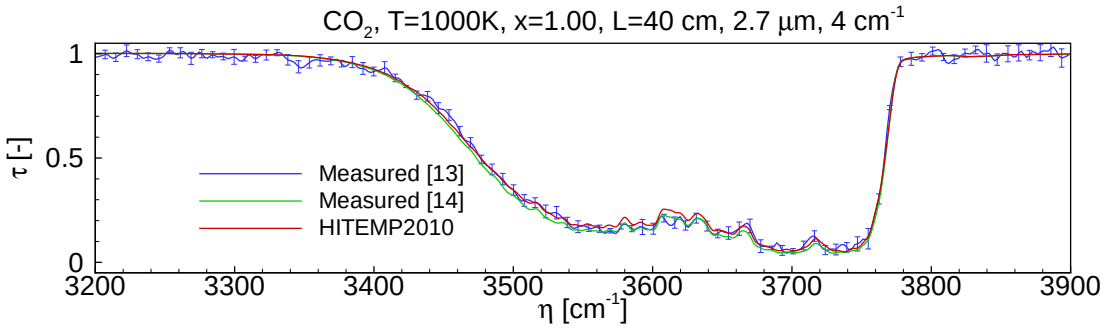

Figure 2.9: Comparison of two independently measured transmissivity [70, 71] with nominal transmissivity calculated at the given temperature T=1000 K for pure CO_2 2.7 μm band

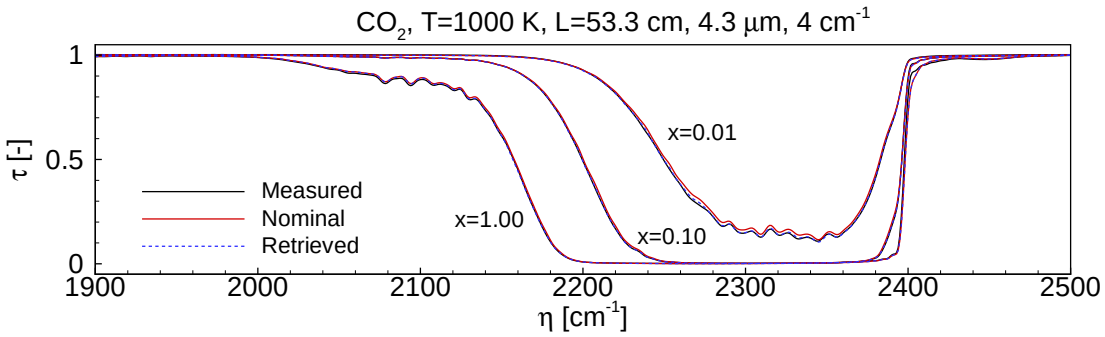

Figure 2.10: Comparison of retrieved transmissivity with measured transmissivity [71] and nominal transmissivity calculated at the given temperature T=1000 K for CO_2 4.3 μm band

Table 2.5: Inverse calculation results using Evseev and Fateev's transmissivity spectra [71] for CO_2 at 1473 K

Test condition (1473 K)		Retrieved T (K)	Retrieved x	Error for T (%)	Error for x (%)
L=53.3 cm, 2.7 μm	x=0.01	1460.28	0.0106	-0.86	6.10
	x=0.10	1464.59	0.1090	-0.57	8.98
	x=1.00	1529.91	1.0000	3.86	0.00
L=53.3 cm, 4.3 μm	x=0.01	1465.49	0.0107	-0.51	7.10
	x=0.10	1471.80	0.1068	-0.08	6.79
	x=1.00	1524.53	1.0000	3.50	0.00

2.3.3 Water Vapor

Two H_2O spectral bands at 1.8 μm and 2.7 μm are tested using transmissivity data measured by Bharadwaj and Modest [72], and Fateev and Clausen [73] at temperatures from 600 K to 1673 K.

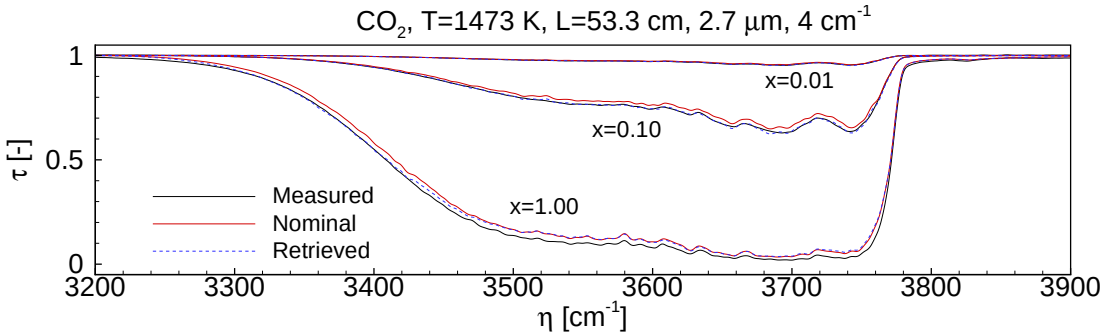

Figure 2.11: Comparison of retrieved transmissivity with measured transmissivity [71] and nominal transmissivity calculated at the given temperature T=1473 K for CO_2 2.7 μm band

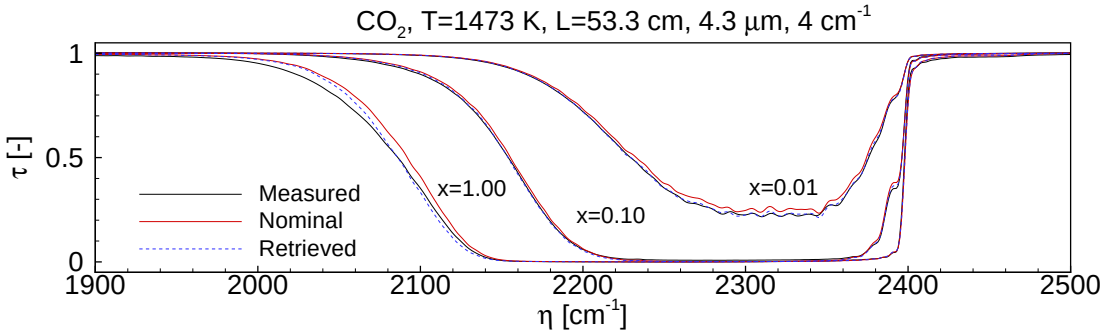

Figure 2.12: Comparison of retrieved transmissivity with measured transmissivity [71] and nominal transmissivity calculated at the given temperature T=1473 K for CO_2 4.3 μm band

Table 2.6: Inverse calculation results using Fateev and Clausen's transmissivity spectra [71] for CO_2 at 1550 K

Test condition (1550 K)		Retrieved T (K)	Retrieved x	Error for T (%)	Error for x (%)
L=53.3 cm, 2.7 μm	x=0.01	1545.04	0.0104	-0.32	4.20
	x=0.10	1532.24	0.1061	-1.15	6.13
	x=1.00	1600.94	1.0000	3.29	0.00
L=53.3 cm, 4.3 μm	x=0.01	1553.52	0.0101	0.23	1.10
	x=0.10	1548.48	0.1066	-0.10	6.57
	x=1.00	1610.14	1.0000	3.88	0.00

Table 2.8 shows the inverse results at three different temperatures. Here we show the results using medium-resolution (4 cm^{-1}) data at 600 K measured by Bharadwaj and Modest and convolved medium-resolution (4 cm^{-1}) transmissvities from Fateev and Clausen's measurements at 1073 K and 1673 K.

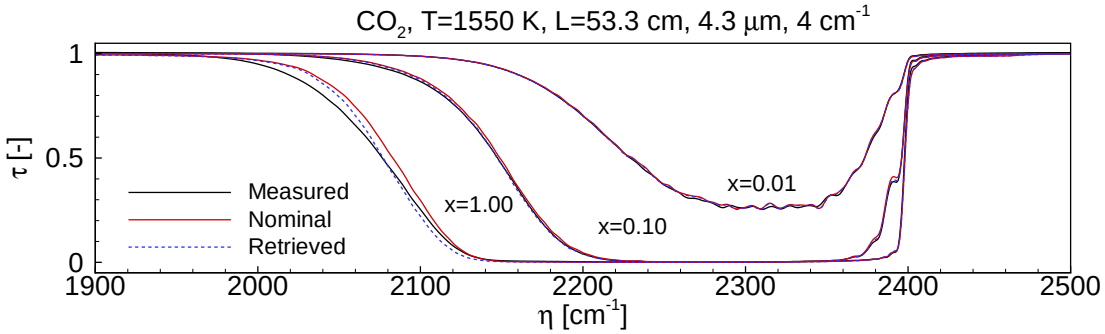

Figure 2.13: Comparison of retrieved transmissivity with measured transmissivity [71] and nominal transmissivity calculated at the given temperature T=1550 K for CO_2 4.3 μm band

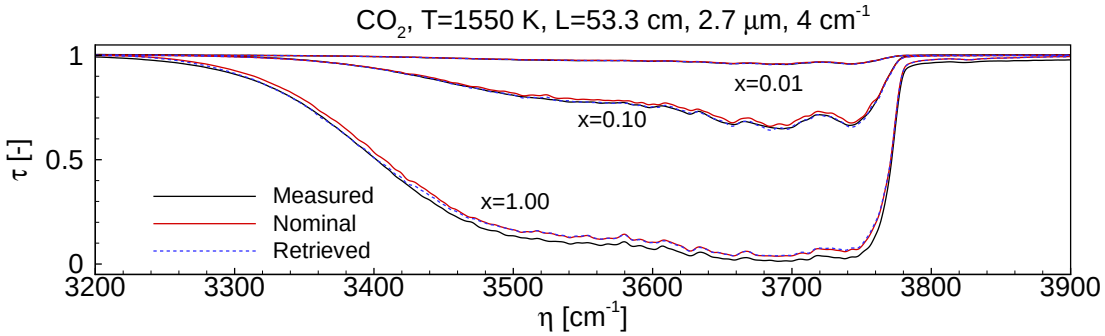

Figure 2.14: Comparison of retrieved transmissivity with measured transmissivity [71] and nominal transmissivity calculated at the given temperature T=1550 K for CO_2 2.7 μm band

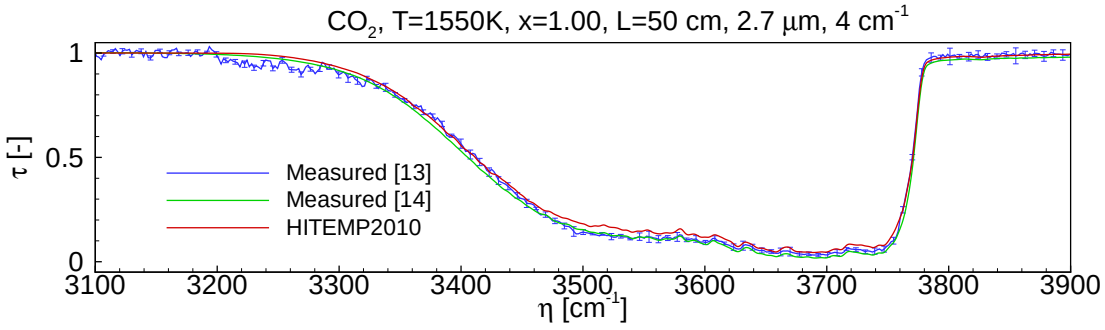

Figure 2.15: Comparison of two independently measured transmissivity [70,71] with nominal transmissivity calculated at the given temperature T=1550 K for pure CO_2 2.7 μm band

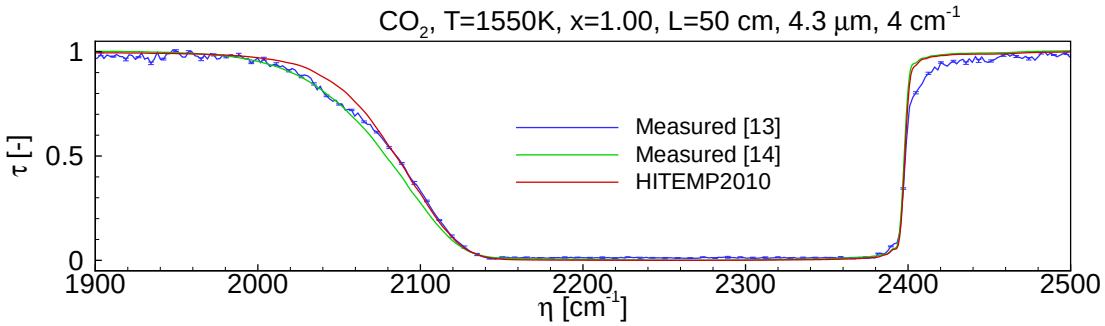

Figure 2.16: Comparison of two independently measured transmissivity [70,71] with nominal transmissivity calculated at the given temperature T=1550 K for pure the CO_2 4.3 μm band

Table 2.7: Inverse calculation results using Evseev and Fateev's transmissivity spectra [71] for CO_2 at 1773 K

Test condition (1773 K)		Retrieved T (K)	Retrieved x	Error for T (%)	Error for x (%)
L=53.3 cm, 2.7 μm	x=0.01	1646.38	0.0100	-7.14	0.40
	x=0.10	1686.77	0.1078	-4.86	7.84
	x=1.00	1734.29	1.0000	-2.18	0.00
L=53.3 cm, 4.3 μm	x=0.01	1679.62	0.0102	-5.27	1.90
	x=0.10	1689.54	0.1031	-4.71	3.10
	x=1.00	1822.31	1.0000	2.78	0.00

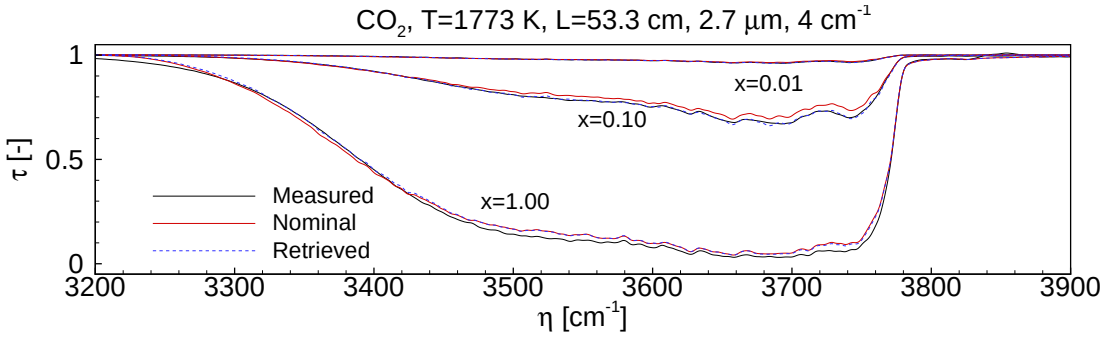

Figure 2.17: Comparison of retrieved transmissivity with measured transmissivity [71] and nominal transmissivity calculated at the given temperature T=1773 K for CO_2 2.7 μm band

Again, for Bharadwaj and Modest's measurements, the measured data include error bars, which are the experimental standard deviations of six different sets of transmission spectra, as shown in Figs 2.19 and 2.20 for the 1.8 μm and 2.7 μm band, respectively. The retrieved temperatures are fairly accurate. For concentration inversion, the measured transmissivities are smaller

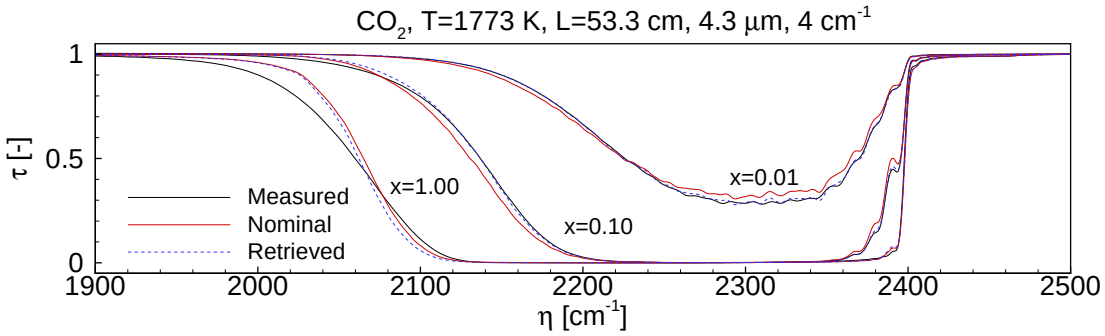

Figure 2.18: Comparison of retrieved transmissivity with measured transmissivity [71] and nominal transmissivity calculated at the given temperature T=1773 K for CO_2 4.3 μm band

than the nominal transmissivities for the H_2O 1.8 μm band (as shown in Fig. 2.19) and limiting the retrieved concentrations to ≤ 1, makes the retrieved concentration to be 1. Still, the retrieved transmissivities do not agree with the measured transmissivities very well. For the H_2O 2.7 μm band, the measured transmissivities are larger than the nominal transmissivities at the band center, which makes the retrieved concentration more than 10% less than unity. Since measured concentrations should be correct for $x = 1.00$, possible causes for the deviations include measurement uncertainty of temperatures and/or total pressures. The measurements were made over a period of 8-12 hours for each temperature, the experimental transmissivity in the band is corrected for the drifts of the intensity over time [72]. It is also possible that the wavenumber-based intensity drifts were not appropriately corrected for the band.

Table 2.8: Inverse calculation results using Bharadwaj and Modest's [72] and Fateev and Clausen's [73] transmissivity spectra for H_2O

Test condition (L=53.3 cm)		Retrieved T (K)	Retrieved x	Error for T (%)	Error for x (%)
T=600 K, x=1.00 [72]	1.8 μm	606.67	1.0000	1.11	0.00
	2.7 μm	610.89	0.8701	1.81	-12.99
T=1073K, x=0.35 [73]	1.8 μm	1117.95	0.3314	4.18	-5.31
	2.7 μm	1105.00	0.348	2.97	-0.57
T=1273K, x=0.35 [73]	1.8 μm	1350.48	0.3745	6.07	7.01
	2.7 μm	1331.26	0.3638	4.56	3.93
T=1473K, x=0.35 [73]	1.8 μm	1525.57	0.4690	3.56	34.00
	2.7 μm	1532.86	0.4175	4.05	19.30
T=1673 K, x=0.35 [73]	1.8 μm	1751.65	0.5007	4.69	43.05
	2.7 μm	1741.38	0.4171	4.08	19.17

Two H_2O spectral bands at 1.8 μm and 2.7 μm were tested using transmissivity data measured at temperatures from 1073 K to 1673 K and concentration at 0.35. Table 2.8 shows the inverse results. As shown in this table, temperatures are overestimated about 4% for all temperatures. As temperature increases, huge errors are obtained for concentration inversions; as large as 40% for the

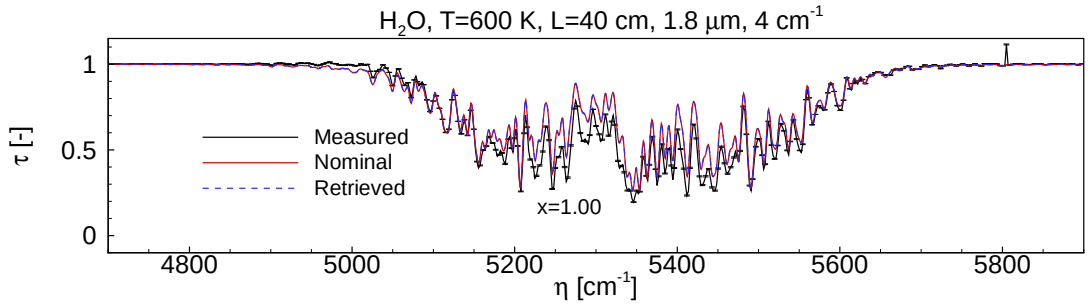

Figure 2.19: Comparison of retrieved transmissivity with measured transmissivity [72] and nominal transmissivity calculated at the given temperature T=600 K for H_2O 1.8 μm band

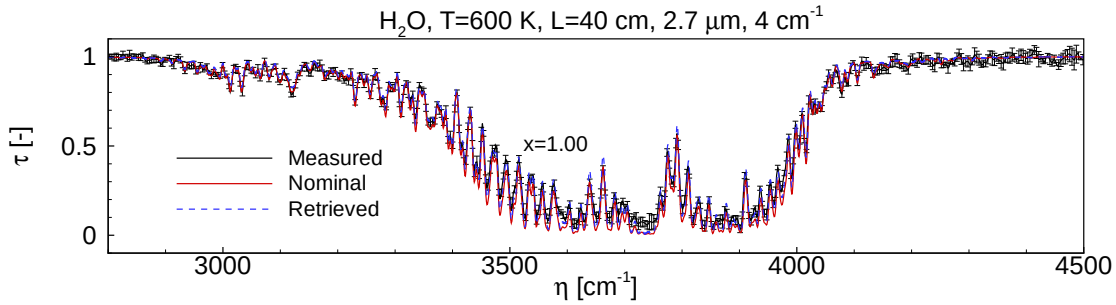

Figure 2.20: Comparison of retrieved transmissivity with measured transmissivity [72] and nominal transmissivity calculated at the given temperature T=600 K for H_2O 1.8 μm band

H_2O 1.8 μm band at 1673 K. If the H_2O 2.7 band is employed for temperatures higher than 1473 K, the error for retrieved concentrations is about 20%.

Figures 2.21, 2.23, 2.25 and 2.27 show the comparison of retrieved transmissivity with measured and nominal transmissivity for H_2O at 1.8 μm band and temperatures of 1073 K, 1273 K, 1473 K and 1673 K, respectively. Overall larger errors for concentrations inversion were obtained, however, the retrieved transmissivities always have better match with the measured transmissivities. The deviations between nominal and measured transmissivities become larger as temperature increases. The deviations between nominal and measured transmissivities at temperatures around 1000 K are relatively small. At higher temperatures, the deviations become larger both at the band center and band tails. Careful investigation of high-resolution transmissivity data at 1673 K indicates that HITEMP 2010 may fail to describe weak lines in the H_2O band tails and miss hot lines or underestimate line intensities in the band center at higher temperatures. Fig. 2.29 shows the measured and calculated high-resolution transmissivities at a temperature of 1673 K and H_2O concentration of 0.35 for small parts of the H_2O 1.8 μm band tails and center. The H_2O 1.8 μm band tails are shown in the upper and lower frames in Fig. 2.29, and the band center is shown in the

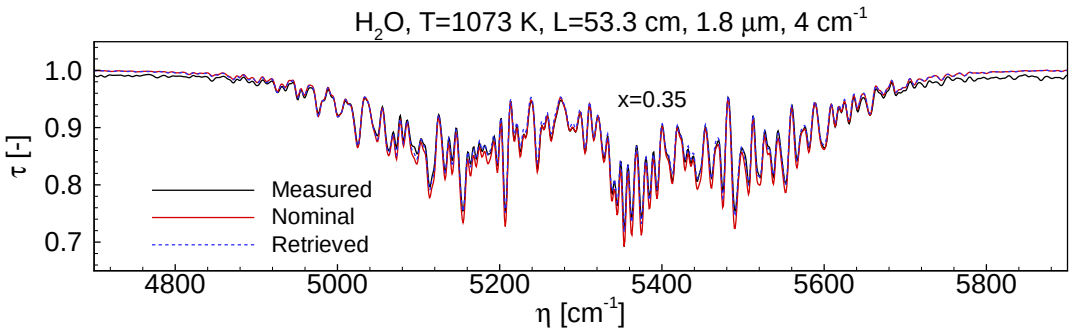

Figure 2.21: Comparison of retrieved transmissivity with measured transmissivity [73] and nominal transmissivity calculated at the given temperature T=1073 K for H_2O 1.8 μm band

middle frame. For the two band tails, the measured transmissvities contain a lot of weak H_2O lines which are missing in the HITEMP 2010 database. At the band center, it appears that intensities of hot lines are underestimated, which causes overestimation of transmissivities using HITEMP 2010.

Figures 2.22, 2.24, 2.26 and 2.28 show comparison of retrieved transmissivity with measured and nominal transmissivity for the H_2O 2.7 μm band at temperatures 1073 K, 1273 K, 1473 K and 1673 K, respectively. Compared to the H_2O 1.8 μm band, the H_2O 2.7 μm band is relatively strong and HITEMP 2010 is more accurate for this strong band. As shown in Table 5.4, the retrieved concentrations are relatively accurate at different temperatures if using H_2O 2.7 μm band instead of H_2O 1.8 μm band. For a temperature of 1073 K both retrieved temperature and concentration are very accurate. As temperature increases, the retrieved errors for concentration become larger. The deviations between nominal and measured transmissivities at temperatures around 1000 K are quite small. At higher temperatures, weak lines are missing at band tails and underestimation of absorption at the band center is also observed for the H_2O 2.7 μm band. Figure. 2.30 shows measured and calculated high-resolution transmissivities at 1673 K and H_2O concentration of 0.35 for small parts of the H_2O 2.7 μm band tails and center. The H_2O 2.7 μm band tails are shown in the upper and lower frames in Fig. 2.30, and the band center is shown in the middle frame. Although larger errors for concentrations inversion were obtained for higher temperatures, the retrieved transmissivities always have better agreement with the measured transmissivities.

Larger errors for concentration inversions were obtained at the higher temperature of 1673 K; as large as 40% for the H_2O 1.8 μm band and about 20% for the H_2O 2.7 band. At higher temperatures, the deviations become larger both at the band center and band tails, as shown in Figs. 2.27 and 2.28. Although it appears to be a baseline offset for the experimental data, careful investigation of high-resolution transmissivity data at 1673 K shows there is no significant offset for the high-resolution transmissivities. Figure 2.29 shows the measured and calculated high-resolution transmissivities at a temperature of 1673 K and H_2O concentration of 0.35 for small parts of the H_2O 1.8 μm band tails and center. The H_2O 1.8 μm band tails are shown in the upper and lower frames in Fig. 2.29, and the band center is shown in the middle frame. This indicates that the deviations may be caused by HITEMP 2010 failing to describe weak lines in the H_2O band tails and missing hot lines

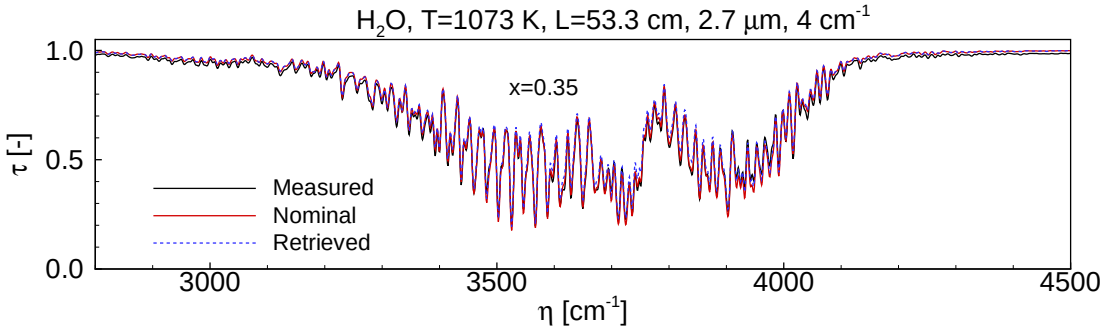

Figure 2.22: Comparison of retrieved transmissivity with measured transmissivity [73] and nominal transmissivity calculated at the given temperature T=1073 K for H_2O 2.7 μm band

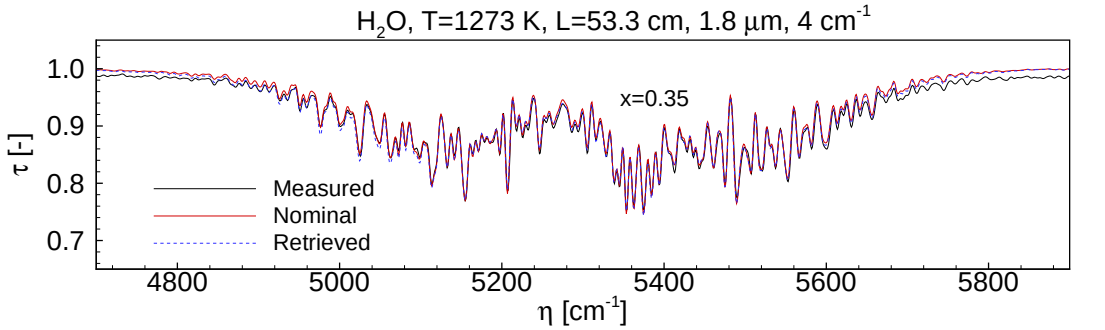

Figure 2.23: Comparison of retrieved transmissivity with measured transmissivity [73] and nominal transmissivity calculated at the given temperature T=1273 K for H_2O 1.8 μm band

or underestimating line intensities in the band center at higher temperatures. For the two band tails, the measured transmissivities contain a lot of weak H_2O lines which may be missing in the HITEMP 2010 database. Although some of the lines appear to be electronic noise in the measurements, the band tails do contain weak lines. As shown in Fig. 2.27, after convolving transmissivities into medium resolution, most of the electronic noise is smoothed out, the measured transmissivities are still consistently lower than the calculated transmissivities, which indicates that there are missing weak lines at the band tails in the HITEMP 2010 database. At the band center, it appears that intensities of hot lines are underestimated, which causes overestimation of transmissivities using the HITEMP 2010 database. This is also observed for the H_2O 2.7 μm band. Figure 2.30 shows measured and calculated high-resolution transmissivities for small parts of the H_2O 2.7 μm band tails and center; the band tails are shown in the upper and lower frames of Fig. 2.30, and the band center is shown in the middle frame. The deviations can also be caused by introducing errors during the experiments; more measurements at high resolution need to be conducted to validate the HITEMP 2010 database for H_2O spectral calculations at higher temperature, which is beyond the

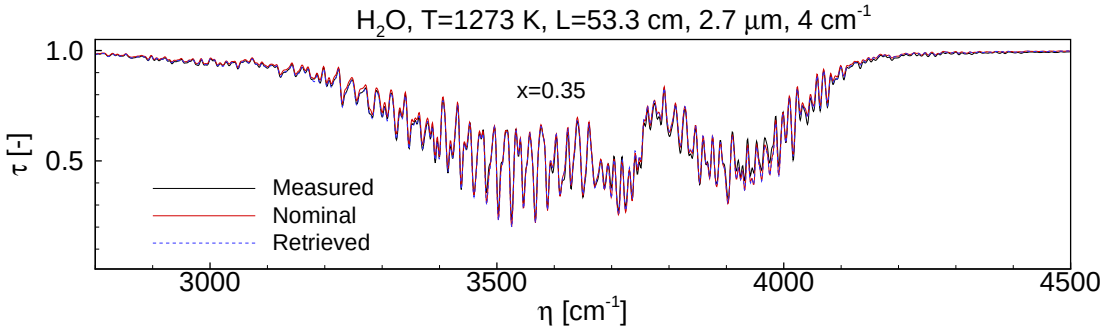

Figure 2.24: Comparison of retrieved transmissivity with measured transmissivity [73] and nominal transmissivity calculated at the given temperature T=1273 K for H_2O 2.7 μm band

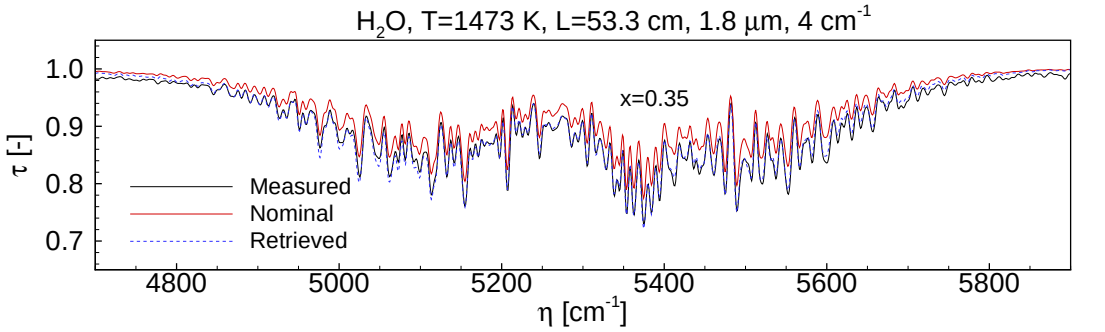

Figure 2.25: Comparison of retrieved transmissivity with measured transmissivity [73] and nominal transmissivity calculated at the given temperature T=1473 K for H_2O 1.8 μm band

scope of the present study. Although larger errors for concentration inversion were obtained for higher temperatures, the retrieved transmissivities always have better agreement with the measured transmissivities.

2.4 Inverse radiation model for gas mixture

The previous study applies to a single combustion species. However, combustion products usually are mixtures of several gas species. In this section, the previous model is extended to retrieve temperature, species concentrations for a gas mixture of the three major combustion products CO_2, H_2O and CO mixed with N_2. The spectral absorption coefficient for the gas mixture is

$$\kappa_\eta(T, \mathbf{x}) = \kappa_\eta\left(T, x_{CO_2}\right) + \kappa_\eta\left(T, x_{H_2O}\right) + \kappa_\eta\left(T, x_{CO}\right) \tag{2.15}$$

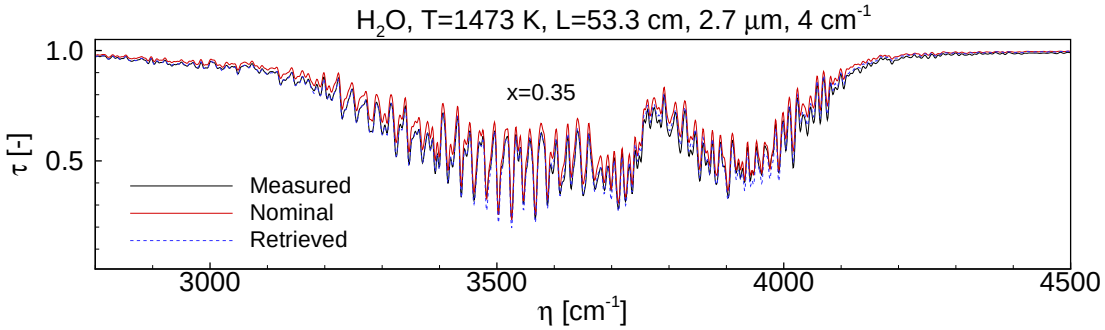

Figure 2.26: Comparison of retrieved transmissivity with measured transmissivity [73] and nominal transmissivity calculated at the given temperature T=1473 K for H_2O 2.7 μm band

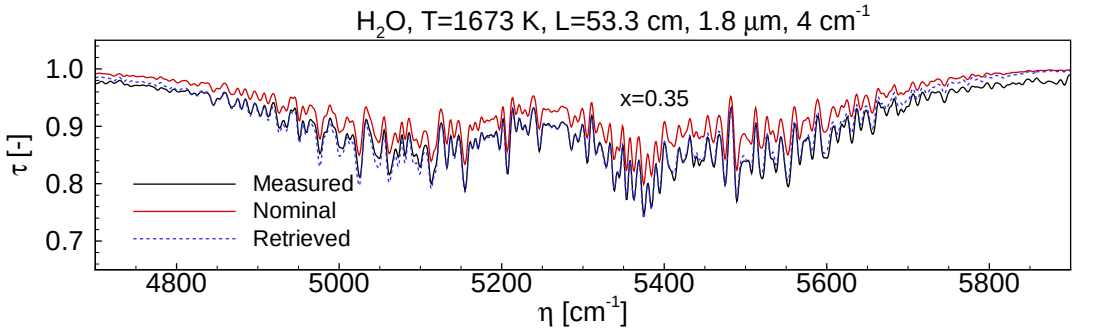

Figure 2.27: Comparison of retrieved transmissivity with measured transmissivity [73] and nominal transmissivity calculated at the given temperature T=1673 K for H_2O 1.8 μm band

where $\mathbf{x} = [x_{CO_2}, x_{H_2O}, x_{CO}]$ is a set consisting of all the species concentrations. Therefore, the spectral transmissvities for the gas mixture are

$$\tau_\eta(T, \mathbf{x}) = e^{-\kappa_\eta(T,\mathbf{x})L} \tag{2.16}$$

Compared to Eq. (2.1) Eq. (2.16) introduces two more species concentrations. A similar approach as described in Section 2.2.2 (for now 4 other than 2 parameters) can be applied to retrieve temperature and species concentrations for the gas mixture of CO_2, H_2O and CO. Since in the spectral interval 1800 cm^{-1}– 2500 cm^{-1}, all the three species have spectral bands, as shown in Fig. 1.2, this part of the spectrum was selected to study the accuracy and capability of retrieving temperature and species concentrations for a gas mixture. An artificial case was generated at a given temperature T=1500 K for a gas mixture containing 10% CO_2+10% H_2O+5% CO at atmospheric pressure for a 100-cm gas column. "Measured" transmissivities were synthesized with 5% of artificial random noise. The generated spectrum was used to retrieve temperature and concentrations

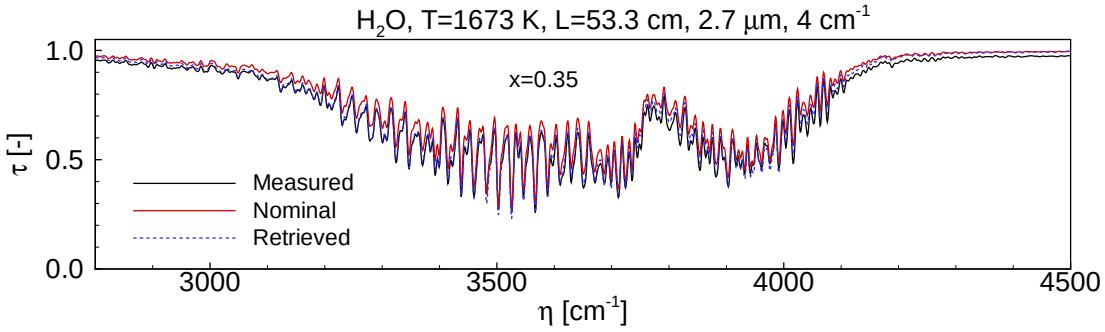

Figure 2.28: Comparison of retrieved transmissivity with measured transmissivity [73] and nominal transmissivity calculated at the given temperature T=1673 K for H_2O 2.7 μm band

for the three combustion species. Temperature and all the species concentrations can be retrieved simultaneously and the inverse results are shown in Table 2.9. Figure 2.31 shows comparison of retrieved transmissivity with "measured" and nominal transmissivity for the gas mixture. Although the "measured" data include considerable noise, the retrieved spectrum is in good agreement with the nominal one and the inverse results are within an error of 5%.

Table 2.9: Inverse calculation results for retrieving temperatures, species concentrations for a gas mixture of 10% CO_2+10% H_2O+5% CO

retrieved parameters	T (K)	x_{CO_2}	x_{H_2O}	x_{CO}
Test conditions	1500.00	0.1000	0.1000	0.0500
retrieved	1498.97	0.0957	0.0998	0.0490
error(%)	−0.07	−4.29	−0.18	−1.92

2.5 Real-time Temperature Reconstruction for Homogeneous Media

Real-time measurements of temperature and species concentration are an important challenge in combustion systems. It is difficult to make quantitatively accurate nonintrusive measurements of temperature and species concentration in real time . Although measurements of the transmissivity of rotational spectral lines of a gas can reveal its temperature and concentration, usually measured transmissivity have considerable noise, which can significantly affect the accuracy of the retrieved temperature and concentration. Here we present an inverse calculation model based on the efficient Levenberg-Marquardt inverse method with a Kalman filter technique to retrieve temperature and species concentration in real time for a transient system. A significant increase in the accuracy of inverse results can be achieved through the filtering method that include constraints from *a priori* knowledge plus measurements.

Usually the measured transmissivity Y_i in Eq. (2.10) have considerable noise, which can significantly affect the accuracy of the retrieved temperature and concentration. As shown in Fig. 2.32,

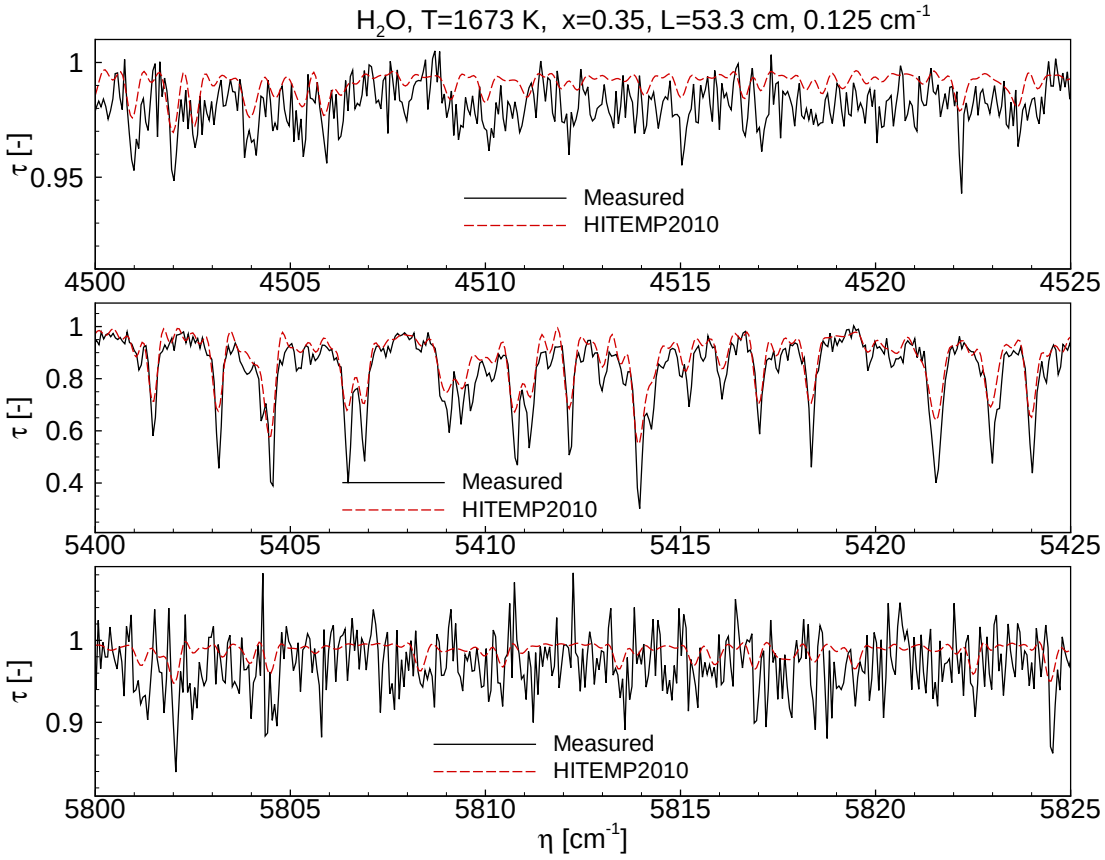

Figure 2.29: Comparison of calculated and measured high-resolution (nominal resolution $\Delta\eta$ = 0.125 cm^{-1}) transmissivity [73] at the given temperature T=1673 K and concentration x=0.35 for H_2O 1.8 μm band

based on single measurements to retrieve temperature, the state vector **z** evolves in a random way with considerable noise. To sequentially estimate temperature and concentration, if all available single measurements are used together with prior knowledge of the system, the error can be minimized in a statistical manner through the widely known Kalman filter approach.

2.5.1 The Kalman Filter Approach

For the application of a Kalman filter, the prediction and the measurement models are assumed to be linear. It assumes that the state vector evolves from the prior state with Gaussian distributed processing noise **v**, which has zero mean and is additive. Like the processing noise, the measurement noise **n** is also assumed to be zero mean Gaussian white noise. With all these

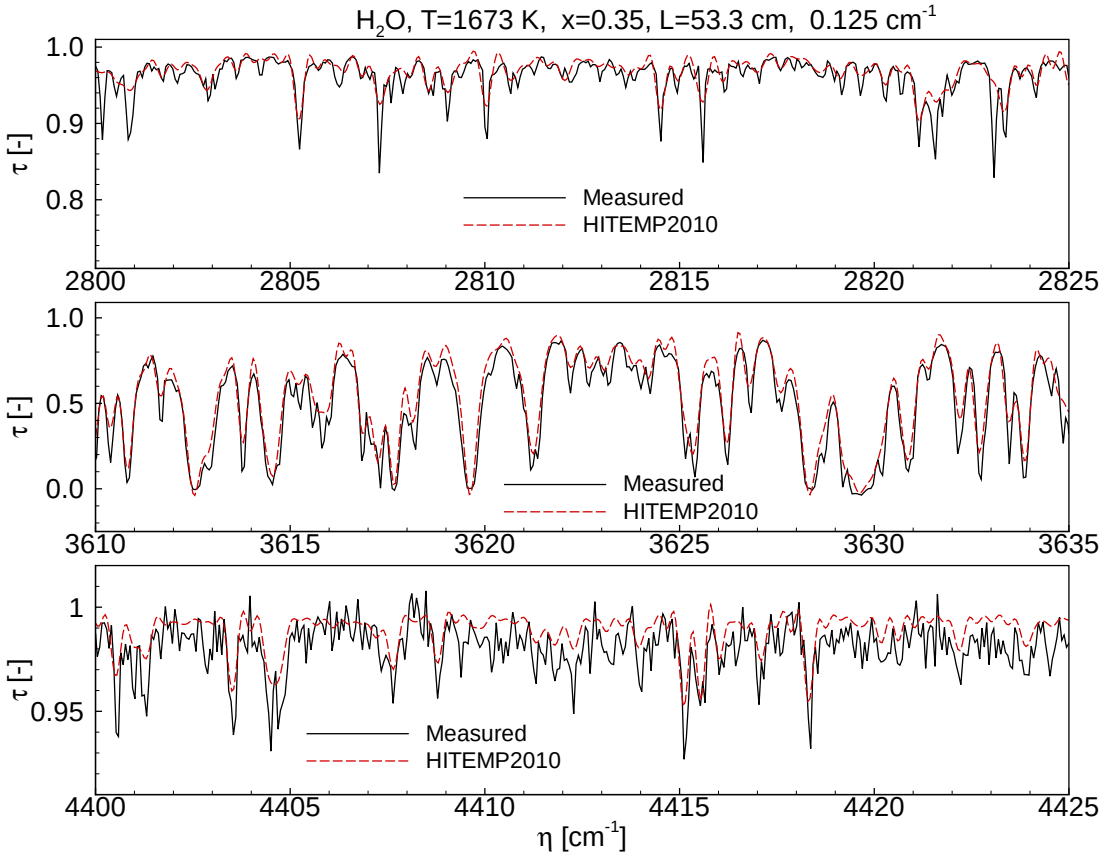

Figure 2.30: Comparison of calculated and measured high-resolution (nominal resolution $\Delta\eta$ = 0.125 cm^{-1}) transmissivity [73] at the given temperature T=1673 K and concentration x=0.35 for H_2O 2.7 μm band

assumptions, the prediction and measurement models can be written respectively as:

$$\mathbf{a}_k = \mathbf{F}_k\mathbf{a}_{k-1} + \mathbf{s}_k + \mathbf{v}_{k-1} \tag{2.17a}$$

$$\mathbf{z}_k = \mathbf{A}_k\mathbf{a}_k + \mathbf{n}_k \tag{2.17b}$$

where **F** is the state transition matrix. Because the state transition information is not known, so it is simply assumed that the state remains constant over time, i.e., **F**=**I** is an identity matrix. **A** is the transformation matrix that maps the state vector parameters into the measurement domain. In the inverse calculation model, temperature and species concentration are retrieved from transmissivity spectra at each time step. The retrieved temperature and concentration are treated as measurements data. In this case, the transformation matrix is also an identity matrix. **s** is a known vector of inputs. Here **a** and **z** are state vectors of temperature and concentration $(x, T)^T$ from prediction and measurement. By assuming that the noises **v** and **n** have zero means and covariance matrices **Q** and **R**,

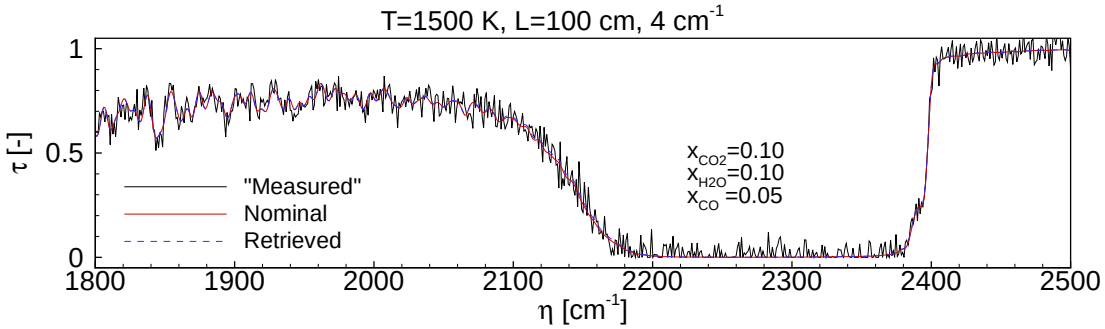

Figure 2.31: Comparison of retrieved transmissivity with "measured" transmissivity (synthetic) and nominal transmissivity calculated at the given temperature T=1500 K for a gas mixture of 10% CO_2+10% H_2O+5% CO for the spectral interval 1800 cm^{-1}– 2500 cm^{-1}

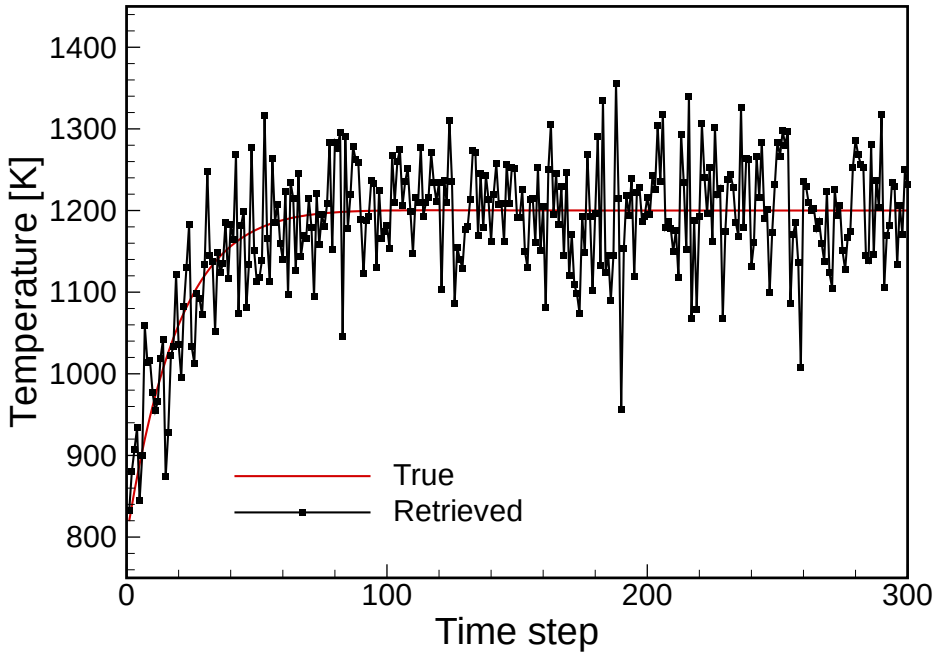

Figure 2.32: Comparison of retrieved temperature evolution based on single measurements with true temperature evolution

respectively, the prediction and update steps of the Kalman filter are given by:

Prediction:

$$\mathbf{a}_k^- = \mathbf{F}_k \hat{\mathbf{a}}_{k-1} + \mathbf{s}_k \tag{2.18a}$$

$$\mathbf{P}_k^- = \mathbf{F}_k \mathbf{p}_{k-1} \mathbf{F}_k^T + \mathbf{Q}_k \tag{2.18b}$$

Update:

$$\mathbf{K}_k = \mathbf{P}_k^- \mathbf{A}_k^T \left(\mathbf{A}_k \mathbf{P}_k^- \mathbf{A}_k^T + \mathbf{R}_k \right)^{-1} \tag{2.19a}$$

$$\hat{\mathbf{a}}_k = \mathbf{a}_k^- + \mathbf{K}_k \left(\mathbf{z}_k - \mathbf{A}_k \mathbf{a}_k^- \right) \tag{2.19b}$$

$$\mathbf{P}_k = \left(\mathbf{I} - \mathbf{K}_k \mathbf{A}_k \right) \mathbf{P}_k^- \tag{2.19c}$$

The matrix **K** is called Kalman's gain matrix. Notice above that after predicting the state variable **a** and its covariance matrix **P** with equations, a *posteriori* estimates for such quantities are obtained in the update step with the utilization of the "measurements" **z**. The symbols " ˆ " above indicates an estimate of the state vector

2.5.2 Test Cases

Kalman filters use constraints from *a priori* knowledge plus measurements to make an optimal estimation of the state evolution. The prediction noise **v** and measurements noise **n** in Eq. (2.17) are very important for a successful estimation. In this study, we only retrieve temperature at each time step (species concentration can be retrieved in the same fashion), so the covariance **Q** and **R** become two scalars. The relative value **Q**/**R** has significant effect on the performance of the filtered solution. Because we assume that temperature stays constant from one time step to the next, this assumption is only truly valid at steady state condition. For time-varying states, the prediction noise can be very large. If the prediction noise is much larger than the measurement noise (measurements are more believable than predictions), the retrieved temperature from the Kalman filter will pretty much follow the measurement, as shown in Fig. 2.33 (a). Otherwise, if the predication noise is much smaller than the measurement noise, as shown in Fig. 2.33 (c), until temperature reach steady state, the predicted temperatures by Kalman filter have very large discrepancies from the true temperatures. For a medium **Q**/**R**, as shown in Fig. 2.33 (b), the temperature varies more smoothly as compared to Fig. 2.33 (a) and is resolved more accurately before steady state as compared to Fig. 2.33 (c). But at steady state, temperature also evolves with considerable noise.

In order to retrieve temperature more accurately before and at steady state condition, it is appropriate to using varying **Q**/**R** for the prediction of temperatures. As shown in Fig. 2.33 (d), larger **Q**/**R** are used for the Kalman filter method before temperature reaches steady state. After temperature reach steady state, the assumption of the state transition function is more accurate and thus a smaller **Q**/**R** leads to a better prediction of temperatures.

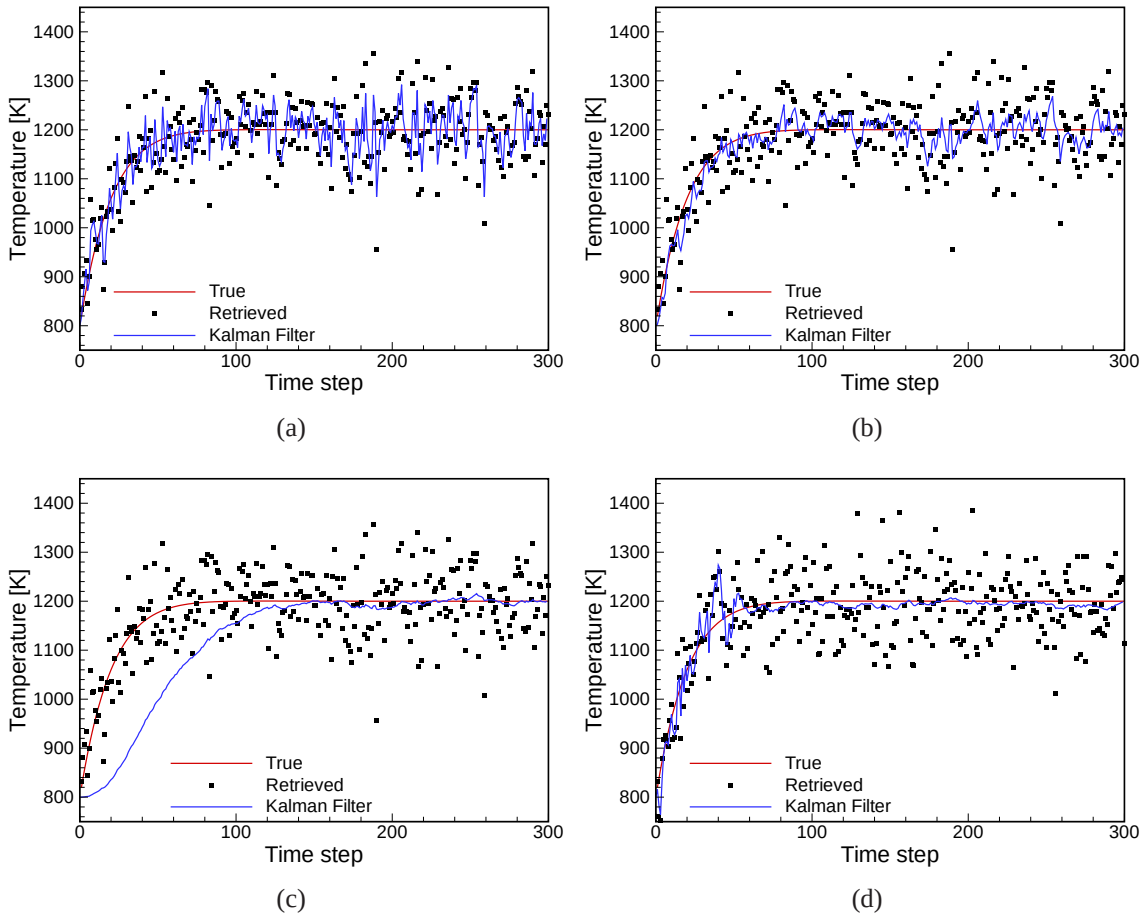

Figure 2.33: (a): **Q**/**R**=1, (b): **Q**/**R**=1/100, (c): **Q**/**R**=1/1000, (d): varying **Q**/**R**

2.6 Summary

An inverse radiation model was developed by applying the Levenberg-Marquardt scheme for temperature and concentration inversion in combustion gases. The model was validated by retrieving temperatures and gas concentrations using previously measured transmissivity data over a wide range of temperatures and gas concentrations for the CO_2 2.7 μm and 4.3 μm bands, and the H_2O 1.8 μm and 2.7 μm bands. Although the retrieved temperatures and concentrations display large differences compared to the nominal experimental conditions in some cases, good agreement between measured and retrieved transmissivities was observed. The resulting inverse radiation model provides a reliable tool for temperature and concentration prediction. By employing the Kalman filter approach, the model was extended for retrieving scalar parameters for a transient system in real-time.

Chapter 3

Optimal Spectral Parameters Investigations

3.1 Introduction

The developed inverse radiation tool for homogeneous media in the previous chapter is used to identify optimal spectral bands and resolutions for a variety of gas species and conditions of interest. Radiation spectra usually contain several emission bands for common combustion gases, such as CO_2, H_2O and CO in the infrared range. After inverse algorithms are developed, they can be used to determine which bands are optimal for inverse calculations at what conditions. For example, the CO_2 4.3 μm band is a relatively strong band and, while it can be used for inverse calculations, in the presence of high CO_2 concentrations the transmissivity becomes highly saturated, masking spectral information, and making the ill-posed inverse radiation calculations even more challenging. Therefore, optimal spectral bands for particular combustion conditions need to be determined before more complicated experiments are conducted, and before the model is extended to nonhomogeneous media. As indicated, optimal spectral resolution will depend on given conditions. Finer spectral resolution may contain information for each individual transition lines and will resolve more spectral information. However, these spectral data are based on quantum mechanics calculations and experimental measurements, it is subject to some degree of theoretical uncertainties. This may be smoothed out by a coarse resolution measurement. While coarse resolution also requires less collection times, on the other hand, one may not resolve some important spectral information.

Synthetic spectral transmission signals are generated for different medium-to-coarse resolutions using rovibrational band spectra created from HITEMP2010 to simulate the transmissivities measured by a Fourier transform infrared (FTIR) spectrometer. The simulated data are disturbed with random noise to represent measurement noise inevitable in an experimental setting. Experimental measurement drifts both on transmissivities and wavenumbers are also considered to investigate their effects on temperature and concentration inversion. Ideal FTIR instrument line shape (ILS) functions are used to convolve the high-resolution transmissivity spectra to generate different medium-to-coarse resolutions of FTIR transmissivity spectra for the CO_2 4.3 μm and 2.7 μm bands, H_2O 2.7 μm and 1.8 μm bands, and CO 4.7 μm and 2.3 μm bands. The goal of this study is to conduct a systematic investigation to determine what spectral range measured at what resolu-

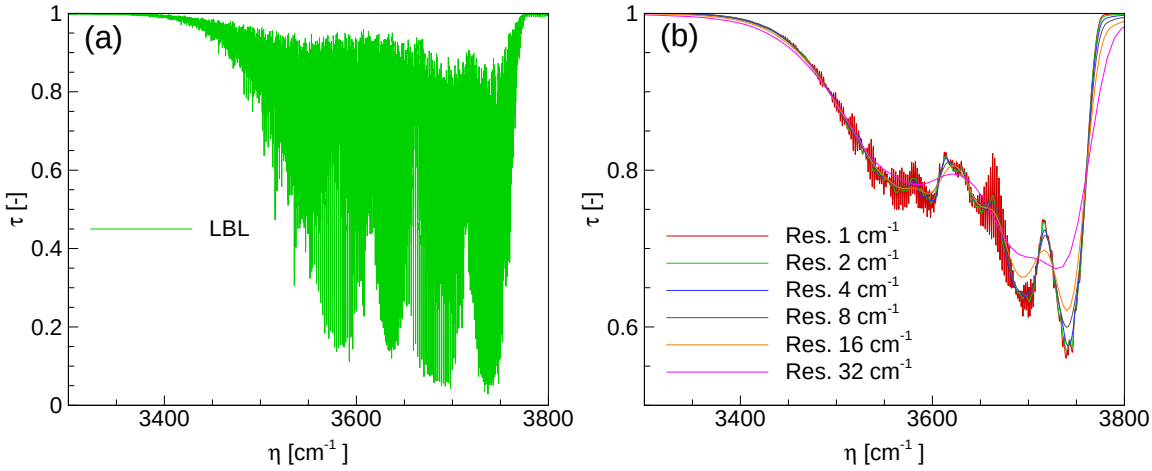

Figure 3.1: Spectral transmissivity for CO_2 2.7μm band. (a): High resolution transmissivity from LBL database (b): Convoluted transmissivity with ILS functions

tion for what species leads to the most accurate reconstruction of the underlying temperature and concentration fields.

3.2 Spectral Resolutions

Equation (2.7) describes the ILS for an ideal instrument. In the present study, we do not actually obtain spectra with an FTIR but, we create synthetic spectra by simulating how an FTIR measures a spectrum. Synthetic spectra were created by convolving high-resolution transmissivity spectra with the ideal ILS functions of 1, 2, 4, 8, 16 or 32 cm^{-1} resolution. As an example, Fig. 3.1 shows spectral transmissivities for a N_2-CO_2 mixture containing 40% CO_2 at 1 bar and a temperature of 1000K for the 2.7μm band. The band, as calculated from the HITEMP2010 LBL database, exhibits the precise line shape of transmissivities, while after convolution smoother averaged shapes with diminishing structures are obtained. While the fine resolution has a very distinct structure, which can be exploited for inversion, this fine structure is subject to theoretical uncertainty, such as calculated values for line strengths, shapes and widths. Fine resolution is also more susceptible to experimental noise, and requires large collection times. Therefore, one may expect that a resolution exists, which is fine enough for reconstruction of temperature and concentration, and also coarse enough to save measurement and computational times.

3.3 Spectral Bands for Combustion Gases

In order to use combustion gases like CO_2, H_2O and CO as the media for reconstruction of temperature and concentration, the ideal spectral band should be spectrally distinct at different

temperatures and concentrations. For transmission measurements, the band cannot be very strong, otherwise it will be saturated and will approach zero over much of the band; it also cannot be too weak or transmissivity will approach unity for a large part of the band, again making it no longer spectrally distinct. Figure 3.2 shows the possible candidates of spectral bands for three different combustion gases. CO_2 has three bands in the range of interest: the 4.3 μm, 2.7 μm and 2.0 μm bands, as shown in Fig. 3.2(a). The 2.0 μm band holds little promise at least at atmospheric pressure, because the band is too weak even for high concentrations and large path lengths. As shown in Fig. 3.2(b), H_2O bands are wider and spread out over much of the spectrum. It also has three bands in the range of interest: the 6.3 μm, 2.7 μm and 1.8 μm bands. The 6.3 μm band is a strong band but in the region beyond 6 μm. As mentioned before, because of transmission limits of optical windows and limited detector ranges, wavelengths beyond 6 μm tend to be less useful. The performance of using the other two bands for inverse calculations may depend on the temperature and concentration conditions. The CO 4.7 μm band is a relatively strong band and has distinct temperature trends, as shown in Fig. 3.2(c), which may make it a good candidate for reconstruction of temperature and concentration. By contrast, the CO 2.3 μm band may be too weak. For a measured CO spectrum, the signal-to-noise ratio for the CO 2.3 μm band may be too small, and makes it very difficulty and inaccurate to retrieve temperature and concentration from this band. The appropriateness of these bands of different species depends on the temperature T and pressure path length PxL, defined as the product of the partial pressure and gas path length, and needs to be investigated.

Figure 3.3 shows transmissivity spectra for several temperatures and two different concentrations for the CO_2 4.3 μm band. The transmissivity data show very distinct temperature trends at lower concentrations for the CO_2 4.3 μm band, but it is seen that transmissivities tend toward zero for large parts of the band if concentration or, most importantly, the pressure path length becomes large enough. Thus, for relatively high pressure path lengths, the CO_2 4.3 μm band will not be a good candidate to reconstruct temperatures and concentrations.

Consequently, it is critical to quantitatively investigate the performance of each band for the reconstruction of temperature and concentration. In this study, two bands for CO_2 (4.3 μm and 2.7 μm), two bands for H_2O (2.7 μm and 1.8 μm), and two bands for CO (4.7 μm and 2.3 μm) will be studied for varying temperatures between 550K−2350K and varying gas pressure path length from 0.2 bar·cm to about 100 bar·cm to determine the optimal spectral band for each individual combustion gas for temperature and concentration inversion.

3.4 Results and Discussion

A systematic study was conducted by retrieving gas temperature and concentration using the developed inverse method to investigate the optimal spectral bands and resolutions for inverse calculations. Artificial drifts on both transmissivities and wavenumbers were created to simulate systematic error, and Gaussian random noise was added to the transmissivity spectra to simulate the random error inevitable in experiments.

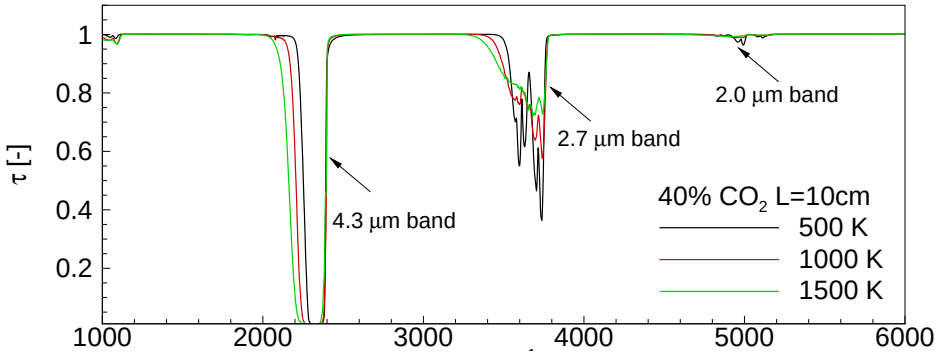

(a) transmissivity spectrum for CO_2

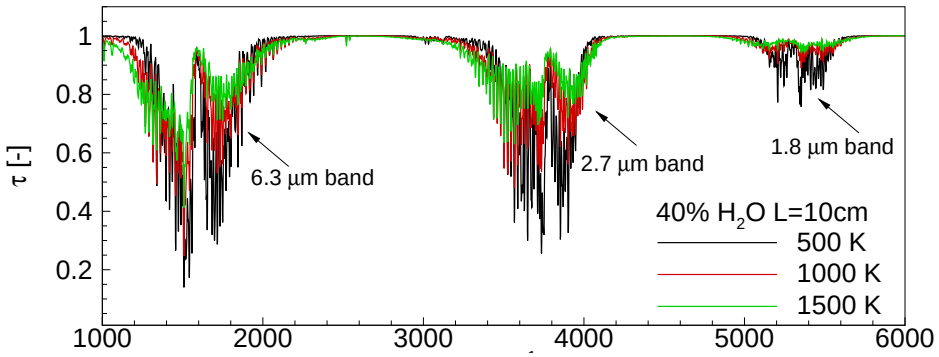

(b) transmissivity spectrum for H_2O

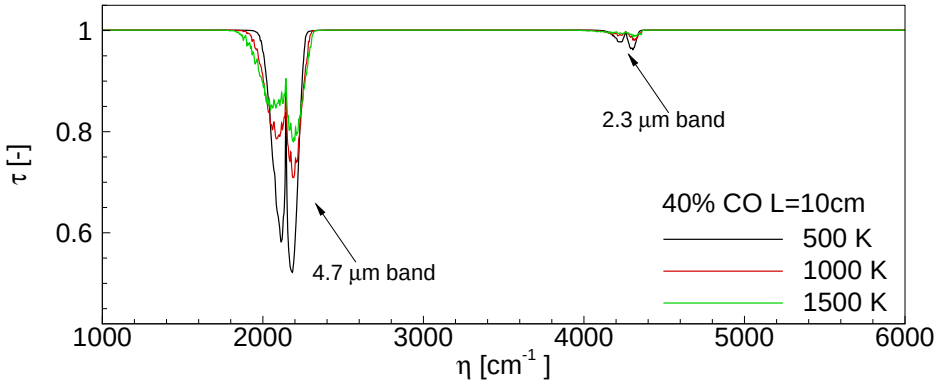

(c) transmissivity spectrum for CO

Figure 3.2: Spectral transmissivity bands for combustion gases

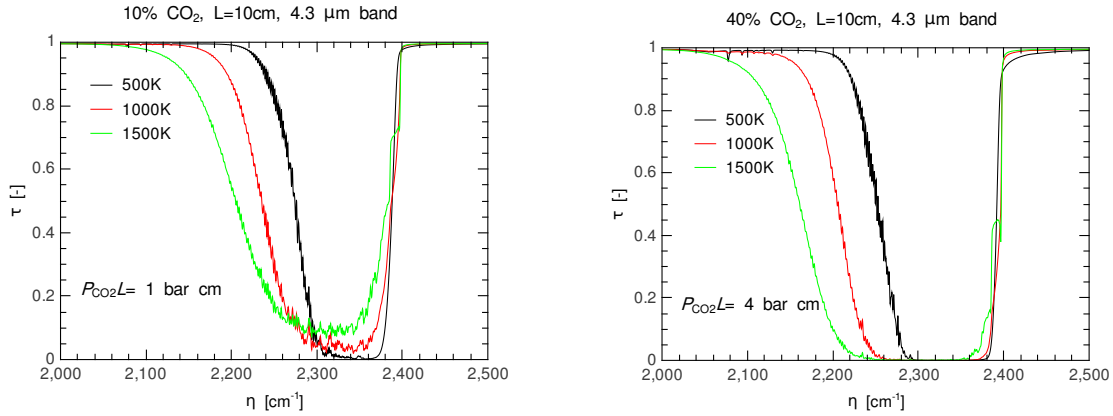

Figure 3.3: Spectral transmissivity of CO_2 4.3 μm band for a homogeneous gas path length of L=10 cm, Res= 1cm^{-1}

Systematic Error

The case of a homogeneous 10-cm-long CO_2 gas path of temperature 1050 K and 10% concentration using CO_2 4.3 μm band was studied to investigate the effects of experimental measurement drifts on the inverse results. Different amounts of artificial drift on both transmissivities τ and wavenumbers η were created for the synthetic spectra. The errors for retrieved temperature and concentration as shown in Figs. 3.4 and 3.5, indicate that:

1. The developed inverse method converges to the correct solution when there are no errors present in the measured spectral transmissivity.

2. A positive drift on transmissivities will lead to an overestimation of the temperature and an underestimation of the concentration and vice versa.

3. When there is a drift in transmissivities, the inverse results get worse with coarser resolution.

4. Measurement drift error on transmissivities has larger effects on the concentration prediction than on temperature prediction. This is to be expected, since the absorption coefficient (and, thus, transmissivity) is directly proportional to concentration.

5. A left drift in wavenumbers will lead to an underestimation of the temperature and an overestimation of the concentration and vice versa.

6. When there is a drift in wavenumbers, the inverse results are only weakly dependent on what resolution is used for the inverse calculation.

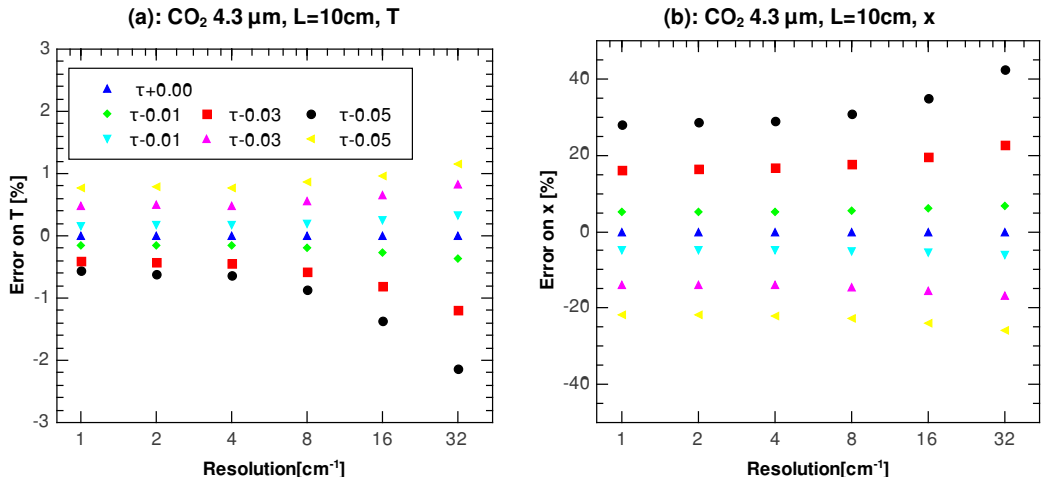

Figure 3.4: Temperature and concentration inversion with drift subjects to transmissivities

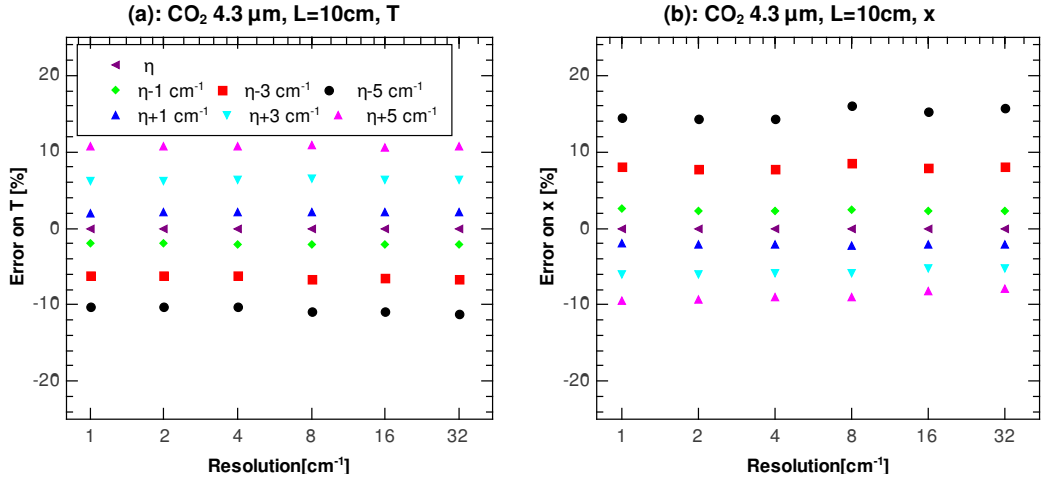

Figure 3.5: Temperature and concentration inversion with drift subjects to wavenumbers

Random Error

Absorption coefficients taken from the high-resolution LBL database were used to calculate transmissivity spectra for a homogeneous gas path of L=10 cm and L=320 cm length. After spectra are convolved with the ideal ILS function, Gaussian random noise with zero mean and 5% standard deviation was added to the convolved spectra. These convoluted spectra with noise were used as input data instead of actually measured transmissivity spectra from an FTIR. Several spectral bands for three combustion species were investigated for a large range of temperatures and concentrations,

with different spectral resolutions. All cases studied are summarized in Table 3.1.

Table 3.1: Summary of the test cases

Species	CO_2, H_2O and CO
Total pressure (P)	1 bar
Temperature (T)	linearly increased from 550 to 2350K
Concentration (x)	0.02, 0.04, 0.08, 0.16, 0.32
Gas path length (L)	10cm, 320cm
Resolution (Res)	1, 2, 4, 8, 16, 32 cm^{-1}
Spectral bands	CO_2: 4.3μm, 2.7μm H_2O: 2.7μm, 1.8μm CO: 4.7μm, 2.3μm
Noise	5% Gaussian random noise

In this study, temperature and concentration were retrieved simultaneously and the $Error$ revealing the performance of the inverse calculation is defined as,

$$Error = \sqrt{\frac{1}{2}\left[\left(\frac{\sum_j^N \mid T_j - T_{exact} \mid}{NT_{exact}}\right)^2 + \left(\frac{\sum_j^N \mid x_j - x_{exact} \mid}{Nx_{exact}}\right)^2\right]} \tag{3.1}$$

Where T_{exact} and x_{exact} are the exact values for temperature and concentration. For each case, N=100 different "measurements" were employed and T_j and x_j are the retrieved temperature and concentration for the jth "measurement". Thus, $Error$ can be viewed as an average error when one retrieves temperature and concentration. On the other hand, results indicate that the individual errors for temperature and concentration inversion for most cases show only small differences, i.e., the individual inverse errors closely follow the total error given by Eq. (3.1). An exception is the CO_2 4.3 μm band, for which the individual errors for temperature and concentration show very large differences, so only the individual inverse errors for this band are presented. Many error contours for temperature and concentration inversion were created. These results can be used as references to find optimal experimental parameters.

The relationship between transmissivities and temperature and concentration in Figs. 3.2 and 3.3 show that the transmissivity increases with decreasing temperature, while occupying a wider part of the spectrum, and decreases with increasing concentration, or more importantly, with pressure path length PxL. For the CO_2 4.3 μm band, the individual errors for concentration and temperature inversion are shown in Fig. 3.6 and Fig. 3.7, respectively. It indicates that for this band, the error for concentration inversion is much larger than temperature inversion for a wide range of conditions. With increasing temperature, the spectral band will become wider, making the spectrum more distinct at varying temperatures. That is why there is a smaller retrieving error for temperature inversion. But as pressure path length increases, first the transmissivity spectrum becomes saturated and large parts of the band reach zero transmissivity, making the spectrum no longer spectrally distinct. If pressure path lengths are further increased, the spectral band will also become wider. That is why the error for retrieving concentration becomes smaller for higher pressure path lengths.

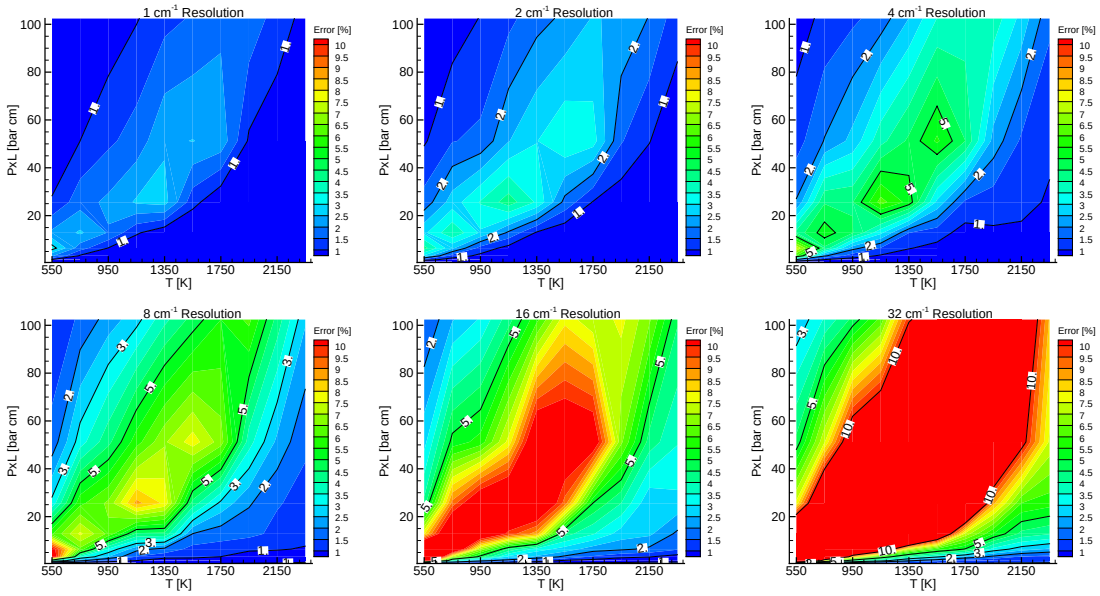

Figure 3.6: Error contours for concentration inversion when temperature and concentration are retrieved simultaneously, CO_2 4.3 μm band

Correspondingly, the conditions for temperature and concentration inversion within a required error limit can be determined from Figs. 3.6 and 3.7.

If the CO_2 2.7 μm band is employed at atmospheric pressure, as shown in Fig. 3.8, large errors are incurred at coarse resolution for small PxL. That is because this band is relatively weak for small pressure path length. If the pressure path length is not large enough, transmissivities will approach unity for this band and make the ill-posed radiation problem worse. For large PxL, as shown in Fig. 3.8, the results improve considerably for using the CO_2 2.7 μm band.

Optimal spectral band and resolution depend on conditions as well requirements. For example, consider a temperature of about 1350 K and CO_2 concentration of about 20%, and a pressure path length of PxL=1 bar $\times$ 20% $\times$ 100 cm=20 bar·cm. If the desired $Error$ for retrieving temperature and concentration is to be less than 5%, comparing all the frames in Figs. 3.6, 3.7 and 3.8, it is found that if the CO_2 2.7 μm band is used, all resolutions from 1 to 32 cm^{-1} can retrieve temperature and concentration accurately. However, the CO_2 4.3 μm band meets the requirements only for the finer 1 cm^{-1} or 2 cm^{-1} resolutions for concentration inversion. Thus, for this case, the CO_2 2.7 μm band and 32 cm^{-1} resolution are the optimal parameters, since they can meet the requirements and are the most efficient.

Generally, the H_2O 2.7 μm band performs good for large pressure path lengths at all the medium to coarse resolutions. Large errors are incurred only for very small PxL at coarse resolutions, as shown in Fig. 3.9. Considering an example for temperature of 2150 K, H_2O concentration of 10% and a pressure path length of PxL=1 bar $\times$ 10% $\times$ 100 cm=10 bar·cm. Again, if the desired

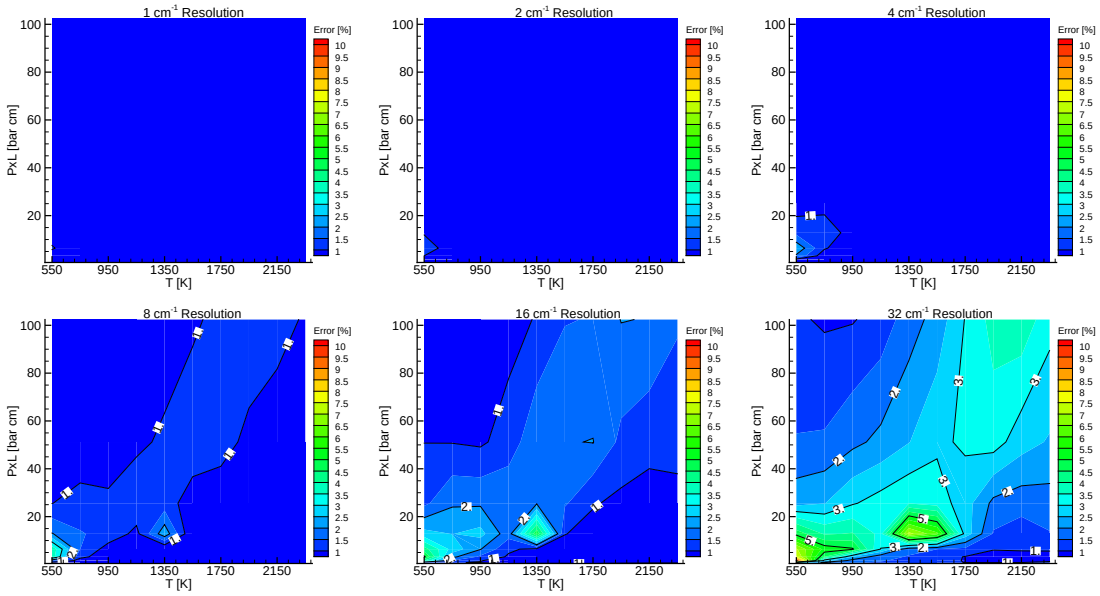

Figure 3.7: Error contours for temperature inversion when temperature and concentration are retrieved simultaneously , CO_2 4.3 μm band

Error for retrieving temperature and concentration is to be less than 5%, then all the resolutions can be used to retrieve temperature and H_2O. By contrast, if the H_2O 1.8 μm band is used at this condition, only finer resolutions of 1 and 2 cm^{-1} can meet the requirements for retrieving temperature and concentration. As shown in Fig. 3.10, for coarse resolutions from 8 and 32 cm^{-1}, the H_2O 1.8 μm band only performs well at very large *PxL*. Large errors for temperature and concentration inversions occur at higher temperature and lower pressure path length *PxL*, while the results get even worse at coarser resolution. Therefore, if the pressure path length *PxL* is not sufficiently large, using these two bands at lower resolution cannot retrieve temperature and concentration accurately. Finer resolution may be used if computational and measurement times are not considered a problem.

The CO 4.7 μm band shows similar performance to the H_2O 2.7 μm band. CO only has two bands in the infrared region, the CO 4.7 μm and 2.3 μm bands. The CO 4.7 μm band is a relatively strong band but not as strong as the CO_2 4.3 μm band; then using this band, one can retrieve temperature and species concentration accurately over a larger range of temperatures and pressure path lengths, as shown in Fig. 3.11. As indicated in Fig. 3.2(c), the CO 2.3 μm band may be too weak and holds little promise for temperature and concentration inversion. This can be proved by the results in Fig. 3.12. There are huge errors for retrieving temperature and concentration at all the studied temperatures and pressure path lengths using relatively coarse resolutions. For finer resolutions, temperatures and concentrations can only be accurately retrieved at very large pressure path lengths. For example, if we want the desired *Error* for retrieving temperature and concentration to be less than 5% for all the temperatures from 550 K to 2350 K, only the finer resolutions 1 and

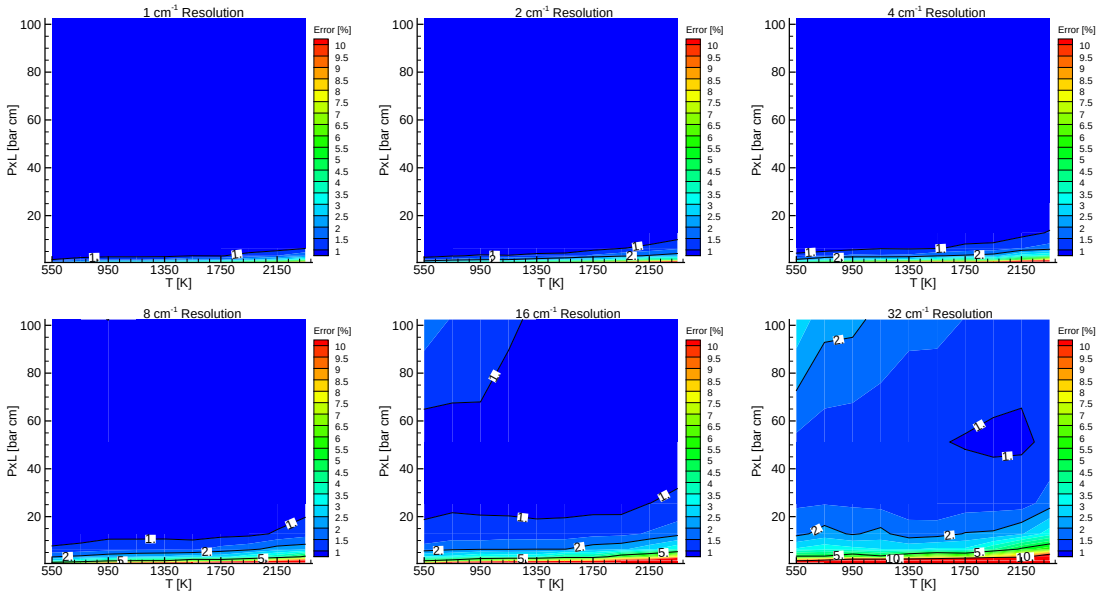

Figure 3.8: Error contours for temperature and concentration inversion, CO_2 2.7 μm band

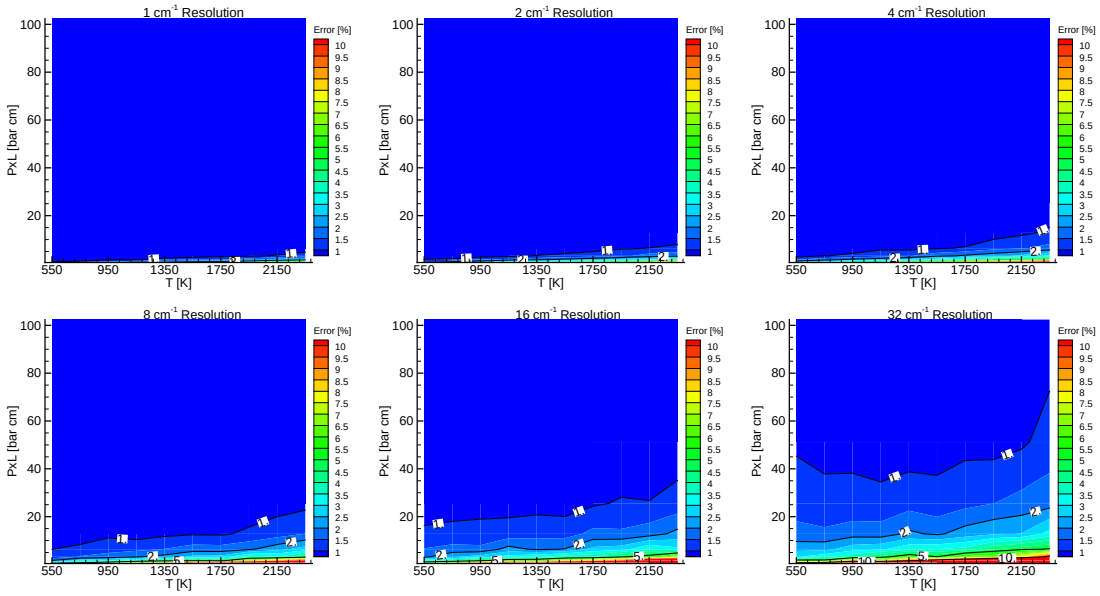

Figure 3.9: Error contours for temperature and concentration inversion, H_2O 2.7 μm band

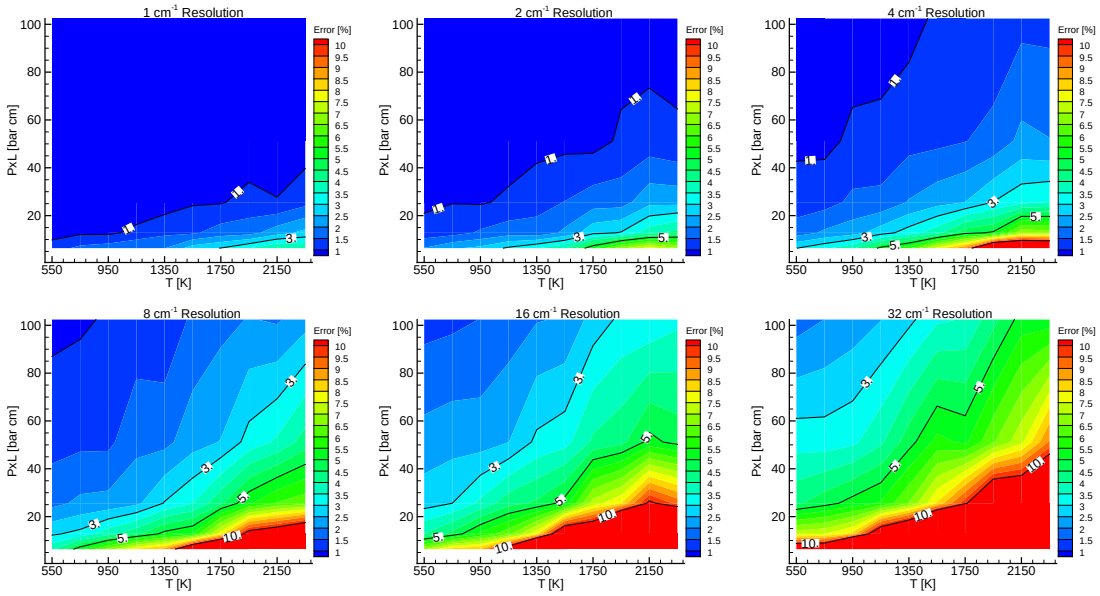

Figure 3.10: Error contours for temperature and concentration inversion, H_2O 1.8 μm band

2 cm^{-1} can be used and the pressure path lengths have to be larger than 20 bar·cm and 60 bar·cm, receptively.

3.5 Summary

The developed inverse radiation model is used to determine the optimal spectral band and resolution for temperature and concentration inversion in combustion systems. Synthetic transmissivities were created by convolving high-resolution transmissivity spectra with an ideal FTIR ILS function for three combustion species, several different spectral bands and different FTIR spectral resolutions for 10 different temperatures from 550 K to 2350 K and 5 different gas concentrations from 2% to 32% for varying pressure path length. These synthetic spectra were disturbed with Gaussian random noise and artificial measurement drift to systematically study the performance of inverse calculations. Experimental parameters (wavenumber range and resolution) that can minimize the ill-posedness of inversion were determined.

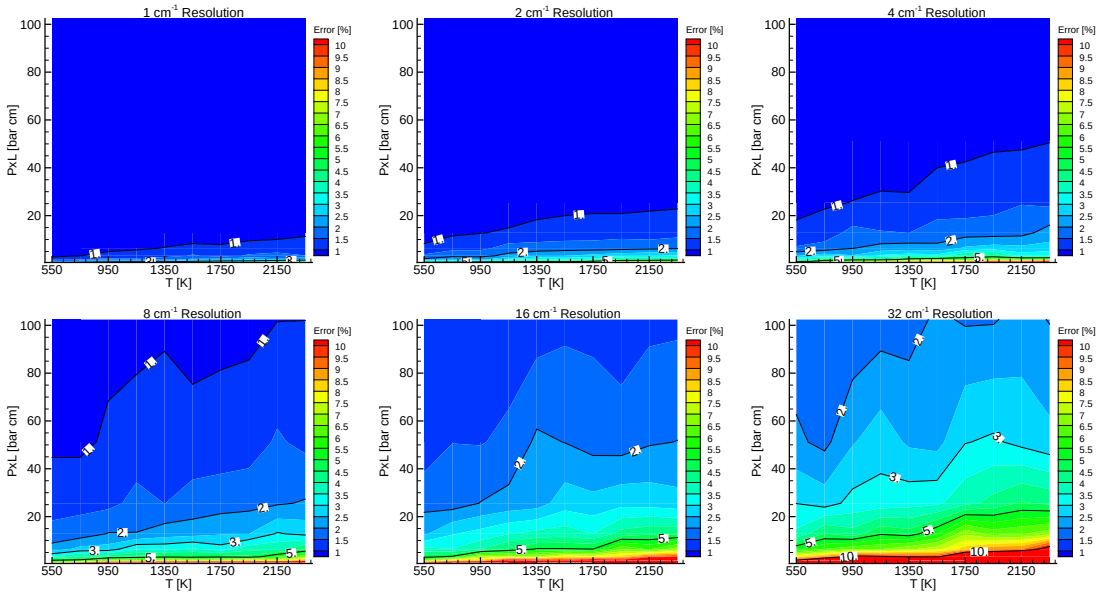

Figure 3.11: Error contours for temperature and concentration inversion, CO 4.7 μm band

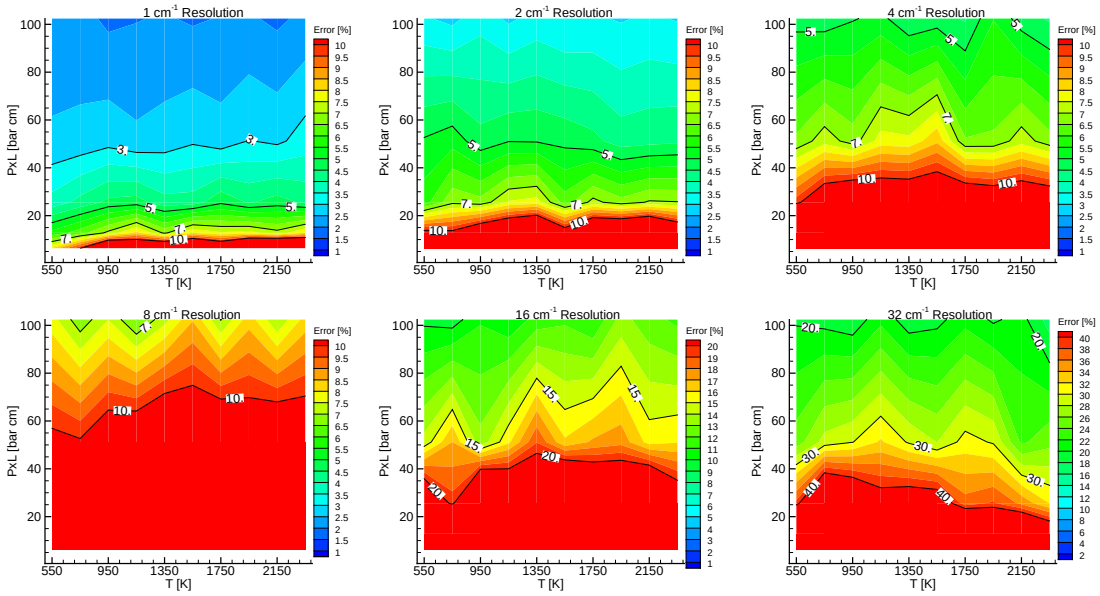

Figure 3.12: Error contours for temperature and concentration inversion, CO 2.3 μm band

Chapter 4

Inverse Radiation Model for Nonhomogeneous Media

4.1 Introduction

In this chapter, we present an inverse calculation model based on the Levenberg-Marquardt optimization method with Tikhonov Regularization to reconstruct CO_2 temperature profiles and average concentrations from measured line-of-sight spectral intensity data. The measured spectra were synthesized through calculations from HITEMP 2010, the high-temperature spectral database, for the CO_2 4.3 μm and CO_2 2.7 μm bands. Although it has been shown Tikhonov regularization is suitable for ill-posed inverse problems, it is difficult to select an appropriate regularization parameter, especially for nonlinear problems. Due to the ill-posedness of the inverse problem, additional conditions or criteria need to be imposed to determine the most realistic solution. Most regularization methods transform an ill-posed inverse problem into a well-behaved one by adding auxiliary information based on desired or assumed characteristics. Tikhonov regularization imposes smoothness to the solution by adding a regularization term and the extent of regularization is controlled by a regularization parameter. In the present study, a new regularization selection method is proposed and performs very well for different temperature profiles inversion.

4.2 Forward calculation

Figure.1.1 shows a schematic diagram of the physical system. A non-isothermal combustion gaseous column is presented. It is assumed the system is in local thermal equilibrium and scattering effects in the medium can be neglected. The spectral intensity along a line-of-sight within a nonscattering medium, as seen by a detector at $s = L$ is given by [38]

$$I_\eta = I_{0\eta} e^{-\int_0^L \kappa_\eta ds} + \int_0^L \kappa_\eta I_{b\eta} e^{-\int_s^L \kappa_\eta ds'} ds \tag{4.1}$$

where κ_η is the spectral absorption coefficient at wavenumber η (which depends on temperature and concentration), $I_{b\eta}$ is the local blackbody intensity of the medium and $I_{0\eta}$ is external irradiation entering the gas column $0 \leq s \leq L$ at $s = 0$. In this study, we assume there is no external irradiation and only emission from the gaseous medium is taken into account.

In order to determine the intensity given by Eq. (4.1) numerically, the entire gas column is divided into n coarse sub-columns for each of which temperature is assumed constant. Without external irradiation, Eq. (4.1) can then be discretized as

$$I_\eta = \sum_{i=1}^{n-1} I_{bi}\left(1 - e^{-\Delta s_i \kappa_{\eta i}}\right) e^{-\sum_{k=i+1}^{n} \Delta s_k \kappa_{\eta j}} + I_{bn}\left(1 - e^{-\Delta s_n \kappa_{\eta n}}\right) = f(\mathbf{T}) \tag{4.2}$$

where

$$\mathbf{T} = [T_i]; \qquad i = 1, ..., n \tag{4.3}$$

and f is a nonlinear function of the temperatures of all sub-columns. $\kappa_{\eta i}$ is the absorption coefficient calculated from the HITEMP 2010 line-by-line database [33] for the temperature of the i-th sub-column. Eq. (4.2) shows the relationship between the outgoing intensity and the temperature distribution along a line-of-sight.

Since intensity spectra can only be measured at a finite resolution, LBL spectral intensities of Eq. (4.2) are convolved with an ideal instrument line shape (ILS) function to mimic the different spectral resolutions of a spectrometer. Here we use triangular apodization for creating the ideal ILS $\Gamma(\eta)$, and the ILS function we used is the same as in Eq. 2.7. In this study, LBL spectral intensities are convolved with an ILS function with nominal resolution of 8 cm^{-1} to create medium-resolution intensity spectra.

After intensity spectra are convolved with the ILF $\Gamma(\eta)$, they become,

$$I_{\eta c} = \int_0^\infty I(\eta')\Gamma(\eta - \eta')d\eta' \tag{4.4}$$

If one measures intensity with a certain spectral resolution, obtaining m discrete values of wavenumber ($m > n$), a system of nonlinear equation results,

$$\mathbf{I}_c = \mathbf{f}(\mathbf{T}) \tag{4.5}$$

where

$$\begin{aligned} &\mathbf{I}_c = \left[I_j\right]; \\ &\mathbf{f} = \left[f_j([T_i])\right]; \qquad i = 1, ..., n \text{ and } j = 1, ..., m \end{aligned} \tag{4.6}$$

4.3 Inverse calculation

Equation (4.5) cannot be inverted directly to obtain the temperature profile of the gas column. An inverse procedure is required to solve this equation numerically. In this study, the solution to the

inverse problem is found by minimizing an objective function, F_1, [38]

$$F_1(\mathbf{T}) = \sum_{i=1}^{I} (I_i - Y_i)^2 = \| (\mathbf{i} - \mathbf{y}) \|^2 \tag{4.7}$$

where I_i is the predicted intensity spectrum from forward calculations, and Y_i is the measured intensity spectrum.

In order to determine the most realistic inverse solution, this ill-posed problem needs to be transformed into a well-behaved one by adding auxiliary information based on desired or assumed characteristics. For this problem, Tikhonov regularization is employed to impose smoothness to the solution by adding a regularization term $\lambda\, \mathbf{T}^{\mathrm{T}} \cdot \mathbf{R} \cdot \mathbf{T}$ to Eq. (4.7),

$$F_2(\mathbf{T}) = \| (\mathbf{i} - \mathbf{y}) \|^2 + \lambda\, \mathbf{T}^{\mathrm{T}} \cdot \mathbf{R} \cdot \mathbf{T} \tag{4.8}$$

where

$$\mathbf{T}^{\mathrm{T}} \cdot \mathbf{R} \cdot \mathbf{T} = \sum_{i=1}^{n-2} (T_i - 2T_{i+1} + T_{i+2})^2 \tag{4.9}$$

and here $\mathbf{R}$ is a second order smoothing matrix, which can be found by calculating the second derivatives of Eq. (4.9) versus temperature for each sub-column. The reader is referred to *Numerical Recipes* [78] for more details about how to obtain a smoothing matrix. The regularization parameter λ determines the smoothness of the solution: a small value of λ implies little regularization, while a larger λ imposes more presumed information to the solution. A good selection of regularization parameter is critical to obtain a good inverse solution. In the present study, a new method for selecting an optimal λ for this nonlinear problem is proposed.

To solve this problem numerically, the parameter vector $\mathbf{T}$ is gradually increased by a small value $\delta\mathbf{T}$ at each iteration,

$$\mathbf{T}_{new} = \mathbf{T}_{old} + \delta\mathbf{T} \tag{4.10}$$

with

$$\delta\mathbf{T} = -(\mathbf{H} + \mu\, \mathbf{\Omega} + \lambda\, \mathbf{R})^{-1}\ \mathbf{B} \tag{4.11}$$

In the Levenberg-Marquardt method, The vector $\mathbf{B} = \nabla F_1(\mathbf{T})$ is the gradient vector of F_1 with respect to $\mathbf{T}$, and $\mathbf{H}$ is the Hessian matrix $\mathbf{H} = \nabla^2 F_1(\mathbf{T})$. $\mathbf{\Omega}$ is a unit matrix with diagonal elements equal to 1. The same Levenberg-Marquardt algorithm as in Chapter 2 was applied here to retrieve temperature profiles. The parameter vector became the set of discrete temperature $\mathbf{T}$.

4.4 Selecting the Regularization Parameter

It is intuitively known from Eq.(4.8) that a large regularization parameter λ makes the temperature profile overregularized and a small regularization parameter λ makes the temperature profile underregularized. It is difficulty to select a good regularization parameter for a nonlinear problem like Eq.(4.8). In this section a new method is proposed to select an appropriate regularization parameter λ. This method is based on the theory of the L-curve criterion [126] and the discrepancy

principle [127]. Several types of temperature profiles are retrieved accurately using this method.

The L-curve is a log-log plot of the regularization term $\gamma_\lambda = \mathbf{T}^{\mathrm{T}} \cdot \mathbf{R} \cdot \mathbf{T}$ vs. the residual term $\rho_\lambda = \|(\mathbf{i} - \mathbf{y})\|^2$. A good regularization parameter and well-regularized inverse solution can be found by locating the corner on the L-curve. For a linear problem, the process is pretty straightforward. First the problem is solved for a wide range of regularization parameters to obtain the L-curve and then the corner is located. But for a nonlinear problem, the two terms on the right hand side (RHS) of Eq. (4.8) require the solution to a nonlinear problem, making it is very difficult and time consuming to compute the "exact" L-curve. Based on the fact that all calculated points always lie on or above the exact L-curve, Viklands and Gulliksson [128] suggested to gather points given during iteration and pick a subset from all gathered points to define a monotonically decreasing convex function. This function can be treated as an approximated L-curve. Since it still requires a considerably large number of points to create a relatively smooth and meaningful approximate L-curve, this parameter selection method is still not practical for solving nonlinear inverse problems. The discrepancy principle is based on the reasoning that the residual term should be at least the same order of magnitude as the noise. This suggests to choose the regularization parameter so that the residual error $\|(\mathbf{i}(\mathbf{T}_\lambda) - \mathbf{y})\|$ of the regularized system is less than or equal to ϵ. This implies λ should be chosen so that

$$\|(\mathbf{i}(\mathbf{T}_\lambda) - \mathbf{y})\|^2 = \epsilon^2 \tag{4.12}$$

where $\mathbf{T}_\lambda$ is the regularized solution corresponding to the regularization parameter λ. This also requires to solve the nonlinear Eq. (4.12) many times and both the L-curve criterion and the discrepancy principle will choose a fixed λ as regularization parameter. However, as stated in the previous section, Eq. (4.8) is solved by iteration and iteration with a fixed λ makes it converge slowly. Kim and Song [86] suggested using a fast and efficient model to choose different values λ for each iteration, i.e.,

$$\lambda = \frac{\|(\mathbf{i} - \mathbf{y})\|^2}{\mathbf{T}^{\mathrm{T}} \cdot \mathbf{R} \cdot \mathbf{T}} \frac{1}{G} \tag{4.13}$$

where G is a correction factor which counterbalances the weight between the residual term and regularization term. This biases the solution toward the true profile without sacrificing the smoothness of the profile and thus makes the solution converge faster. Kim and Song [86] employed an empirical value, which is based on their own practical experience through numerical experiments. A "magic" number $G = 5$ is claimed to be appropriate for many problems. According to our extensive numerical experiments, the optimal G is quite different for different temperature profiles and also relies on the initial guess of the temperature distribution. A "magic" number $G = 5$ cannot always guarantee a good inverse solution.

In the present study, Eq. (4.13) is used to determine the regularization parameter at each iteration, but the correction number G is selected based on the combination of the L-curve criterion and the discrepancy principle. An appropriate correction number can be found by solving the nonlinear Eq. (4.8) only a few times. Assuming the noise of the measured transmissivities can be estimated and employing the discrepancy principle, the residual error $\rho_\lambda = \|(\mathbf{i} - \mathbf{y})\|^2$ of the regularized system should be less than or equal to the measurement noise ϵ^2. For a given correction number G, Eq. (4.8) is solved by iteration, which is stopped when $\rho_\lambda \leq \epsilon^2$. For different correction numbers G, the regularized solution has different values for $\gamma_\lambda = \mathbf{T}^{\mathrm{T}} \cdot \mathbf{R} \cdot \mathbf{T}$. Based on the fact that all

calculated points $(\gamma_\lambda, \rho_\lambda)$ always lie on or above the exact L-curve, the one which is closest to the "exact" L-curve will have the best inverse solution. Usually the "exact" L-curve is not known, so the one satisfies $\rho_\lambda \leq \epsilon^2$ and with the smallest γ_λ will have the best inverse solution. This process can be summarized as: for a given correction number G, solve Eq. (4.8) by iteration; stop iteration if $\rho_\lambda \leq \epsilon^2$ or the number of iterations exceeds a given maximum iteration number (400); choose the one which satisfies $\rho_\lambda \leq \epsilon^2$ and has the smallest γ_λ as the best inverse solution.

4.5 Results and Discussions

4.5.1 Temperature profiles reconstruction

In this section, two fictitious temperature profiles are retrieved based on the Levenberg-Marquardt optimization method with Tikhonov Regularization. The proposed regularization parameter selection scheme is employed. Because there is no experimental data available, synthetic intensity spectra for the CO_2 4.3 μm band (2000 cm^{-1}–2500 cm^{-1}) are created from the HITEMP 2010 database for a 10 cm-long gas column with a uniform CO_2 concentration of 20%. The gas column is divided into 21 sub-columns and each temperature is assumed uniform. Medium-resolution (8 cm^{-1}) spectral data are created with 260 data points for the spectral range 2000 cm^{-1}–2500 cm^{-1}. Gaussian random noise was added to the intensity spectra to simulate the random error inevitable in experiments: first a small relative error (0.5%) is added to the synthetic spectra to investigate the performance of the inverse model, and then more realistic relative error (3%) is used.

The first tested temperature profile has one peak and is symmetric, as shown in Fig. 4.1 (a). In order to select an appropriate correction number in Eq. (4.13) to retrieve the temperature distribution, several correction number values from 0.1-1000 were tested. As demonstrated in Fig. 4.1 (c), if the correction number is too small (G=0.1), the solution is overregularized and the residual term $\rho_\lambda = \|(\mathbf{i} - \mathbf{y})\|^2$ may never converge to the noise level and stop before $\rho_\lambda \leq \epsilon^2$. If the correction number is too large (G=1000), the temperature profile is underregularized and will have a large value for the regularization term $\gamma_\lambda = \mathbf{T}^{\mathrm{T}} \cdot \mathbf{R} \cdot \mathbf{T}$ when $\rho_\lambda \leq \epsilon^2$. Retrieved temperatures and spectral intensities using correction number values $G = 0.1$ and $G = 100$ are also shown in Fig. 4.1 (a) and (b). For the five tested correction numbers, solving Eq. (4.8) using $G = 1$ produced the smallest γ_λ and according to the proposed parameter selection scheme, $G = 1$ is chosen as the optimal correction number for the given problem. As shown in Fig. 4.1 (a), the inverse solution agrees very well with the exact temperature profile.

The second temperature profile has two symmetric peaks, as shown in Fig. 4.2 (a). Retrieved temperatures and spectral intensities using correction number values $G = 0.1$, $G = 1$ and $G = 100$ are shown in Fig. 4.2 (a) and (b). The proposed correction number selection scheme is employed and again G=1 is found to be the optimal correction number for this problem, as shown in Fig. 4.2 (c). In this case, the retrieved optimal temperature profile does not match with the exact one very well: discrepancies are observed at locations between the two peaks. Extensive numerical experiments indicate that obtaining a best inverse solution not only relies on an appropriate correction number, but an appropriate initial guess for the temperature profile is also important. For this problem, the temperature distribution labeled "Initial guess 1" in Fig. 4.3 was used as the initial guess of the temperature profile. If a sine-shape temperature distribution is used with the same number of peaks

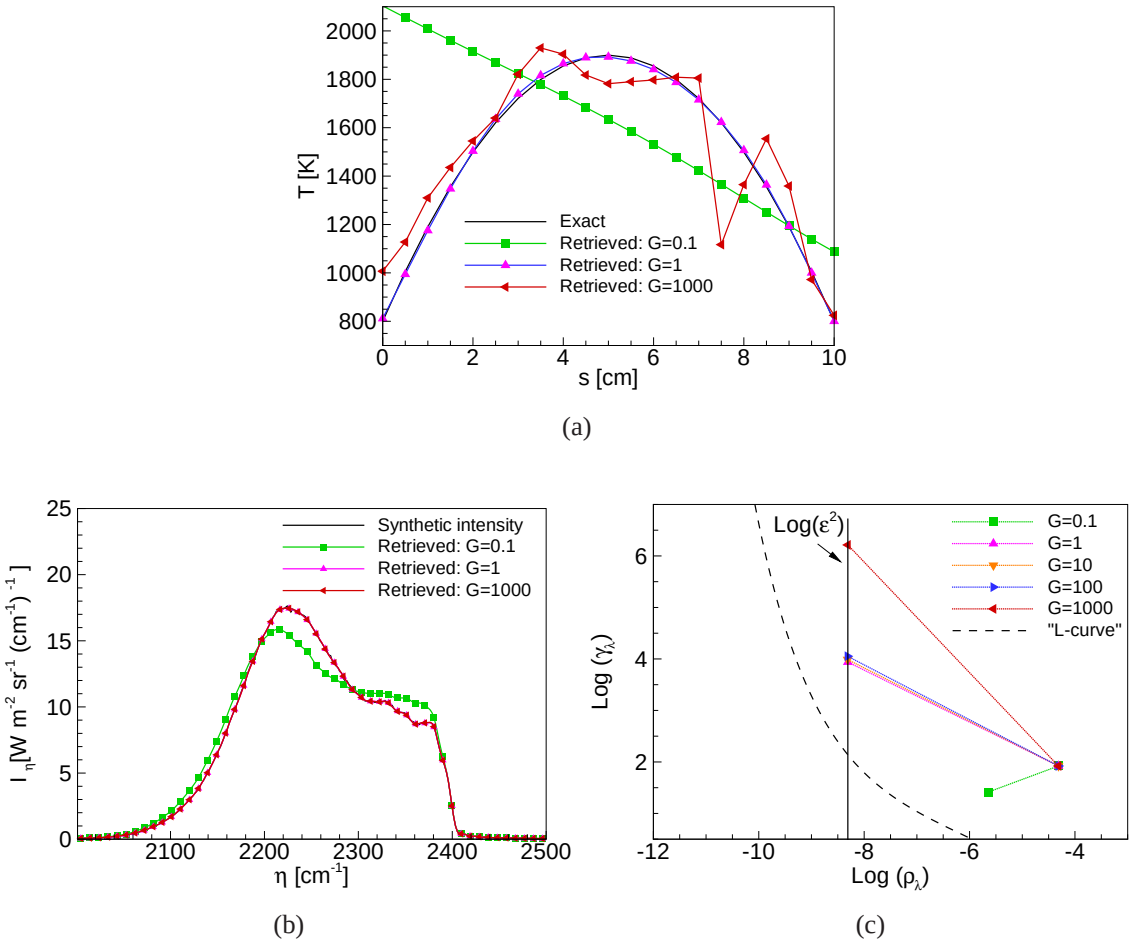

Figure 4.1: (a): Comparison of retrieved temperature and exact temperature for a one-peak temperature profile using correction numbers $G = 0.1$, $G = 1$ and $G = 1000$. (b): Comparison of retrieved intensity spectra with synthetic intensity spectrum for correction numbers $G = 0.1$, $G = 1$ and $G = 1000$. (c): Illustration of using the L-curve criterion and the discrepancy principle to determine the optimal correction number G, here $G = 1$ is selected for the given problem.

and valleys as the exact one, such as “Initial guess 2” shown in Fig. 4.3, the retrieved temperature improves significantly and matches perfectly with the exact one as shown in Fig. 4.4 (a). The optimal correction number is found to be G=0.01 for this case, as shown in Fig. 4.4 (c). This implies that the optimal correction number also depends on the initial guess of the temperature distribution. In order to get a unique solution for this kind of ill-posed problem, one must necessarily introduce some additional assumptions. For retrieving a best inverse solution, what really matters is not the exact value of the optimal correction number G but the magnitude of the correction number. As shown in Figs. 4.1 (c), 4.2 (c) and 4.4 (c), there is a range of correction numbers, which produce similar results. Using these values as the correction number can also produce acceptable results.

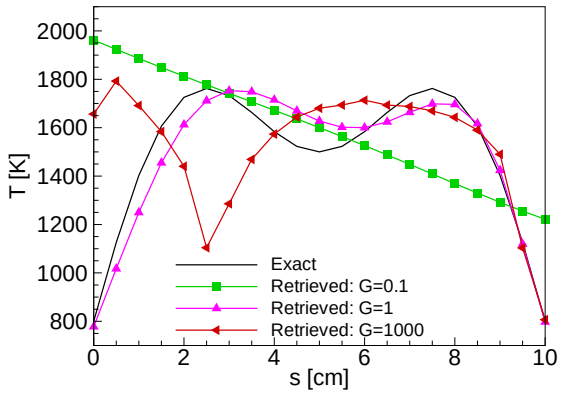

(a)

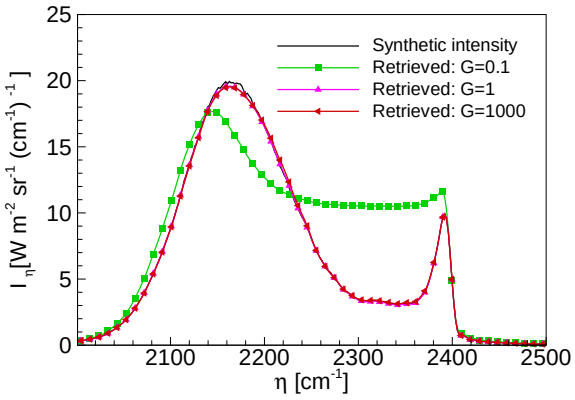

(b)

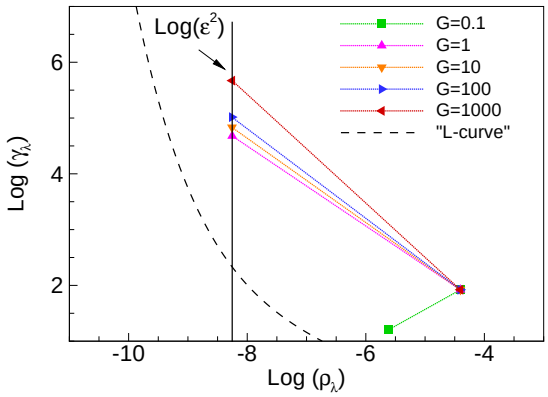

(c)

Figure 4.2: (a): Comparison of retrieved temperature and exact temperature for a two-peaks temperature profile using correction numbers $G = 0.1$, $G = 1$ and $G = 1000$. (b): Comparison of retrieved intensity spectra with synthetic intensity spectrum for correction numbers $G = 0.1$, $G = 1$ and $G = 1000$. (c): Illustration of using the L-curve criterion and the discrepancy principle to determine the optimal correction number G, here $G = 1$ is selected for the given problem.

One important characteristic of ill-posed problems is that the solution is very sensitive to noise: without enough additional information for the system, small noise may alter the solution significantly. The above two temperature profiles were retrieved from synthetic spectral intensity with small random noise (0.5%). Even for this small noise, the retrieved temperature can have large discrepancies from the exact one if a bad initial guess is used, as indicated by the case in Fig. 4.2 (a). It is not a surprise that worse temperature profiles will be retrieved if there is more noise in the intensity spectra. Figure 4.5 (a) shows two retrieved temperature profiles from a synthetic spectral intensity spectrum with 3% of Gaussian random noise for the two-peak temperature profile. “Retrieved 1” and “Retrieved 2” are retrieved temperature profiles using “Initial guess 1” and “Initial

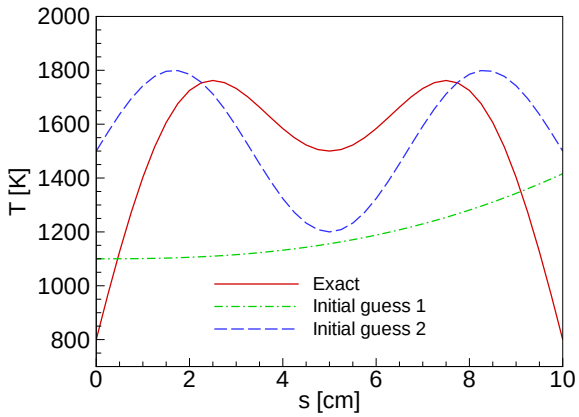

Figure 4.3: Comparison of two initial guesses of the temperature profile for the second tested cases.

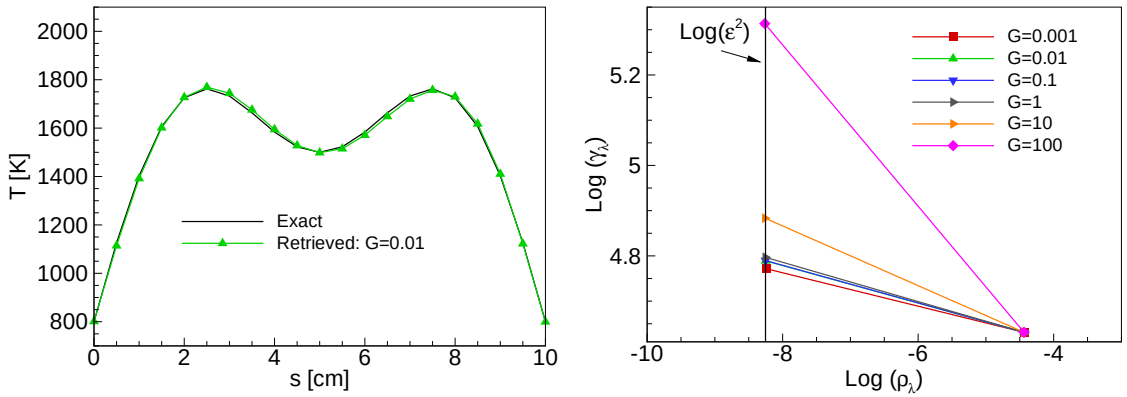

(a) (b)

Figure 4.4: (a): Comparison of retrieved temperature and exact temperature for a two-peak temperature profile using correction number $G = 0.01$. (b): Illustration of using the L-curve criterion and the discrepancy principle to determine the appropriate correction number G, here $G = 0.01$ is selected for the given problem.

guess 2" as the initial guesses in Fig. 4.3, respectively. As shown in this figure, the retrieved temperature profiles differ significantly from the exact one, especially for small s, no matter which initial guess is used (i.e., locations farther away from the detector).

All these cases so far are based on one-sided measured data taken by a detector at $s = L$ as shown in Fig. 1.1. Accuracy improves considerably if optical access is available for two-sided measurements (exiting intensity to the right at $s = L$, and also to the left at $s = 0$). This is demonstrated in Fig. 4.5 (b), which shows two retrieved temperature profiles from a synthetic spectral intensity

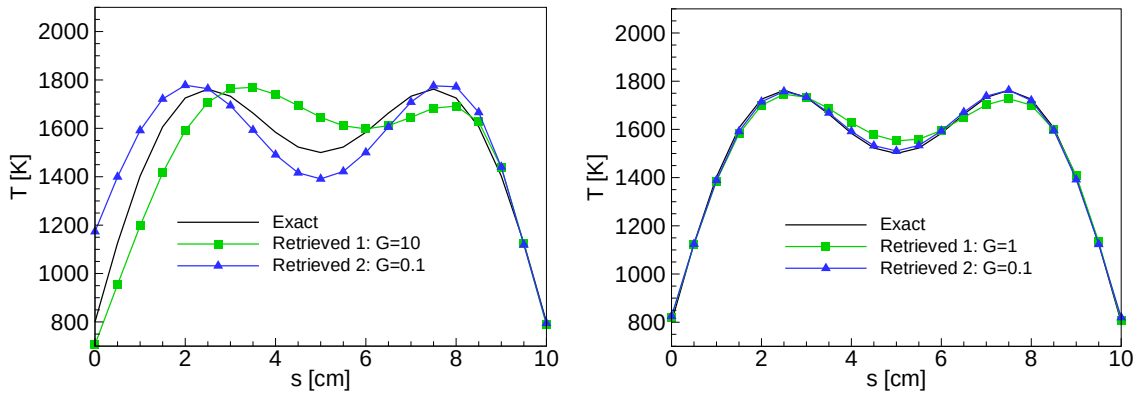

(a) (b)

Figure 4.5: Comparison of retrieved temperature and exact temperature for a two-peak temperature profile using two different initial guesses from spectral intensity spectrum with 3% random noise. (a): Temperature is retrieved from one-side measured spectral data. (b): Temperature is retrieved from two-side measured spectral data.

spectrum with 3% Gaussian random noise for the two-peak temperature profile, as retrieved from two-sided spectral intensity measurements. As shown in the figure, the result improves significantly for both initial guesses. Another advantage of using two-sided measured data is that the inverse calculation is more efficient than using one-sided measured data: because additional information from both sides of the gas column is provided to the inverse calculation model, the solution converges faster than using one-sided measured data.

4.5.2 Comparison of the CO_2 4.3 μm and 2.7 μm bands

All the test cases in the previous section use the CO_2 4.3 μm intensity band to retrieve temperature profiles for a 10 cm-long gas column with 20% of CO_2 by volume, i.e., for a pressure path length (defined as the product of the partial pressure and gas path length) of PxL=1 bar $\times$ 20% $\times$ 10 cm=2 bar·cm. In this section, the performance of the CO_2 4.3 μm and 2.7 μm bands for retrieving temperature profiles are investigated for three different pressure path lengths. Synthetic intensity spectra from the CO_2 4.3 μm band (2000 cm^{-1}–2500 cm^{-1}) and the CO_2 2.7 μm band (3200 cm^{-1}–3800 cm^{-1}) are created from the HITEMP 2010 database for a 10 cm, a 100 cm and a 1000 cm long gas column (all for a fixed CO_2 concentration of 20%). The three gas columns are each divided into 21 sub-columns and each temperature is assumed uniform. Again, 0.5% Gaussian random noise was added to the intensity spectra.

Figure 4.6 shows retrieved temperatures from the CO_2 4.3 μm and 2.7 μm spectral bands compared against the true temperatures for the three gas columns with different gas path lengths. It is seen that, for a wide range of gas path lengths, using the CO_2 4.3 μm band can retrieve temperature profiles relatively accurately. The 2.7 μm band only performs better when the gas path length

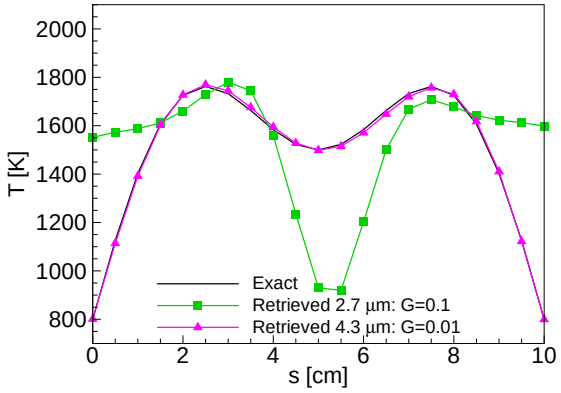

(a)

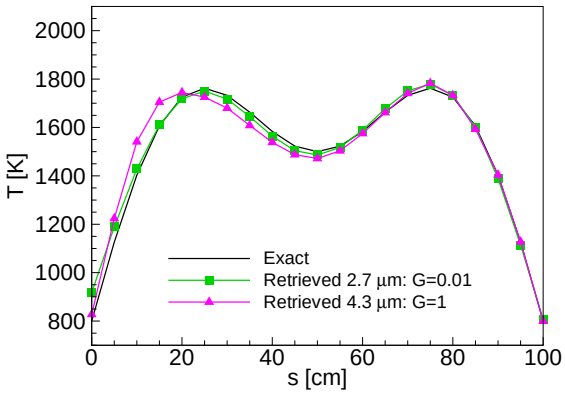

(b)

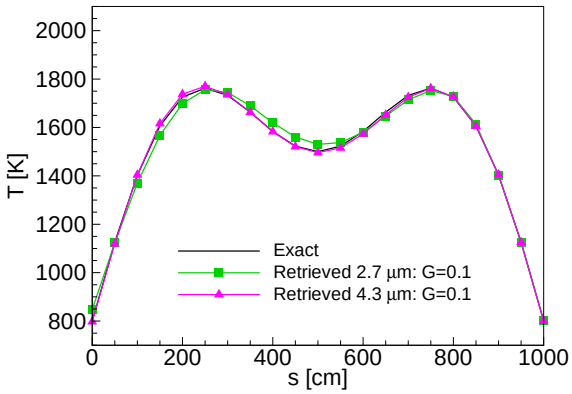

(c)

Figure 4.6: Comparison of retrieved temperature and exact temperature from the CO_2 4.3 μm and 2.7 μm spectral bands. (a): 10 cm-long gas column. (b): 100 cm-long gas column. (c): 1000 cm-long gas column.

gets sufficiently large. For an ideal spectral band used for inverse calculations, within the band every portion of the gas column should make a contribution to the detected intensities, and all the contributions should be spectrally distinguishable. In order to explain the different performances in Fig. 4.6, it is important to understand what are the intensity contributions from different portions of the gas column. Figures 4.7, 4.8 and 4.9 show the "detected" spectral intensity, which are contributed by the 1st, 6th, 11th, 16th and 21st sub-columns (one extra column 20 is also included in order to show the dynamics in the intensity contributions; red lines for column 1 are not seen because its emission is almost completely absorbed by the gas along the path) of the CO_2 4.3 μm and 2.7 μm bands for the 10 cm-long, 100 cm-long and 1000 cm-long gas columns, respectively. For the CO_2 4.3 μm band, different portions of the gas column have spectrally distinguishable contributions to the spectral intensity for all gas path lengths from 10 cm to 1000 cm, as indicated

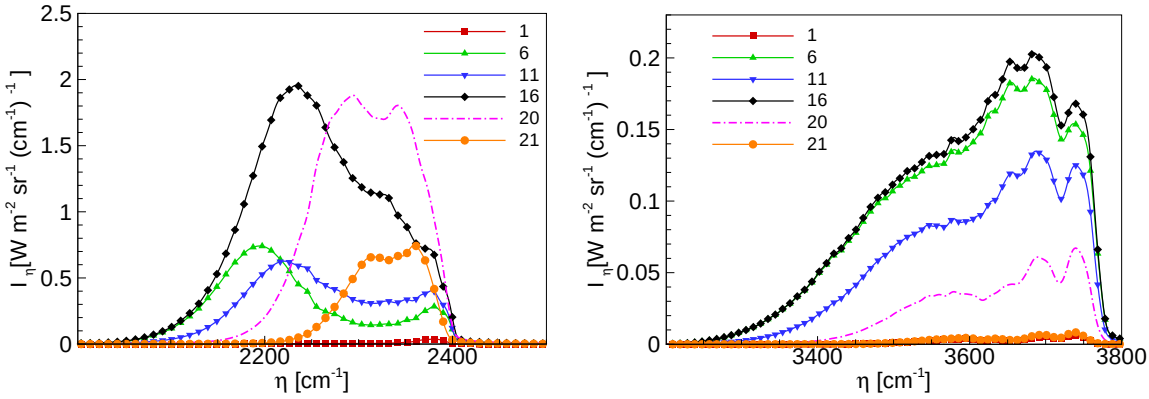

(a) (b)

Figure 4.7: Spectral intensity contribution from 6 sub-columns for a 10 cm-long gas column, the true temperature profile is shown in Fig. 4.6 (a). (a): the CO_2 4.3 μm band. (b): the CO_2 2.7 μm band.

in Figs. 4.7 (a), 4.8 (a) and 4.9 (a). For the CO_2 2.7 μm band, as shown in Fig. 4.7 (b), the spectral intensities from different portions of the gas column have similar patterns for the 10 cm long gas column. Increasing the gas path length to 1000 cm, as shown in Figs 4.8 (b) and 4.9 (b), the intensity from different portions of the gas column become spectrally different. This explains why the 2.7 μm band performs well only at large pressure path lengths. Since the CO_2 4.3 μm band shows equal or better performance for all inverse radiation calculations, this band may always be used for temperature and concentration inversion.

4.5.3 Temperature profile and average concentration reconstruction

Unfortunately, only the temperature profile can be retrieved from the emitted intensity. This can be shown by assuming temperature T to be constant, and concentration to be a function of location s, $x = x(s)$: for such case the emitted intensity is

$$I_\eta = \int_0^L I_{b\eta}(T)\kappa_\eta(T,x)e^{-\int_s^L \kappa_\eta(T,x)ds'}ds \tag{4.14}$$

For species like CO_2, absorption coefficient κ_η is almost linear with concentration x due to weak self-broadening effects of CO_2, i.e.,

$$\kappa_\eta(T,x) = \kappa_{P\eta}(T)x \tag{4.15}$$

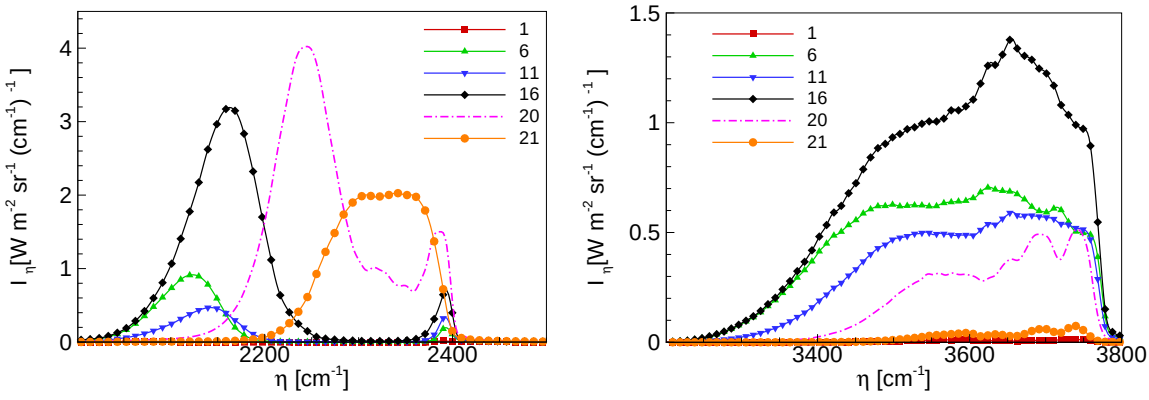

(a) (b)

Figure 4.8: Spectral intensity contribution from 6 sub-columns for a 100 cm-long gas column, the true temperature profile is shown in Fig. 4.6 (b). (a): the CO_2 4.3 μm band. (b): the CO_2 2.7 μm band.

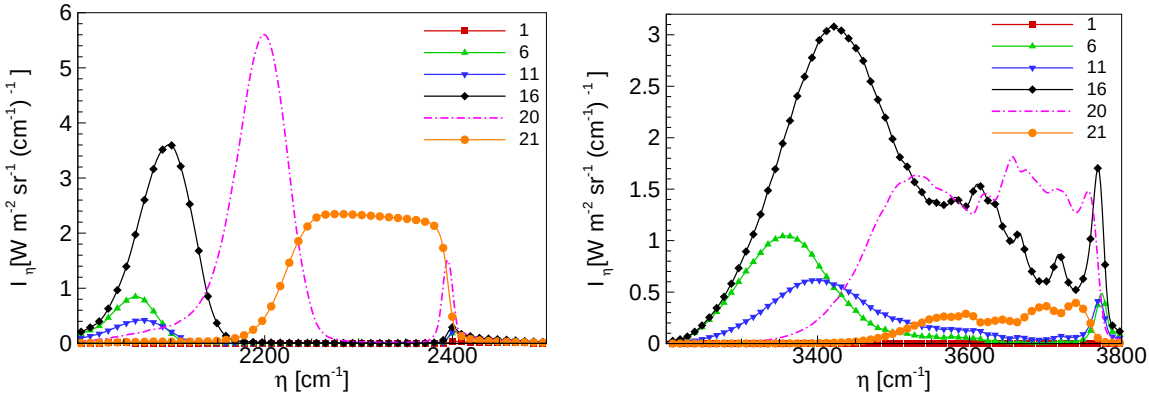

(a) (b)

Figure 4.9: Spectral intensity contribution from 6 sub-columns for a 1000 cm-long gas column, the true temperature profile is shown in Fig. 4.6 (c). (a): the CO_2 4.3 μm band. (b): the CO_2 2.7 μm band.

Where $\kappa_{P\eta}$ is the pressured-based absorption coefficient and is a function of temperature only. Rewriting Eq. (4.14) gives

$$\begin{aligned} I_\eta &= I_{b\eta}(T)\kappa_{P\eta}(T)\int_0^L x(s)e^{-\kappa_{P\eta}(T)\int_s^L x(s')ds'}ds \\ &= -I_{b\eta}(T)\kappa_{P\eta}(T)\int_0^L e^{-\kappa_{P\eta}(T)\int_s^L x(s')ds'}d\left(\int_s^L x(s')ds'\right) \\ &= I_{b\eta}(T)\left[1-e^{-\kappa_{P\eta}(T)\int_0^L x(s)ds}\right] \end{aligned} \tag{4.16}$$

where $\int_0^L x(s)ds$ is the area under the curve $x(s)$ for s from 0 to L. As long as this area remain the same, the emitted intensity will be the same and, for a given intensity spectrum, the retrieved concentration profile will have infinitely many solutions; thus, it is impossible to reconstruct the concentration profile based on the emitted intensity spectrum alone. Only average concentration can be retrieved. Therefore, in the previous section it was assumed that concentration is known and constant (20%) along the path, and only temperature profiles are retrieved. In this section, the model is extended to include average concentration as another inverse parameter: temperature profile plus average concentration can be retrieved simultaneously. Temperature profiles are retrieved in the same fashion as discussed before using the same regularization method. There is no regularizations applied between temperatures and average concentration. Figure. 4.10 shows the comparison of exact temperature profile and exact average concentration with retrieved temperature profile and retrieved average concentration from the CO_2 4.3 μm band. They both match very well.

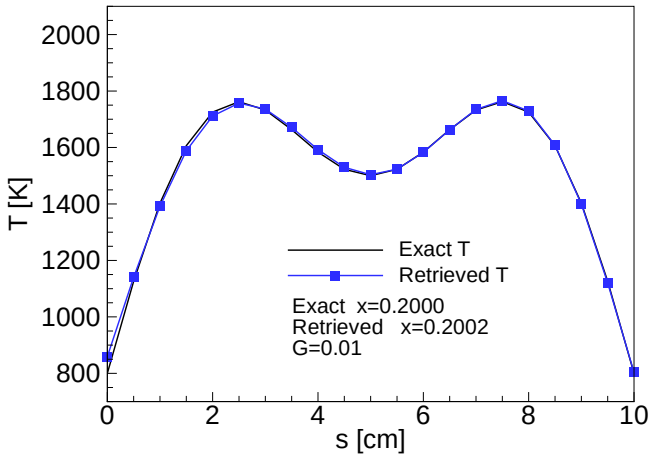

Figure 4.10: Inverse results for retrieving temperature profile plus average concentration.

4.6 Summary

An inverse radiation model was developed by applying the Levenberg-Marquardt inverse scheme with Tikhonov regularization to a nonhomogeneous gas medium. This model is capable of retrieving the temperature profile plus average concentration based on the emitted intensity spectra from the hot gas medium. A new selection method is proposed to determine the optimal regularization parameter for Tikhonov regularization. This new method is tested using synthetic intensity data, which were created based on the HITEMP 2010 database for the CO_2 4.3 μm band for two fictitious temperature profiles and disturbed with Gaussian random noise. This new regularization parameter selection method shows good generality for different temperature profile inversions.

Chapter 5

Inverse Radiation Model for Turbulent Systems

5.1 Introduction

In the present study, by assuming the pdf shape of temperature and species concentration fluctuations, time-averaged transmissivity and its rms spectrum are successfully related to the time-averaged and rms values of temperature and species concentration; this is the so-called forward calculation. Once these relationships are established, time-averaged and rms values of temperature and species concentration and turbulence scales can be retrieved from time-averaged transmissivity and its rms spectrum; this is the so-called inverse calculation. The absorption coefficients, which are required to calculate transmissivity and its rms spectrum, are calculated from HITEMP 2010. For the present work, synthetic turbulent fields for temperature and species concentration fluctuations are generated by a stochastic approach. Instantaneous transmissivity spectra are generated along a line-of-sight for different spectral bands of CO_2, H_2O and CO. Synthetic time-averaged transmissivities and their rms spectra are calculated by conducting a stochastic analysis on these instantaneous transmissivity spectra and are used as input data to retrieve time-averaged and rms values of temperature, species concentration and turbulence length scale.

5.2 Instantaneous turbulence fields

A stochastic approach developed by Kritzstein and Soufiani [129] is adopted here, in which instantaneous temperature and species concentration fields are generated by Fourier transforming an assumed space-time correlation function. Without specifying the entire geometry of the system, turbulent scalar fields are created along a line-of-sight over a gas column of length L and for the time interval $0 \leqslant t \leqslant t_0$. The scalar fields are assumed to be stationary, homogeneous stochastic process, with a Gaussian probability density function. They are determined from these assumptions and the following properties:

$$\langle u'(s,t)\rangle = 0 \tag{5.1}$$

$$\langle u(s,t)u(s+r,t+\tau)\rangle = U^2 C(r,\tau) \tag{5.2}$$

where a prime denotes a fluctuation about the local mean value and angle brackets denote time-averaged quantities. The generated scalar field $u(s,t)$ is assumed to have a zero mean, a standard deviation $U = 1$ and to statistically satisfy a space-time correlation function:

$$C(r,\tau) = C_s(r)C_t(\tau) \tag{5.3}$$

where $C_s(r) = e^{-r/\Lambda}$ is the two-point/one-time correlation function and $C_t(\tau) = e^{-\tau/t_e}$ is the one-point/two-time correlation function, and Λ and t_e are the turbulence integral length scale and time scale, respectively. Kritzstein and Soufiani [129] studied the TRI effect for different forms of spatial correlation function and concluded that the contribution of turbulence on radiation is not very sensitive to the shape of the spatial correlation function. Therefore, in this study we only use exponential decay functions for both spatial and temporal correlation functions. Temperature and species concentration fields are generated by

$$T(s,t) = T_0\left[1 + \beta_T u'_T(s,t)\right] \tag{5.4a}$$

$$x(s,t) = x_0\left[1 + \beta_x u'_x(s,t)\right] \tag{5.4b}$$

where β_T and β_x represent the percentage of temperature and species concentration fluctuations around mean temperature and concentration T_0 and x_0, respectively. $u'_T(s,t)$ and $u'_x(s,t)$ are turbulent fluctuations used to generate temperature and species concentration fields satisfying properties as in Eqs. (5.1) and (5.2). The reader is referred to [129, 130] for more details on the approach of numerically generating the turbulent scalar fields.

Once temperature and species concentration fields along a line-of-sight are obtained, instantaneous spectral transmissvities $\tau_\eta(t)$ can be calculated as

$$\tau_\eta(t) = e^{-\int_0^L \kappa_\eta(T,x)\mathrm{d}s} \tag{5.5}$$

where $\kappa_\eta(T,x)$ is the spectral absorption coefficient calculated from the HITEMP 2010 line-by-line (LBL) database. Since transmissivity spectra can only be measured at a finite resolution by a spectrometer, the LBL spectral transmissvities of Eq. (5.5) have to be convolved with an pixel response function (PRF) to mimic the resolution of a spectrometer. After the transmissivity spectra are convolved with the PRF $\Gamma(\eta)$, they become,

$$\tau_{\eta c}(t) = \int_0^\infty \tau_\eta(t)\Gamma(\eta - \eta_1)\mathrm{d}\eta_1 \tag{5.6}$$

The PRF $\Gamma(\eta)$ is a property associated with the optical detector, and it can be determined by deconvolution of a measured spectrum. For an array detector, the PRF can also have the same shape as in Eq. 2.7 [131]. Therefore, Eq. 2.7 was also used as the PRF in this study. LBL spectral transmissivity are convolved with an PRF with nominal resolution of 4 cm^{-1} to create instantaneous medium-resolution transmissivity spectra based on the generated turbulent scalars filed.

Instantaneous scalar fields are created with an integral length scale of Λ for a gas medium of length L and with an integral time scale of t_e for a total time interval of t. Time-averaged transmissivity $\langle\tau_c(\eta)\rangle$ and its variance $\left\langle\tau'_c(\eta)^2\right\rangle$ can be obtained by conducting a stochastic analysis over the in-

stantaneous transmissivity of Eq. (5.6). These values are used as input data to retrieve time-averaged temperature $\langle T \rangle$, concentration $\langle x \rangle$ and their variances $\left\langle T'^2 \right\rangle$, $\left\langle x'^2 \right\rangle$ and $\langle T'x' \rangle$. The retrieved statistical data will be compared with the the ones directly calculated from the created turbulent scalar fields.

5.3 Forward calculation

In order to retrieved mean scalars and their rms values from optically measured transmissivity and its rms spectra, it is important to have an accurate forward calculation model that can relate the mean and rms transmissvities to the mean and rms values of temperature and concentration. It is assumed that the time-averaged transmissivity and its variance can be measured in a finite resolution. Also, it is assumed transmissivities vary temporally and the fluctuation has zero mean. The forward calculation model is using time-averaged temperature $\langle T \rangle$, concentration $\langle x \rangle$ and their variances $\left\langle T'^2 \right\rangle$, $\left\langle x'^2 \right\rangle$ and $\langle T'x' \rangle$ to predict the measured time-averaged transmissivity $\langle \tau_c(\eta) \rangle$ and its variance $\left\langle \tau_c'(\eta)^2 \right\rangle$, which involves several levels of calculation.

5.3.1 From temperature and concentration to LBL absorption coefficient

It is known that absorption coefficient κ_η tends to be relatively linear in T and x, and it is reasonable to assume that

$$\kappa_\eta(x,T) \approx \kappa_\eta\left(\langle T \rangle, \langle x \rangle\right) + \frac{\partial \kappa_\eta(\langle T \rangle, \langle x \rangle)}{\partial T} T' + \frac{\partial \kappa_\eta(\langle T \rangle, \langle x \rangle)}{\partial x} x' \tag{5.7}$$

where temperature and concentration fluctuations T' and x' are assumed to be Gaussian random variables with zero mean. Taking the average of Eq. (5.7) leads to

$$\left\langle \kappa_\eta \right\rangle \approx \kappa_\eta(\langle T \rangle, \langle x \rangle) \tag{5.8}$$

This basically means the time-averaged absorption coefficient can be calculated from time-averaged temperature and species concentration. The variance of the absorption coefficient is defined as the mean-square fluctuation of the absorption coefficient. Combining Eqs. (5.7) and (5.8), the variance of κ_η can be deduced as

$$\begin{aligned}\left\langle \kappa_\eta'^2 \right\rangle &= \left\langle \left(\kappa_\eta - \left\langle \kappa_\eta \right\rangle\right)^2 \right\rangle \approx \left\langle \left[\frac{\partial \kappa_\eta(\langle T \rangle, \langle x \rangle)}{\partial T} T' + \frac{\partial \kappa_\eta(\langle T \rangle, \langle x \rangle)}{\partial x} x' \right]^2 \right\rangle \\ &= \left[\frac{\partial \kappa_\eta(\langle T \rangle, \langle x \rangle)}{\partial T} \right]^2 \left\langle T'^2 \right\rangle + \left[\frac{\partial \kappa_\eta(\langle T \rangle, \langle x \rangle)}{\partial x} \right]^2 \left\langle x'^2 \right\rangle + 2 \frac{\partial \kappa_\eta(\langle T \rangle, \langle x \rangle)}{\partial T} \frac{\partial \kappa_\eta(\langle T \rangle, \langle x \rangle)}{\partial x} \langle T'x' \rangle\end{aligned} \tag{5.9}$$

Where $\left\langle \kappa_\eta'^2 \right\rangle$, $\left\langle T'^2 \right\rangle$ and $\left\langle x'^2 \right\rangle$ are variance of absorption coefficient κ_η, temperature T and species concentration x, respectively; $\langle T'x' \rangle$ is the covariance of temperature and species concentration.

5.3.2 From LBL absorption coefficient to LBL transmissivity

Because of the approximately linear relation between absorption coefficient, temperature and species concentration, the absorption coefficients also vary temporally with a Gaussian distribution, which have mean and variance of $\langle \kappa_\eta \rangle$ and $\langle \kappa_\eta'^2 \rangle$, respectively. It is known that

$$\begin{aligned} \tau_\eta =& e^{-\int_0^L \kappa_\eta(s)\mathrm{d}s} = e^{-\int_0^L \left[\langle \kappa_\eta \rangle + \kappa_\eta'(s)\right]\mathrm{d}s} \\ =& e^{-\langle \kappa_\eta \rangle L} e^{-\int_0^L \kappa_\eta'(s)\mathrm{d}s} \end{aligned} \tag{5.10}$$

Averaging over Eq. (5.10) yields

$$\langle \tau_\eta \rangle = e^{-\langle \kappa_\eta \rangle L} \left\langle e^{-\int_0^L \kappa_\eta'(s)\mathrm{d}s} \right\rangle \tag{5.11}$$

and the variance of the transmissivity can be written as

$$\langle \tau_\eta'^2 \rangle = \left\langle \left(\tau_\eta - \langle \tau_\eta \rangle\right)^2 \right\rangle = \left[e^{-\langle \kappa_\eta \rangle L}\right]^2 \left[\left\langle e^{-2\int_0^L \kappa_\eta'(s)\mathrm{d}s} \right\rangle - \left\langle e^{-\int_0^L \kappa_\eta'(s)\mathrm{d}s} \right\rangle^2\right] \tag{5.12}$$

Here we define $\chi_\eta = \int_0^L \kappa_\eta'(s)\mathrm{d}s$ as the turbulence optical thickness, which is a normally distributed random variable with mean $\langle \chi_\eta \rangle$ and variance $\langle \chi_\eta'^2 \rangle$. By definition, the positive random variable $e^{-\chi_\eta}$ is log-normally distributed with mean and variance of [132]

$$\langle e^{-\chi_\eta} \rangle = e^{-\langle \chi_\eta \rangle + \frac{1}{2}\langle \chi_\eta'^2 \rangle} \tag{5.13}$$

$$\mathrm{var}\left(e^{-\chi_\eta}\right) = \langle e^{-\chi_\eta} \rangle^2 \left(e^{\langle \chi_\eta'^2 \rangle} - 1\right) \tag{5.14}$$

In order to evaluate Eqs. (5.11) and (5.12), the mean and variance for the turbulence optical thickness χ_η need to be evaluated first. The mean is

$$\langle \chi_\eta \rangle = \left\langle \int_0^L \kappa_\eta'(s)\mathrm{d}s \right\rangle = \int_0^L \langle \kappa_\eta'(s) \rangle \mathrm{d}s = 0 \tag{5.15}$$

and its variance is

$$\langle \chi_\eta'^2 \rangle = \left\langle \left[\int_0^L \kappa_\eta'(s)\mathrm{d}s\right]^2 \right\rangle = \int_0^L \int_0^L \langle \kappa_\eta'(s_1)\kappa_\eta'(s_2) \rangle \mathrm{d}s_1 \mathrm{d}s_2 \tag{5.16}$$

where $\langle \kappa_\eta'(s_1)\kappa_\eta'(s_2) \rangle$ is the covariance of absorption coefficients at two different spatial locations s_1

and s_2, and according to Eqs. (5.7) and (5.8),

$$\begin{aligned}\left\langle \kappa'_\eta(s_1)\kappa'_\eta(s_2)\right\rangle &= \left\langle \left[\kappa_\eta(s_1)-\left\langle\kappa_\eta(s_1)\right\rangle\right]\left[\kappa_\eta(s_2)-\left\langle\kappa_\eta(s_2)\right\rangle\right]\right\rangle \\ &= \left(\frac{\partial\left\langle\kappa_\eta\right\rangle}{\partial T}\right)^2\left\langle T'(s_1)T'(s_2)\right\rangle + \left(\frac{\partial\left\langle\kappa_\eta\right\rangle}{\partial x}\right)^2\left\langle x'(s_1)x'(s_2)\right\rangle \\ &+ \frac{\partial\left\langle\kappa_\eta\right\rangle}{\partial T}\frac{\partial\left\langle\kappa_\eta\right\rangle}{\partial x}\left\langle T'(s_1)x'(s_2)\right\rangle + \frac{\partial\left\langle\kappa_\eta\right\rangle}{\partial x}\frac{\partial\left\langle\kappa_\eta\right\rangle}{\partial T}\left\langle x'(s_1)T'(s_2)\right\rangle \end{aligned} \tag{5.17}$$

For homogeneous turbulence,$\langle x'(s_1)T'(s_2)\rangle = \langle x'(s_2)T'(s_1)\rangle$, so Eq. (5.17) becomes,

$$\left\langle \kappa'_\eta(s_1)\kappa'_\eta(s_2)\right\rangle = \left(\frac{\partial\left\langle\kappa_\eta\right\rangle}{\partial T}\right)^2\left\langle T'(s_1)T'(s_2)\right\rangle + \left(\frac{\partial\left\langle\kappa_\eta\right\rangle}{\partial x}\right)^2\left\langle x'(s_1)x'(s_2)\right\rangle + 2\frac{\partial\left\langle\kappa_\eta\right\rangle}{\partial T}\frac{\partial\left\langle\kappa_\eta\right\rangle}{\partial x}\left\langle T'(s_1)x'(s_2)\right\rangle \tag{5.18}$$

If the turbulent fields have a spatial correlation function $C_s(r)$, where r is the distance between two arbitrary spatial locations, Eq. (5.18) can be rewritten as

$$\begin{aligned}\left\langle \kappa'_\eta(s_1)\kappa'_\eta(s_2)\right\rangle &= \left(\frac{\partial\left\langle\kappa_\eta\right\rangle}{\partial T}\right)^2 C_s(|s_1-s_2|)\left\langle T'^2\right\rangle + \left(\frac{\partial\left\langle\kappa_\eta\right\rangle}{\partial x}\right)^2 C_s(|s_1-s_2|)\left\langle x'^2\right\rangle \\ &+ 2\frac{\partial\left\langle\kappa_\eta\right\rangle}{\partial T}\frac{\partial\left\langle\kappa_\eta\right\rangle}{\partial x}C_s(|s_1-s_2|)\left\langle T'x'\right\rangle \end{aligned} \tag{5.19}$$

let

$$\theta^2 = \frac{1}{L^2}\int_0^L\int_0^L C_s(|s_1-s_2|)\mathrm{d}s_1\mathrm{d}s_2 \tag{5.20}$$

then Eq. (5.16) becomes,

$$\left\langle \chi'^2_\eta\right\rangle = \left\langle \kappa'^2_\eta\right\rangle\theta^2L^2 \tag{5.21}$$

Up to here, we have calculated the mean and variance of the turbulence optical thickness χ_η. Applying Eqs. (5.13) and (5.14) to Eqs. (5.11) and (5.12) yields the mean value for the LBL transmissivity

$$\left\langle\tau_\eta\right\rangle = e^{-\langle\kappa_\eta\rangle L}e^{\frac{1}{2}\left\langle\kappa'^2_\eta\right\rangle L^2\theta^2} \tag{5.22}$$

and variance for LBL transmissivity

$$\left\langle\tau'^2_\eta\right\rangle = \left\langle\tau_\eta\right\rangle^2\left[e^{\left\langle\kappa'^2_\eta\right\rangle L^2\theta^2}-1\right] \tag{5.23}$$

5.3.3 Convolution

In the forward calculation, the calculated LBL spectral transmissivity has to be convolved with a pixel response function (PRF) to mimic the resolution of a spectrometer. After transmissivity spectra are convolved with the PRF $\Gamma(\eta)$, they become,

$$\tau_{\eta c} = \int_0^\infty \tau_{\eta_1} \Gamma(\eta - \eta_1) \mathrm{d}\eta_1 \tag{5.24}$$

After convolution, the time-averaged transmissivity can be rewritten as,

$$\begin{aligned} \left\langle \tau_{\eta c} \right\rangle &= \left\langle \int_0^\infty \tau_{\eta_1} \Gamma(\eta - \eta_1) \mathrm{d}\eta_1 \right\rangle \\ &= \int_0^\infty \left\langle \tau_{\eta_1} \right\rangle \Gamma(\eta - \eta_1) \mathrm{d}\eta_1 \end{aligned} \tag{5.25}$$

This implies that the convoluted time-averaged lower-resolution transmissivity equals the convolution of the time-averaged LBL transmissivity.

The variance of the convoluted transmissivity is

$$\begin{aligned} \left\langle \tau'^2_{\eta c} \right\rangle &= \left\langle \left[\int_0^\infty \tau_{\eta_1} \Gamma(\eta - \eta_1) \mathrm{d}\eta_1 - \int_0^\infty \left\langle \tau_{\eta_1} \right\rangle \Gamma(\eta - \eta_1) \mathrm{d}\eta_1 \right]^2 \right\rangle \\ &= \left\langle \left[\int_0^\infty \tau'_{\eta_1} \Gamma(\eta - \eta_1) \mathrm{d}\eta_1 \right]^2 \right\rangle \\ &= \int_0^\infty \int_0^\infty \left\langle \tau'_{\eta_1} \tau'_{\eta_2} \right\rangle \Gamma(\eta - \eta_1) \Gamma(\eta - \eta_2) \mathrm{d}\eta_1 \mathrm{d}\eta_2 \end{aligned} \tag{5.26}$$

where $\left\langle \tau'_{\eta_1} \tau'_{\eta_2} \right\rangle$ is the covariance of transmissivity τ_η at two arbitrary wavenumber locations η_1 and η_2, where the transmissivity fluctuation is

$$\tau'_\eta = e^{-\langle \kappa_\eta \rangle L} e^{-\int_0^L \kappa'_\eta(s)\mathrm{d}s} - e^{-\langle \kappa_\eta \rangle L} e^{\frac{1}{2}\left\langle \chi'^2_\eta \right\rangle} \tag{5.27}$$

then $\tau'_{\eta_1} \tau'_{\eta_2}$ can be expressed as

$$\tau'_{\eta_1} \tau'_{\eta_2} = e^{-(\langle \kappa_{\eta_1} \rangle + \langle \kappa_{\eta_2} \rangle) L} \left(e^{-\int_0^L \kappa'_{\eta_1}(s)\mathrm{d}s} - e^{\frac{1}{2}\left\langle \chi'^2_{\eta_1} \right\rangle} \right) \left(e^{-\int_0^L \kappa'_{\eta_2}(s)\mathrm{d}s} - e^{\frac{1}{2}\left\langle \chi'^2_{\eta_2} \right\rangle} \right) \tag{5.28}$$

Taking the average of Eq. (5.28) yields the covariance of τ_{η_1} and τ_{η_2},

$$\begin{aligned} \left\langle \tau'_{\eta_1} \tau'_{\eta_2} \right\rangle =& e^{-\left(\langle \kappa_{\eta_1} \rangle + \langle \kappa_{\eta_2} \rangle\right) L} \left(\left\langle e^{-\int_0^L \left(\kappa'_{\eta_1} + \kappa'_{\eta_2}\right)\mathrm{d}s} \right\rangle + e^{\frac{1}{2}\left(\left\langle \chi'^2_{\eta_1} \right\rangle + \left\langle \chi'^2_{\eta_2} \right\rangle\right)} - \left\langle e^{-\int_0^L \kappa'_{\eta_1}(s)\mathrm{d}s} \right\rangle e^{\frac{1}{2}\left\langle \chi'^2_{\eta_2} \right\rangle} - e^{\frac{1}{2}\left\langle \chi'^2_{\eta_1} \right\rangle} \left\langle e^{-\int_0^L \kappa'_{\eta_2}(s)\mathrm{d}s} \right\rangle \right) \\ =& e^{-\left(\langle \kappa_{\eta_1} \rangle + \langle \kappa_{\eta_2} \rangle\right) L} \left(\left\langle e^{-\int_0^L (\kappa'_{\eta_1} + \kappa'_{\eta_2})\mathrm{d}s} \right\rangle - e^{\frac{1}{2}\left(\left\langle \chi'^2_{\eta_1} \right\rangle + \left\langle \chi'^2_{\eta_2} \right\rangle\right)} \right) \end{aligned} \tag{5.29}$$

and it is known that

$$\left\langle \int_0^L (\kappa'_{\eta_1} + \kappa'_{\eta_2}) \mathrm{d}s \right\rangle = \int_0^L \left\langle (\kappa'_{\eta_1} + \kappa'_{\eta_2}) \right\rangle \mathrm{d}s = 0 \tag{5.30}$$

and

$$\begin{aligned}\left\langle \left[\int_0^L (\kappa'_{\eta_1} + \kappa'_{\eta_2}) \mathrm{d}s \right]^2 \right\rangle &= \int_0^L \int_0^L \left\langle \left[\kappa'_{\eta_1}(s_1) + \kappa'_{\eta_2}(s_1) \right] \left[\kappa'_{\eta_1}(s_2) + \kappa'_{\eta_2}(s_2) \right] \right\rangle \mathrm{d}s_1 \mathrm{d}s_2 \\ &= \left\langle \chi'^2_{\eta_1} \right\rangle + \left\langle \chi'^2_{\eta_2} \right\rangle + 2 \int_0^L \int_0^L \left\langle \kappa'_{\eta_1}(s_1) \kappa'_{\eta_2}(s_2) \right\rangle \mathrm{d}s_1 \mathrm{d}s_2 \\ &= \left\langle \chi'^2_{\eta_1} \right\rangle + \left\langle \chi'^2_{\eta_2} \right\rangle + 2 \left\langle \chi'_{\eta_1} \chi'_{\eta_2} \right\rangle \end{aligned} \tag{5.31}$$

where $\left\langle \chi'_{\eta_1} \chi'_{\eta_2} \right\rangle = \int_0^L \int_0^L \left\langle \kappa'_{\eta_1}(s_1) \kappa'_{\eta_2}(s_2) \right\rangle \mathrm{d}s_1 \mathrm{d}s_2$ is the covariance of turbulent optical thickness at two arbitrary wavenumber locations η_1 and η_2 and $\left\langle \kappa'_{\eta_1}(s_1) \kappa'_{\eta_2}(s_2) \right\rangle$ is the covariance of absorption coefficients at two arbitrary wavenumber locations η_1 and η_2 as well as at two arbitrary spatial locations s_1 and s_2, which can be calculated from

$$\begin{aligned}\left\langle \kappa'_{\eta_1}(s_1) \kappa'_{\eta_2}(s_2) \right\rangle =& \frac{\partial \left\langle \kappa_{\eta_1} \right\rangle}{\partial T} \frac{\partial \left\langle \kappa_{\eta_2} \right\rangle}{\partial T} \left\langle T'(s_1) T'(s_2) \right\rangle + \frac{\partial \left\langle \kappa_{\eta_1} \right\rangle}{\partial x} \frac{\partial \left\langle \kappa_{\eta_2} \right\rangle}{\partial x} \left\langle x'(s_1) x'(s_2) \right\rangle \\ &+ \left(\frac{\partial \left\langle \kappa_{\eta_1} \right\rangle}{\partial T} \frac{\partial \left\langle \kappa_{\eta_2} \right\rangle}{\partial x} + \frac{\partial \left\langle \kappa_{\eta_1} \right\rangle}{\partial x} \frac{\partial \left\langle \kappa_{\eta_2} \right\rangle}{\partial T} \right) \left\langle T'(s_1) x'(s_2) \right\rangle \end{aligned} \tag{5.32}$$

For turbulent fields with a spatial correlation function $C_s(r)$, the covariance of turbulent optical thickness $\left\langle \chi'_{\eta_1} \chi'_{\eta_2} \right\rangle$ can be calculated as

$$\begin{aligned}\left\langle \chi'_{\eta_1} \chi'_{\eta_2} \right\rangle =& \int_0^L \int_0^L \left\langle \kappa'_{\eta_1}(s_1) \kappa'_{\eta_2}(s_2) \right\rangle \mathrm{d}s_1 \mathrm{d}s_2 \\ =& \frac{\partial \left\langle \kappa_{\eta_1} \right\rangle}{\partial T} \frac{\partial \left\langle \kappa_{\eta_2} \right\rangle}{\partial T} \left\langle T'^2 \right\rangle \int_0^L \int_0^L C_s(|s_1 - s_2|) \mathrm{d}s_1 \mathrm{d}s_2 + \frac{\partial \left\langle \kappa_{\eta_1} \right\rangle}{\partial x} \frac{\partial \left\langle \kappa_{\eta_2} \right\rangle}{\partial x} \left\langle x'^2 \right\rangle \int_0^L \int_0^L C_s(|s_1 - s_2|) \mathrm{d}s_1 \mathrm{d}s_2 \\ &+ \left(\frac{\partial \left\langle \kappa_{\eta_1} \right\rangle}{\partial T} \frac{\partial \left\langle \kappa_{\eta_2} \right\rangle}{\partial x} + \frac{\partial \left\langle \kappa_{\eta_1} \right\rangle}{\partial x} \frac{\partial \left\langle \kappa_{\eta_2} \right\rangle}{\partial T} \right) \left\langle T' x' \right\rangle \int_0^L \int_0^L C_s(|s_1 - s_2|) \mathrm{d}s_1 \mathrm{d}s_2 \\ =& \theta^2 L^2 \left[\frac{\partial \left\langle \kappa_{\eta_1} \right\rangle}{\partial T} \frac{\partial \left\langle \kappa_{\eta_2} \right\rangle}{\partial T} \left\langle T'^2 \right\rangle + \frac{\partial \left\langle \kappa_{\eta_1} \right\rangle}{\partial x} \frac{\partial \left\langle \kappa_{\eta_2} \right\rangle}{\partial x} \left\langle x'^2 \right\rangle + \left(\frac{\partial \left\langle \kappa_{\eta_1} \right\rangle}{\partial T} \frac{\partial \left\langle \kappa_{\eta_2} \right\rangle}{\partial x} + \frac{\partial \left\langle \kappa_{\eta_1} \right\rangle}{\partial x} \frac{\partial \left\langle \kappa_{\eta_2} \right\rangle}{\partial T} \right) \left\langle T' x' \right\rangle \right] \end{aligned} \tag{5.33}$$

So Eq. (5.29) reduces to

$$\begin{aligned}\left\langle \tau'_{\eta_1}\tau'_{\eta_2}\right\rangle =& e^{-(\langle\kappa_{\eta_1}\rangle+\langle\kappa_{\eta_2}\rangle)L}e^{\frac{1}{2}\left\langle\chi'^2_{\eta_1}\right\rangle+\frac{1}{2}\left\langle\chi'^2_{\eta_2}\right\rangle}\left(e^{\left\langle\chi'_{\eta_1}\chi'_{\eta_2}\right\rangle}-1\right)\\ =&\left\langle\tau_{\eta_1}\right\rangle\left\langle\tau_{\eta_2}\right\rangle\left(e^{\left\langle\chi'_{\eta_1}\chi'_{\eta_2}\right\rangle}-1\right)\\ \approx&\left\langle\tau_{\eta_1}\right\rangle\left\langle\tau_{\eta_2}\right\rangle\left\langle\chi'_{\eta_1}\chi'_{\eta_2}\right\rangle\end{aligned} \tag{5.34}$$

and Eq. (5.26) becomes

$$\left\langle\tau'^2_{\eta c}\right\rangle=\int_0^\infty\int_0^\infty\left(\left\langle\tau_{\eta_1}\right\rangle\left\langle\tau_{\eta_2}\right\rangle\left\langle\chi'_{\eta_1}\chi'_{\eta_2}\right\rangle\right)\Gamma(\eta-\eta_1)\Gamma(\eta-\eta_2)\mathrm{d}\eta_1\mathrm{d}\eta_2 \tag{5.35}$$

5.4 Inverse calculation

The present study is limited to homogeneous turbulent fields of a N_2+CO_2, N_2+H_2O or N_2+CO mixtures and, therefore, the parameters that need to be determined are the time-averaged temperature $\langle T\rangle$ and concentration $\langle x\rangle$, the variance of temperature $\left\langle T'^2\right\rangle$ and concentration $\left\langle x'^2\right\rangle$, and the covariance of temperature and concentration $\langle T'x'\rangle$. Usually, the turbulence length scale Λ is an unknown parameter, so it also need to be determined.

Assuming time-averaged transmissivity and its variance can be optically measured at a relatively low resolution, generally the equations we need to solve to obtain all the parameters are

$$\left\langle\tau_{\eta c}\right\rangle=f_\eta\left(\langle T\rangle,\langle x\rangle,\left\langle T'^2\right\rangle,\left\langle x'^2\right\rangle,\langle T'x'\rangle,\Lambda\right) \tag{5.36}$$

or

$$\left\langle\tau'^2_{\eta c}\right\rangle=g_\eta\left(\langle T\rangle,\langle x\rangle,\left\langle T'^2\right\rangle,\left\langle x'^2\right\rangle,\langle T'x'\rangle,\Lambda\right) \tag{5.37}$$

where the nonlinear functions f_η and g_η can be determined with Eqs. (5.25) and (5.26), respectively. In principle, either of Eqs. (5.36) and (5.37) can be used to solve all the parameters if one measures the time-averaged transmissivity or the variance of transmissivity with a certain spectral resolution, obtaining enough discrete values at different wavenumbers. However, these two equations show different sensitivity to different parameters, as indicated in Eqs. (5.22) and (5.23). In Eq. (5.22), the term $e^{\frac{1}{2}\left\langle\kappa'^2_\eta\right\rangle L^2\theta^2}$ gives the effect of turbulent fluctuations on transmissivity of the gaseous medium. It is easy to demonstrate this term is larger than unity, which means turbulent fluctuations increase transmissivity. But if the optical thickness of the gas medium based on the turbulent integral length scale ($\kappa_\eta\Lambda$) is small, this term is always close to unity, i.e., time-averaged transmissivity is not sensitive to the intensity of turbulence fluctuations. By contrast, as shown in Eq. (5.23), turbulent fluctuations always have significant effects on the fluctuation of transmissivities. Deducing $\langle T\rangle$, $\langle x\rangle$, $\left\langle T'^2\right\rangle$, $\left\langle x'^2\right\rangle$, $\langle T'x'\rangle$ and Λ from Eqs. (5.36) or (5.37) requires deconvolution and makes these problems ill-posed and, therefore these equations cannot be inverted directly to obtain all the parameters. Inverse procedures are required to solve them numerically. In this study, time-averaged temperature $\langle T\rangle$ and concentration $\langle x\rangle$ are solved by minimizing an objective function F_1, which represents the

difference between the predicted and measured time-averaged transmissivity, i.e.,

$$F_1(\mathbf{z}_1) = \sum_{i=1}^{I} (\langle \tau_{ic} \rangle - f_i)^2 \tag{5.38}$$

where i denotes discrete wavenumber. The variance of temperature $\left\langle T'^2 \right\rangle$ and concentration $\left\langle x'^2 \right\rangle$, the covariance of temperature and concentration $\langle T'x' \rangle$ and the turbulence length scale Λ are solved by minimizing an objective function F_2, which represents the difference between the predicted and measured variance of transmissivity, i.e.,

$$F_2(\mathbf{z}_2) = \sum_{i=1}^{I} \left(\left\langle \tau_{ic}'^2 \right\rangle - g_i \right)^2 \tag{5.39}$$

Here we separate all unknown parameters into two parameter vectors, where $\mathbf{z}_1 = (\langle T \rangle, \langle x \rangle)^T$ is solved from Eq. (5.38) and $\mathbf{z}_2 = \left(\left\langle T'^2 \right\rangle, \left\langle x'^2 \right\rangle, \langle T'x' \rangle, \Lambda \right)^T$ is solved from Eq. (5.39). The goal of inverse calculations is to minimize these two functions by properly guessing the parameter vectors until the best matches between the measured spectra and predicted spectra data are achieved. In our previous study [121, 122], the Levenberg-Marquardt optimization method was applied to retrieve temperatures and species concentrations for laminar gaseous media. We found the Levenberg-Marquardt optimization method to be relatively reliable, more accurate and requiring less computational effort than several other methods tested. Therefore, the Levenberg-Marquardt is also employed in the present study. In this method, the parameter vector $\mathbf{z}$ is gradually increased by a small value $\vec{\delta z}$,

$$\mathbf{z}_{new} = \mathbf{z}_{old} + \delta \mathbf{z} \tag{5.40}$$

with

$$\delta \mathbf{z} = -H'^{-1} B \tag{5.41}$$

and the vector $B = \nabla F(\mathbf{z})$ is the gradient vector of the objective function F with respect to $\mathbf{z}$, and $\mathbf{H}'$ is a matrix with elements

$$h'_{ij} = \begin{cases} (1 + \lambda) h_{ij} & i = j \\ h_{ij} & i \neq j \end{cases} \tag{5.42}$$

where the h_{ij} are the elements of the Hessian matrix $\mathbf{H} = \nabla^2 F(\mathbf{z})$.

The same algorithm in Chapter 2 was applied to retrieve $\mathbf{z}_1$ and $\mathbf{z}_2$ separately, the procedure for retrieving all the parameters is summarized as follows

1. Assume starting points for $\mathbf{z}_1$ and $\mathbf{z}_2$.
2. Fix $\mathbf{z}_2$ and apply the Levenberg-Marquardt method to Eq. (5.38) to update $\mathbf{z}_1$.
3. With the updated $\mathbf{z}_1$, apply the Levenberg-Marquardt method again to Eq. (5.39) to update $\mathbf{z}_2$.
4. With the updated $\mathbf{z}_2$, go back to 2 and update $\mathbf{z}_1$ again.

5. Stop iteration when the changes of $\mathbf{z}_1$ and $\mathbf{z}_2$ become sufficiently small

5.5 Results and discussion

Instantaneous turbulence fields were generated assuming that the mean temperature T_0 of the gas medium is 1500 K and mean species concentration x_0 is 0.1. Temperature and species concentration have 10% fluctuations around the mean values. These values were chosen to represent physical conditions, which are typical of the far-field self-preserving region of a turbulent reacting jet, downstream of the location where combustion has taken place [133]. Temperature and species concentration fields are created for 100 spatial points along the gas column of 1 m and for 1000 time realizations in 1 s. The integral length and time scales are 0.1 m (Λ=0.1 L) and 0.1ms, respectively, which makes a spatially correlated and temporally independent turbulence field. Figure 5.1 shows representative spatial temperature fluctuations at an arbitrary time and temporal temperature fluctuations at an arbitrary location for the created turbulent temperature field. Figure 5.2 shows typical correlation functions computed from the stochastic scalars fields as described above, averaged over 1000 time realizations for all the spatial points, which is compared with the theoretical spatial correlation function $C_s(r) = e^{-r/\Lambda}$. Instantaneous transmissvities $\tau_{\eta c}$ are calculated from Eq. (5.6) for the instantaneous temperature and species concentration fields for CO_2, H_2O and CO. Stochastic analysis was conducted to calculate the time-averaged transmissivity and their rms spectra, which are denoted as "actual" spectra and were used to retrieve temperature $\langle T \rangle$, concentration $\langle x \rangle$ and their variance $\left\langle T'^2 \right\rangle$, $\left\langle x'^2 \right\rangle$ and $\langle T'x' \rangle$ for the three species from the inverse calculation model. On the other hand, these mean and rms values can also be directly calculated from the turbulence fields by conducting a stochastic analysis and the results are shown in Table 5.1, denoted as "actual values", which are used as the benchmark for the retrieved values from inverse calculations.

The "actual" time-averaged transmissivity and their rms spectra for CO_2, H_2O and CO were used to retrieve temperature, concentration, their rms values and turbulent length scale. The performance of different spectral bands for inverse calculation was investigated, and the retrieved results are shown in Table 5.1. *Actual* transmissivity and their rms spectra are compared with the spectra calculated with the *retrieved* parameter values in Table 5.1 from Eqs. (5.25) and (5.26) and also compared with the spectra calculated from *forward* calculations with the actual parameter values in Table 5.1 from Eqs. (5.25) and (5.26). All comparisons are shown in Figs. 5.3, 5.4 and 5.5.

Two CO_2 spectral bands at 4.3 and 2.7 μm were tested. The retrieved parameters are shown in Table 5.1. Large errors occur when retrieving rms values for CO_2 concentration from the 4.3 μm band and the retrieved turbulent length scale also has a relatively large discrepancy from the actual value. For the CO_2 2.7 μm band all retrieved results are very accurate: differences from actual parameter values are less than 1%. Figure 5.3 shows the comparison of retrieved transmissivity and their rms spectra with the "actual" spectra and forward spectra for the CO_2 4.3 and 2.7 μm bands. It appears that the forward calculated transmissivity and the rms spectra are overestimated at lower wavenumbers for the CO_2 4.3 μm band compared with the "actual" spectra. In the forward calculation model, we invoke the assumption that the spectral absorption coefficient is only a linear function over the temperature range of $\langle T \rangle \pm T'_{max}$ and species concentration rang of $\langle x \rangle \pm x'_{max}$, as given by Eq. (5.7). The linear assumption for absorption coefficients with concentration is valid due to weak self-broadening effects of CO_2. However, for the the CO_2 4.3 μm band, the spectral absorp-

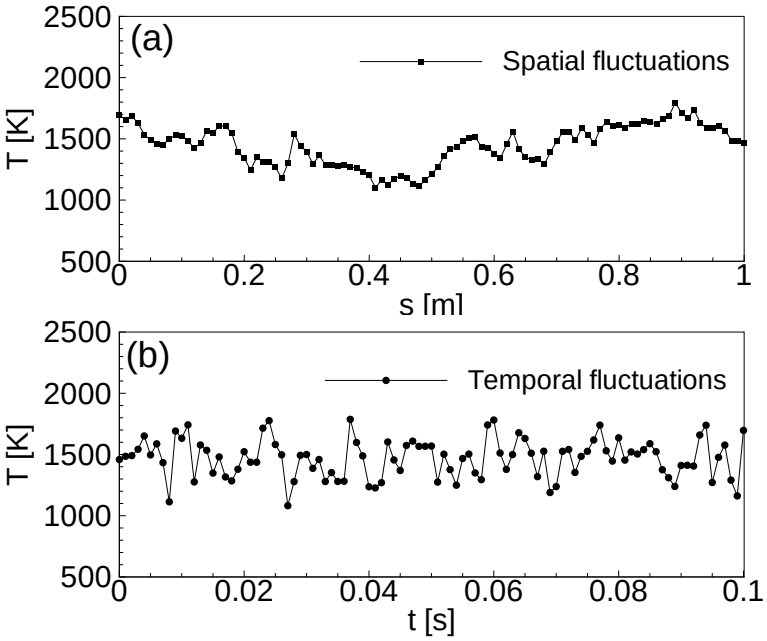

Figure 5.1: Demonstration of (a): spatial temperature fluctuations at an arbitrary time and (b) temporal temperature fluctuations at an arbitrary location

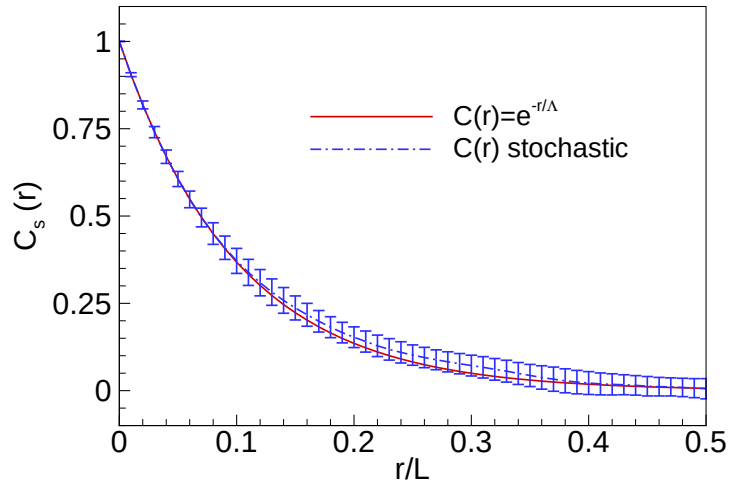

Figure 5.2: Comparison of theoretical spatial correlation function $C_s(r) = e^{-r/\Lambda}$ with the correlation function calculated from the created turbulence fields

tion coefficient may be slightly nonlinear over the temperature range 1500±150 K. Comparing to the CO_2 2.7 μm band, the CO_2 4.3 μm band is so strong that slightly nonlinearity may cause large

Table 5.1: Inverse calculation results for retrieving temperatures, species concentrations, their rms values and turbulent length scales from time-averaged transmissivity spectra and their rms spectra

retrieved parameters		$\langle T\rangle$ (K)	$\langle x\rangle$	$\sqrt{\langle T'^2\rangle}$ (K)	$\sqrt{\langle x'^2\rangle}$	$\langle T'x'\rangle$ (K)	Λ/L
actual values		1495.13	0.0997	150.83	0.0101	1.52	0.100
CO_2 4.3 μm	retrieved	1524.29	0.1017	145.21	0.0125	1.54	0.092
(1900 to 2500 cm^{-1})	error(%)	1.95	2.04	−3.73	24.21	1.78	−7.93
CO_2 2.7 μm	retrieved	1498.20	0.0995	149.46	0.0101	1.52	0.099
(3300 to 3800 cm^{-1})	error(%)	0.21	−0.19	−0.91	0.64	−0.07	−0.78
H_2O 2.7 μm	retrieved	1490.04	0.0994	151.03	0.0098	1.51	0.102
(3200 to 4200 cm^{-1})	error(%)	−0.34	−0.26	0.13	−3.04	−0.24	1.58
H_2O 1.8 μm	retrieved	1491.38	0.0994	149.64	0.0101	1.54	0.099
(4800 to 5800 cm^{-1})	error(%)	−0.25	−0.24	−0.79	0.04	1.49	−1.37
CO 4.7 μm	retrieved	1495.54	0.1006	149.52	0.0100	1.49	0.099
(1800 to 2400 cm^{-1})	error(%)	0.03	0.95	−0.87	−0.25	−1.57	−0.75
CO 2.3 μm	retrieved	1497.42	0.1000	149.79	0.0095	1.49	0.100
(3900 to 4400 cm^{-1})	error(%)	0.15	0.36	−0.69	−5.43	−1.71	0.07

discrepancies for larger optical thickness ($\langle\kappa_\eta\rangle L$). This is easy to demonstrate from Eqs. (5.22) and (5.23).

Two H_2O spectral bands at 2.7 μm and 1.8 μm and two CO spectral bands at 4.7 μm and 1.8 μm were also tested using transmissivity data synthesized from the turbulence fields. Table 5.1 shows the inverse results and Figs. 5.4 and 5.5 show the comparison of retrieved transmissivity and their rms spectra with the "actual" spectra and spectra calculated from froward calculation model. For these H_2O and CO transmissivity spectral bands, retrieved and forward spectra perfectly overlap with the "actual" spectra. Although "actual" and forward rms spectra show discrepancies with the "actual" rms spectra at smaller rms values, the spectral peaks and most part of the "actual" rms spectra bands are well captured by the retrieved and forward rms spectra. This shows that the forward calculations for predicting lower-resolution time-averaged transmissivities and their rms values are accurate enough and the resulting inverse radiation model provides a reliable tool for retrieving mean temperature, concentration, their rms values and turbulent length scale from turbulent transmissivity measurements.

All the previous test cases are for perfectly correlated temperature and species concentration fields, i.e., $u_T = u_x$ as in Eqs. (5.4a) and (5.4a). Although experiments show there are strong correlations between temperature and species concentration for flame [134], for our proposed method, there is no pre-assumption for the correlation between temperature and species concentration. Time-averaged temperature and species concentration are retrieved simultaneously and independently. Table 5.2 shows the results for non-correlated temperature and species concentration fields (other conditions remain the same). Except large errors occur when retrieving rms values for species concentration from the strong CO_2 4.3 μm band in this case, acceptable results are obtained from the CO_2 2.7 μm band as well as from other bands of the other two species.

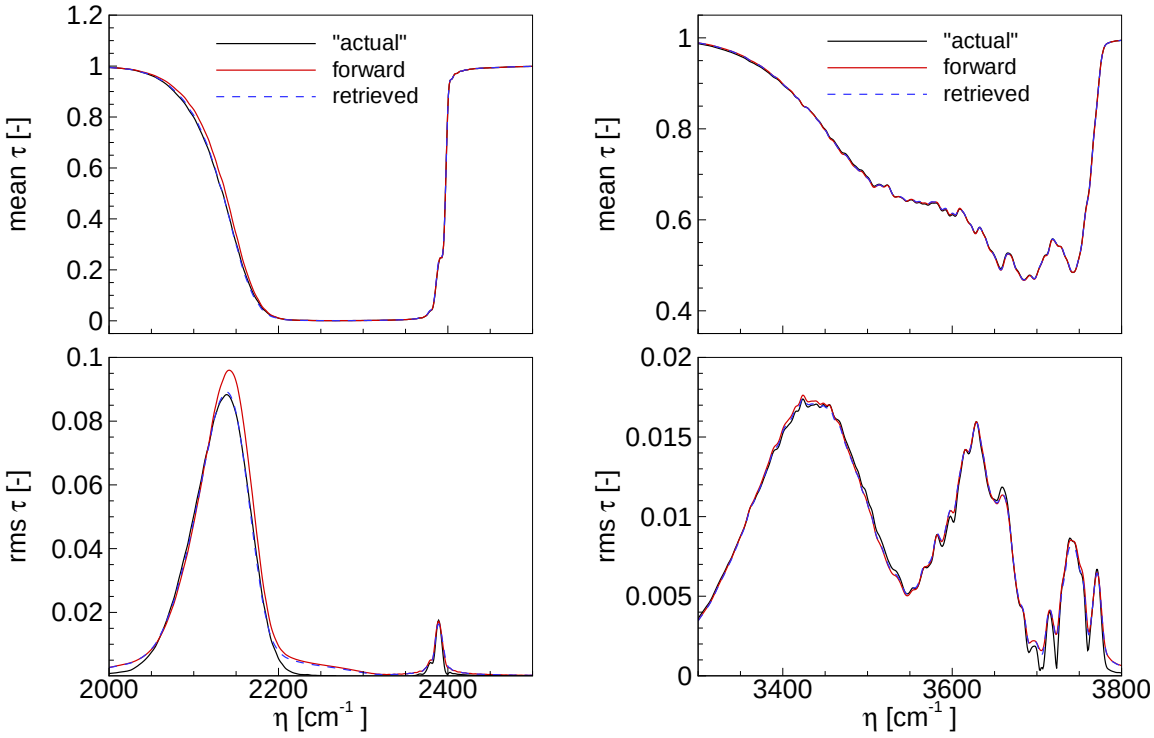

Figure 5.3: Comparison of retrieved transmissivity and its rms spectra with the "actual" spectra and forward spectra calculated by the actual turbulent scalars for the CO_2 4.3 μm and 2.7 μm bands

Table 5.2: Inverse calculation results for retrieving temperatures, species concentrations, their rms values and turbulent length scales from time-averaged transmissivity spectra and their rms spectra for non-correlated temperature and species concentration fields.

retrieved parameters		$\langle T \rangle$ (K)	$\langle x \rangle$	$\sqrt{\langle T'^2 \rangle}$ (K)	$\sqrt{\langle x'^2 \rangle}$	$\langle T'x' \rangle$ (K)	Λ/L
actual values		1495.13	0.1001	150.83	0.0101	0.00	0.100
CO_2 4.3 μm	retrieved	1510.14	0.1021	143.82	0.0151	0.08	0.091
(1900 to 2500 cm^{-1})	error(%)	1.00	2.06	−4.65	49.70	–	−8.70
CO_2 2.7 μm	retrieved	1483.07	0.0999	150.59	0.0100	−0.05	0.101
(3300 to 3800 cm^{-1})	error(%)	−0.81	−0.17	−0.16	−0.99	–	1.08
H_2O 2.7 μm	retrieved	1474.62	0.0998	154.58	0.0090	-0.05	0.107
(3200 to 4200 cm^{-1})	error(%)	−1.37	−0.24	2.48	−11.03	–	6.61
H_2O 1.8 μm	retrieved	1475.93	0.0998	154.10	0.0088	-0.05	0.106
(4800 to 5800 cm^{-1})	error(%)	−1.28	−0.24	2.16	−12.72	–	5.94
CO 4.7 μm	retrieved	1480.19	0.1010	152.62	0.0094	-0.15	0.104
(1800 to 2400 cm^{-1})	error(%)	−1.00	0.99	1.18	−6.96	–	4.18
CO 2.3 μm	retrieved	1482.02	0.1004	151.55	0.0094	-0.13	0.102
(3900 to 4400 cm^{-1})	error(%)	−0.88	0.38	0.48	−6.16	–	1.85

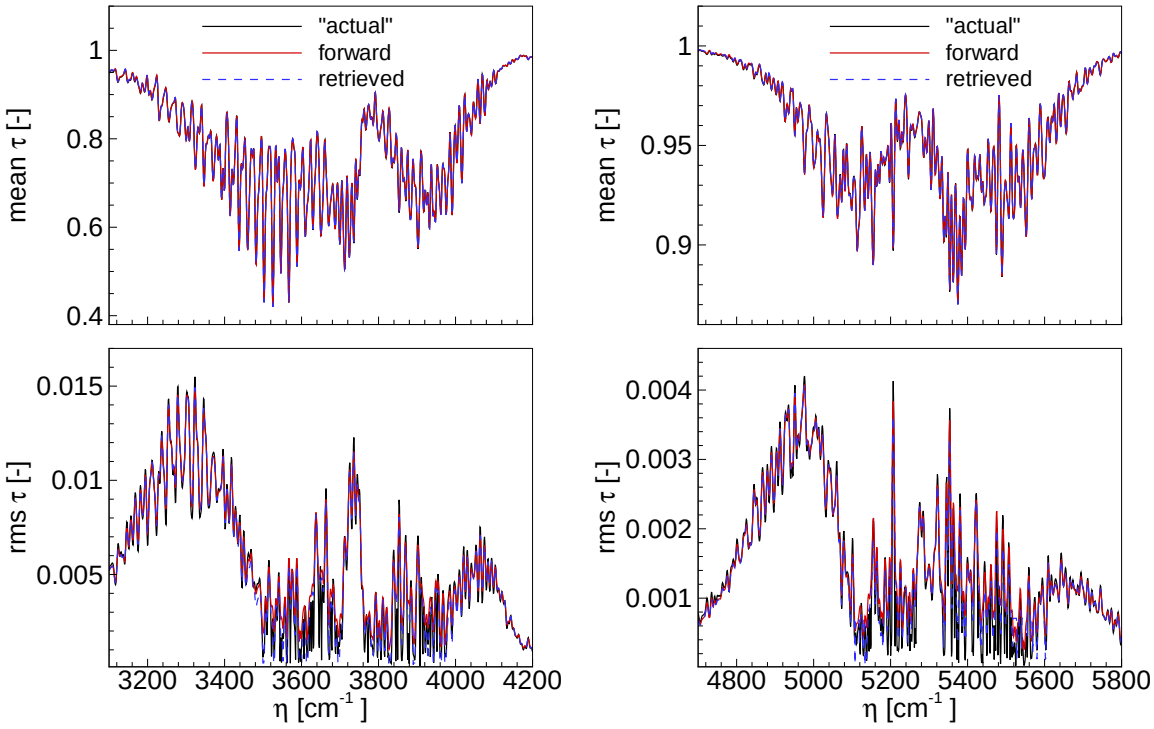

Figure 5.4: Comparison of retrieved transmissivity and its rms spectra with the "actual" spectra and forward spectra calculated by the actual turbulent scalars for the H_2O 2.7 μm and 1.8 μm bands

5.6 Inverse radiation model for turbulent gas mixture

The previous study is also for a single combustion species. In this section, the model was extended to retrieve time-averaged and rms values for temperature, species concentrations as well as turbulence length scale for gas mixture of three major combustion products CO_2, H_2O and CO with N_2. The spectral absorption coefficient for the gas mixture can be approximated linearly as

$$\begin{aligned}\kappa_\eta(T,\mathbf{x}) \approx & \kappa_\eta\left(\langle T\rangle,\langle\mathbf{x}\rangle\right)+\frac{\partial\kappa_\eta(\langle T\rangle,\langle\mathbf{x}\rangle)}{\partial T}T' \\ & +\frac{\partial\kappa_\eta(\langle T\rangle,\langle x_{CO_2}\rangle)}{\partial x_{CO_2}}x'_{CO_2}+\frac{\partial\kappa_\eta(\langle T\rangle,\langle x_{H_2O}\rangle)}{\partial x_{H_2O}}x'_{H_2O}+\frac{\partial\kappa_\eta(\langle T\rangle,\langle x_{CO}\rangle)}{\partial x_{CO}}x'_{CO}\end{aligned} \tag{5.43}$$

where $\mathbf{x} = [x_{CO_2}, x_{H_2O}, x_{CO}]$ is a set consisting of all the species concentrations. Based on the absorption coefficient for the gas mixture, a similar approach can be applied to a gas mixture and equations for time-averaged lower-resolution transmissivity and its variance can be derived accordingly. For a gas mixture of CO_2, H_2O and CO with N_2, Eqs. (5.36) and (5.37) can be rewritten as

$$\left\langle\tau_{\eta c}\right\rangle = f_\eta\left(\langle T\rangle,\langle x_i\rangle,\left\langle T'^2\right\rangle,\left\langle x_i'^2\right\rangle,\left\langle T'x_i'\right\rangle,\left\langle x_i'x_j'\right\rangle,\Lambda\right) \qquad i,j = CO_2, H_2O, CO \tag{5.44}$$

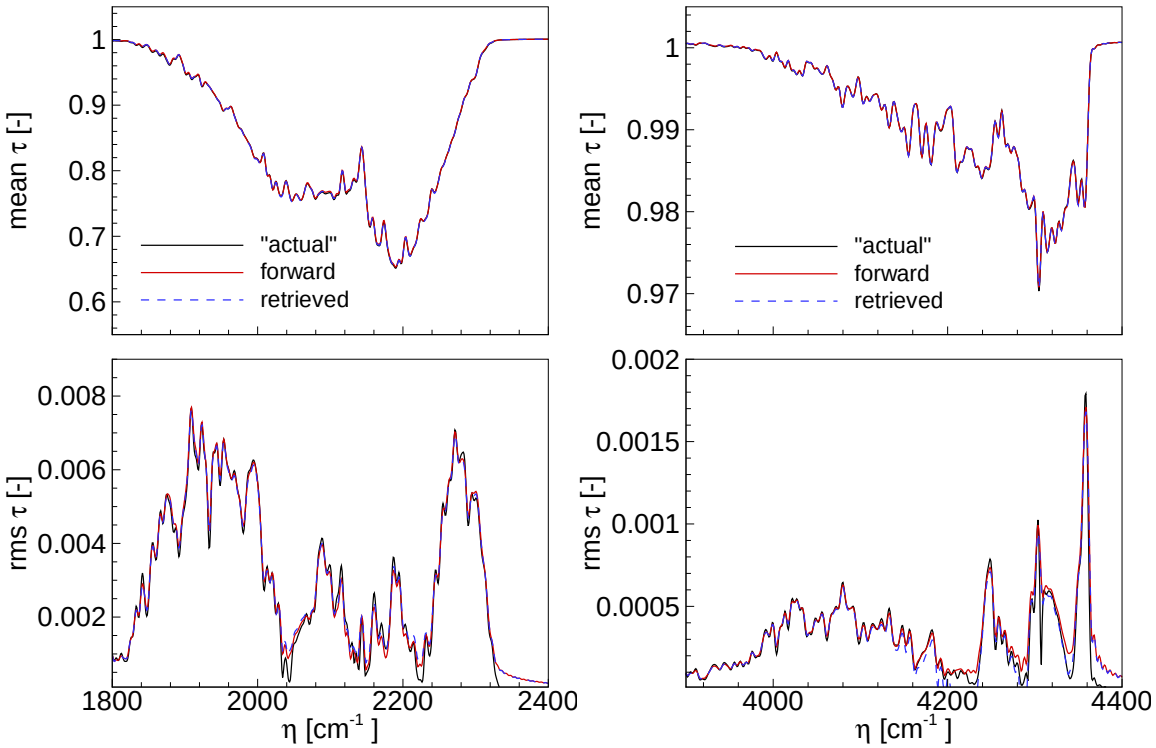

Figure 5.5: Comparison of retrieved transmissivity and its rms spectra with the "actual" spectra and forward spectra calculated by the actual turbulent scalars for the CO 4.7 μm and 2.3 μm bands

$$\left\langle \tau'^2_{\eta c} \right\rangle = g_\eta \left(\langle T \rangle, \langle x_i \rangle, \left\langle T'^2 \right\rangle, \left\langle x_i'^2 \right\rangle, \left\langle T' x_i' \right\rangle, \left\langle x_i' x_j' \right\rangle, \Lambda \right) \qquad i, j = \mathrm{CO_2}, \mathrm{H_2O}, \mathrm{CO} \tag{5.45}$$

Comparing to Eqs. (5.36) and (5.37) for a single gas species, Eqs. (5.44) and (5.45) introduces two more time-averaged species concentrations, two more variances of species concentrations, two more covariances of temperature and species concentration and three more covariances of different species concentrations. Totally, there are 15 parameters need to be retrieved.

New test cases were generated for a gas mixture assuming that the mean temperature T_0 of the gas mixture is 1500 K and mean concentration for CO_2 and H_2O are both 0.1 and mean concentration for CO is 0.05. Again, temperature and species concentrations have 10% fluctuations around the mean values. Other conditions remain the same as in the previous cases for single species. Radiation spectra for the three gases usually contain several strong bands and present at different spectral locations for different gas species. In order to retrieve these parameters accurately and efficiently, it is very important to choose appropriate spectral bands to conduct the inverse calculations. Figure 5.6 shows the spectral absorption coefficients for the three species at 1500 K. In this part of the spectrum, CO_2 has two strong bands, so does CO. For H_2O, the bands are wider and spread out over the spectrum.

Ideally, choosing part of the spectrum where all three species have overlaps can retrieve all the parameters simultaneously. For example in the spectral interval 1800 cm^{-1}– 2500 cm^{-1}, as

shown in Fig. 5.6, spectral bands for CO_2, H_2O and CO all have overlaps. However, as indicated before, this part of the spectrum contains the CO_2 4.3 μm band. Even for a single species, using this band cannot retrieve rms values for temperature and concentration very well. Our investigations show that only time-averaged values for temperature and species concentrations for the turbulent gas mixture can be retrieved relatively accurately if transmissivities at the spectral interval 1800 cm^{-1}– 2500 cm^{-1} are used. Therefore, in our study, instead of retrieving all the parameters simultaneously from the spectral interval 1800 cm^{-1}– 2500 cm^{-1}, parameters for CO_2, H_2O and their correlations are retrieved from the spectral interval 3200 cm^{-1}– 3800 cm^{-1} and the spectral interval 4200 cm^{-1}– 4400 cm^{-1} is used as supplementary band to retrieve parameters for CO. For the spectral interval 3200 cm^{-1}– 3800 cm^{-1}, CO_2 and H_2O have strong overlap, but there is no overlap with CO. That means only parameters for CO_2, H_2O and their correlations can be retrieved from this part of the spectrum. For CO, as shown in Fig. 5.6, there is a strong band within the spectral interval 4000 cm^{-1}– 4400 cm^{-1} and overlaps with H_2O, which can be used to retrieve parameters for CO. However, in the spectral interval 4000 cm^{-1}– 4200 cm^{-1}, the spectrum for H_2O is stronger than CO and make the inverse results for CO less accurate than using the spectral interval 4200 cm^{-1}– 4400 cm^{-1} to retrieve parameters for CO. So first the spectral interval 3200 cm^{-1}– 3800 cm^{-1} is used to retrieved $\langle T\rangle$, $\langle x_{CO_2}\rangle$, $\langle x_{H_2O}\rangle$, $\langle T'^2\rangle$, $\langle x'^2_{CO_2}\rangle$, $\langle x'^2_{H_2O}\rangle$, $\langle T'x'_{CO_2}\rangle$, $\langle T'x'_{H_2O}\rangle$ and Λ. Then $\langle x_{CO}\rangle$, $\langle x'^2_{CO}\rangle$ and $\langle T'x'_{CO}\rangle$ will be retrieved from the spectral interval 4200 cm^{-1}– 4400 cm^{-1}. The inverse results are shown in Table 5.3.

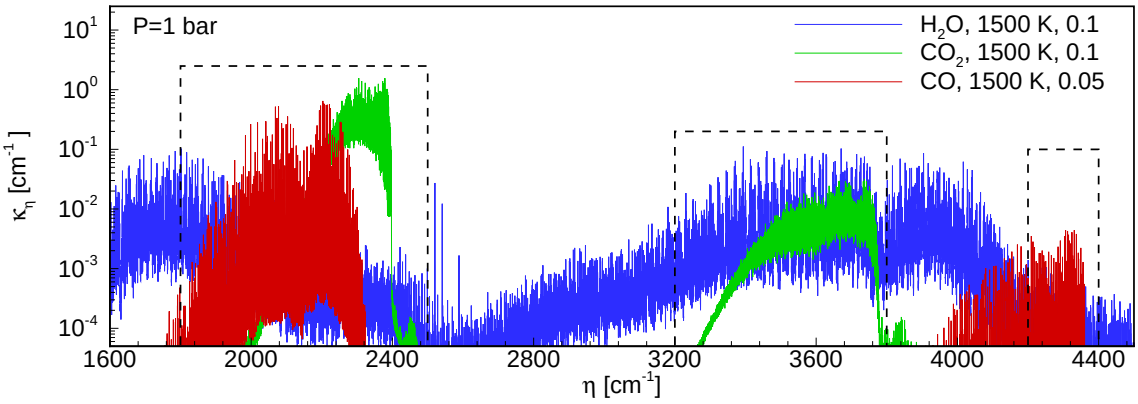

Figure 5.6: Spectral absorption coefficient for three combustion species: CO_2, H_2O and CO

In Table 5.3, there are only 12 parameters instead of 15 parameters. In previous studies for turbulent simulations and measurements [134–137], no results have been shown for correlations between species concentrations. This is one of the reasons that the results for covariances of different species are not shown here. Another reason is that we use different part of the spectrum to retrieved parameters for different species separately, covariance between two different species cannot be retrieved if there is no overlap for the emission bands of the two species, for example, $\langle x'_{CO_2}x'_{CO}\rangle$. Although, $\langle x'_{CO_2}x'_{H_2O}\rangle$ and $\langle x'_{H_2O}x'_{CO}\rangle$ can be retrieved from the spectral intervals 3200 cm^{-1}– 3800 cm^{-1} and 4200 cm^{-1}– 4400 cm^{-1}, respectively, these parameters are not interested and thus will

Table 5.3: Inverse calculation results for retrieving temperatures, species concentrations, their rms values and turbulent length scales from time-averaged transmissivity spectra and their rms spectra for a gas mixture of 10% CO_2+10% H_2O+5% CO

retrieved parameters	$\langle T \rangle$ (K)	$\langle x_{CO_2} \rangle$	$\langle x_{H_2O} \rangle$	$\langle x_{CO} \rangle$
actual values	1495.13	0.0997	0.0997	0.0498
retrieved	1492.56	0.0987	0.1005	0.0502
error(%)	−0.17	−0.96	0.84	0.65
retrieved parameters	$\sqrt{\langle T'^2 \rangle}$ (K)	$\sqrt{\langle x'^2_{CO_2} \rangle}$	$\sqrt{\langle x'^2_{H_2O} \rangle}$	$\sqrt{\langle x'^2_{CO} \rangle}$
actual values	150.83	0.0101	0.0101	0.0050
retrieved	151.3478	0.0101	0.0091	0.0049
error(%)	0.34	0.14	−9.90	−2.74
retrieved parameters	$\langle T' x'_{CO_2} \rangle$ (K)	$\langle T' x'_{H_2O} \rangle$ (K)	$\langle T' x'_{CO} \rangle$ (K)	Λ/L
actual values	1.52	1.52	0.76	0.100
retrieved	1.54	1.52	0.70	0.102
error(%)	1.25	0.32	−7.57	2.10

be neglected. Fig. 5.7 shows the comparison of retrieved transmissivity and their rms spectra with the "actual" spectra and spectra calculated from the forward calculation model for the gas mixture, agreements are very good.

5.7 Summary

An inverse radiation model was developed to reconstruct time-averaged temperature, species concentration, their rms values and the turbulence length scale from time-averaged transmissivities and their rms spectra for homogeneous gaseous media. Synthetic turbulence fields were created for temperatures and species concentrations and synthetic turbulent transmissivity spectra were created for CO_2, H_2O and CO based on the created turbulence fields. Statistical parameters from the turbulence fields and time-averaged transmissivity and rms transmissivity spectra calculated from instantaneous turbulent transmissivity spectra were used to validate the inverse radiation model. Results show that, by considering interaction between turbulence and radiation, time-averaged temperature, concentration, their rms values and turbulent length scale can be accurately retrieved from turbulent transmissivity measurements.

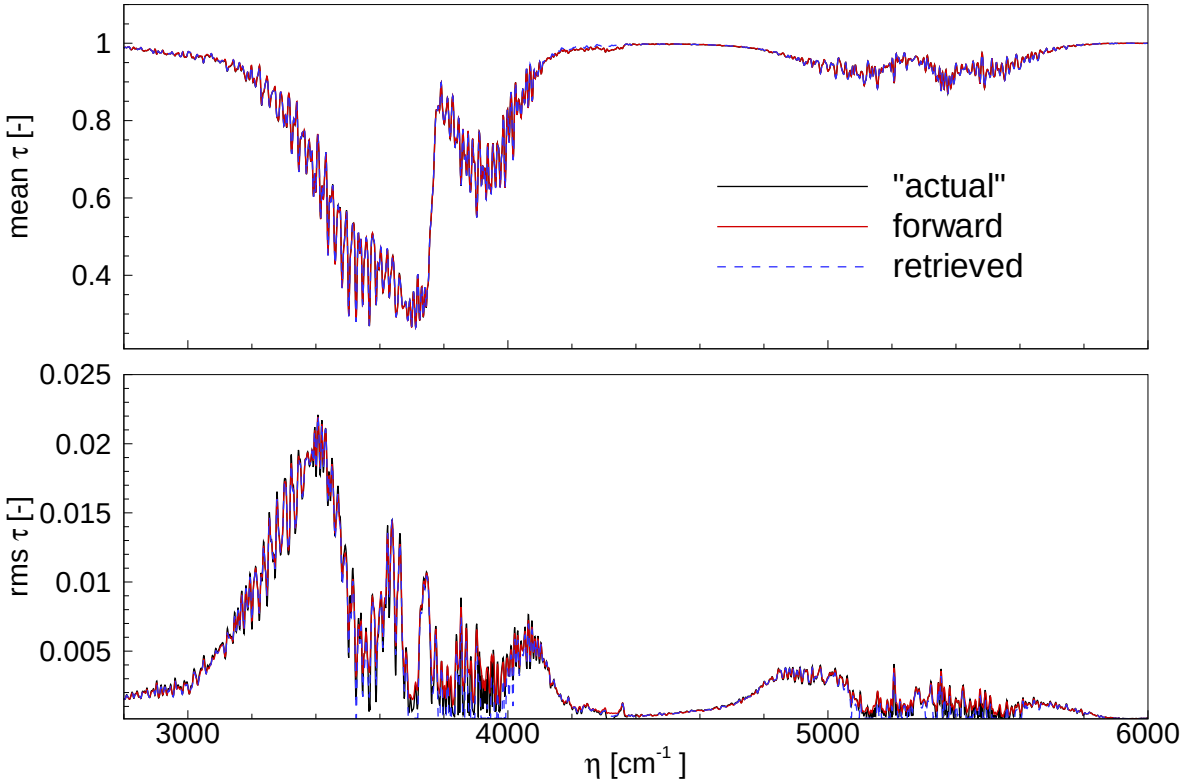

Figure 5.7: Comparison of retrieved transmissivity and its rms spectra with the “actual” spectra and forward spectra calculated by the actual turbulent scalars for a gas mixture of 10% CO_2+10% H_2O+5% CO

Chapter 6

Summary and Future Work

6.1 Concluding Remarks

The objective of the current research was to develop nonintrusive radiation tools that allow for measuring temperature and species concentrations. These tools were developed for laminar systems and, in particular, turbulent systems where turbulence-radiation interactions (TRI) can be significant. The tools naturally require the use of inverse methods, as the ultimate objective is to determine temperatures and concentrations from emitted and/or transmitted intensity measurements. Inverse radiation models were developed and these model are able to retrieve temperature and species concentrations for homogeneous laminar gaseous media, temperature profiles and average species concentrations for nonhomogeneous laminar gaseous media, and time-averaged and rms values as well as turbulent length scales for turbulent gaseous media.

In order to simulate the emission or/and transmission spectrum for combustion species, an updated absorption coefficient database was created based on the spectroscopic database HITEMP 2010 [33], which enable efficient forward calculations for the inverse radiation tools. The new absorption coefficient database contains three species, CO_2, H_2O and CO, and has tabulated data for temperatures of $300 \leq T \leq 3000$ K, total pressures of $0.1 \leq P \leq 80$ bar and species concentrations of $0.0 \leq x \leq 1.0$. An inverse radiation model was developed to retrieve temperature and species concentration for a laminar homogeneous medium, which can also be used to retrieve average temperatures and species concentrations for laminar nonhomogeneous medium. This model was validated against experimental measurements of transmissivity spectra for CO_2 and H_2O for a wide range of temperatures and species concentrations. Investigations for optimal wavenumber ranges and resolutions were conducted by considering multiple factors, including spectral region, spectral resolution, temperature and concentration range, and susceptibility to systematic and random errors. For nonhomogeneous gaseous media, it was found that transmissvities are not sensitive to temperature and concentration distributions, and, therefore emission spectra need to be used to retrieve temperature profiles. A new regularization selection method based on the theory of the discrepancy principle and the L-curve criterion was proposed and shows good generality for different temperature profiles inversion. Several types of temperature profiles were retrieved accurately using this method. It was found using two-sided measured spectra can significantly improve the results for temperature profile inversion. To develop the turbulent inverse radiation model, the nonlinear inter-

action between turbulence and radiation has to be considered. Such an inverse radiation model for a path along the detector's line-of-sight has been developed to deduce time-averaged and rms values of temperature and concentrations. This model works for single gas species as well as combustion gas mixtures and is capable of retrieving turbulent length scales from the optical measurements, as well.

6.2 Future Work

Although the developed inverse radiation tools show good capability for temperature and species retrieval for laminar and turbulent combustion system, a number of aspects need further development and closer examination.

6.2.1 Spectroscopic Database Validation

Accurate prediction of gas radiative spectra at higher temperature are one of great importance in developing inverse radiation tools. The latest spectroscopic database HITEMP 2010, as discussed earlier, was extensively tested by experimental measurements. The overall agreements are good, but our studies indicate it may be possible that there are missing hot lines for CO_2 4.3 μm at higher temperatures and also missing weak lines at the band tails for H_2O 2.7 μm band. Although for developing inverse radiation models, this shortcoming can be overcame by selecting optimal spectral ranges and resolutions, more measurements, especially at high resolution, need to be conducted to validate the HITEMP 2010 database for higher temperature gas emission predictions.

6.2.2 Experimental Validation for Laminar Nonhomogeneous Media

The inverse radiation model for the laminar homogeneous media were validated against experimentally measured transmissivities of CO_2 and H_2O, but there are no experimental data available for nonhomogeneous media. In the current research, measured spectra are synthesized from the spectroscopic database HITEMP 2010 with artificial noise. The high-temperature flow gas cell in Fig. 2.1 can be easily adapted for emission measurements of high-temperature gases with nonuniform temperatures and concentrations. Temperature or concentration variations can be introduced along the gas cell. Unlike transmissities, which are the ratio representing the percentages of how much incoming light transmitted through the gas layer, emitted intensities from the high-temperature gas are absolute values. The intensity measurements have to be carefully calibrated against blackbody emission by a blackbody calibrator.

6.2.3 Experimental Validation for Turbulent Media

The developed inverse radiation model for turbulent gaseous media were validated by analytical "experiments" in the current research. Instantaneous scalar fields were generated to create instantaneous temperature and concentration fields. "Measured" turbulent transmissvities and their rms spectra were synthesized by these fields. By measuring gas column transmissivities in turbulent gas-mixture channel flows and combustion system, this model can be validated by experimental measurements.

6.2.4 Multi-Dimensional Inversion Techniques

The emphasis of the current research was to develop optimal spectral tools to retrieve temperature and species concentration and turbulence moments from a set of line-of-sight radiometric measurements. Based on what has been done for nonhomogeneous laminar gaseous media, multi-dimensional reconstructions on a laminar flow field can be achieved. Similar approaches can be used to determine optimal spectral bands and resolution. In principle, the flow field can be reconstructed based on several line-of-sight measurements with proper spatial resolution. However, there are constraints within line-of-sight measurements. If these constraints can be applied, topographical reconstruction of the flow field will be much easier and accurate.

6.2.5 Turbulent Inverse Radiation Model Based on Emission Measurements

The turbulent inverse radiation model was based on transmissivity measurements of a homogeneous turbulence system. It is capable of retrieving time-averaged and rms values accurately for temperature and concentration without invoking the OTFA. In order to extend the model to nonhomogeneous turbulent systems, it is important to develop inverse radiation tools based on turbulent emission measurements. However, accurate prediction of emission from a turbulent combustion gases requires accurate modeling of the correlation between local instantaneous radiation along the optical path and local absorption coefficient [115], which is a rather difficult challenge. The OTFA implies that this correlation can be neglected for not very strong spectral lines. Therefore, investigation can be done to study the accuracy of applying the OTFA for predicting turbulent time-averaged emission and their rms values for different combustion species and different spectral bands. An optimal spectral band should be selected afterwards; similar inverse calculation algorithm as in the laminar models can be applied to retrieve time-averaged and rms scale values for nonhomogeneous turbulent systems.

6.2.6 Multi-species Inversion Techniques

Although the current studies show the capability of retrieving temperature and species concentrations for gas mixture of major combustion species (CO_2, H_2O and CO), detection of concentrations for other minor species is also important. The concentrations for the minor species, for example, OH, NO_x and SO_x, are good indicator for the completeness of combustion and pollution control, which is critical for developing next-generation of clean and efficient combustion systems. The latest HITRAN database, HITRAN2012 [34], contains spectroscopic data for 47 gas species. Studies should be conducted to investigate the capability of retrieving temperature and species concentrations with this spectroscopic database and the developed inverse radiation models.

6.2.7 Improve Computational Efficiency

The current studies focus on investigating the capability of retrieving scalars from laminar or turbulent radiation measurements. The uncertainties of the solution mainly come from theoretical uncertainties of the forward calculation model (due to assumptions made and the accuracy of the spectroscopic database). Other uncertainties of the retrieved parameters have been artificially

reduced by using sufficient spectral data from wide spectral bands, which also makes the inverse calculation artificially “slow”. Currently, it takes few seconds to retrieve these parameters for a homogeneous gas medium (laminar or turbulent) and takes few minutes to retrieve parameter profiles for non-homogeneous gas medium. Computational efficiency can be significantly improved if less spectral data in the most active part of the spectrum within a spectral band are used to retrieve temperatures and species concentrations.

Bibliography

[1] H. C. Hottel, F. P. Broughton, Determination of true temperature and total radiation from luminous gas flames, Industrial and Engineering Chemistry 4 (1932) 166–174.

[2] D. R. Snelling, K. A. Thomson, G. J. Smallwood, O. L. Gülder, E. J. Weckman, R. A. Fraser, Spectrally resolved measurement of flame radiation to determine soot temperature and concentration, AIAA J 40 (9) (1969) 1789–1795.

[3] S. Strner, R. Bilger, R. Dibble, R. Barlow, Some raman/rayleigh/lif measurements in turbulent propane flames, in: Symposium (International) on Combustion, Vol. 23, Elsevier, 1991, pp. 645–651.

[4] R. Barlow, C. Carter, Raman/rayleigh/lif measurements of nitric oxide formation in turbulent hydrogen jet flames, Combustion and Flame 97 (3) (1994) 261–280.

[5] A. Masri, R. Dibble, R. Barlow, The structure of turbulent nonpremixed flames revealed by raman-rayleigh-lif measurements, Progress in Energy and Combustion Science 22 (4) (1996) 307–362.

[6] P. Nooren, M. Versluis, T. H. van der Meer, R. Barlow, J. Frank, Raman-rayleigh-lif measurements of temperature and species concentrations in the delft piloted turbulent jet diffusion flame, Applied Physics B 71 (1) (2000) 95–111.

[7] W. Meier, R. Barlow, Y.-L. Chen, J.-Y. Chen, Raman/rayleigh/lif measurements in a turbulent $ch_4/h_2/n_2$ jet diffusion flame: experimental techniques and turbulence–chemistry interaction, Combustion and Flame 123 (3) (2000) 326–343.

[8] R. Cabra, T. Myhrvold, J. Chen, R. Dibble, A. Karpetis, R. Barlow, Simultaneous laser raman-rayleigh-lif measurements and numerical modeling results of a lifted turbulent h_2/n_2 jet flame in a vitiated coflow, Proceedings of the Combustion Institute 29 (2) (2002) 1881–1888.

[9] R. S. Barlow, G.-H. Wang, P. Anselmo-Filho, M. Sweeney, S. Hochgreb, Application of raman/rayleigh/lif diagnostics in turbulent stratified flames, Proceedings of the Combustion Institute 32 (1) (2009) 945–953.

[10] A. C. Eckberth, Laser diagnostics for combustion temperature and species, Vol. 3, CRC Press, 1996.

[11] J. M. Seitzman, G. Kychakoff, R. K. Hanson, Instantaneous temperature field measurements using planar laser-induced fluorescence, Optics letters 10 (9) (1985) 439–441.

[12] S. Bejaoui, X. Mercier, P. Desgroux, E. Therssen, Laser induced fluorescence spectroscopy of aromatic species produced in atmospheric sooting flames using uv and visible excitation wavelengths, Combustion and Flame 161 (10) (2014) 2479–2491.

[13] B. Li, Y. He, Z. Li, A. A. Konnov, Measurements of no concentration in nh 3-doped ch 4+ air flames using saturated laser-induced fluorescence and probe sampling, Combustion and Flame 160 (1) (2013) 40–46.

[14] R. Santoro, H. Semerjian, R. Dobbins, Soot particle measurements in diffusion flames, Combust Flame 51 (1983) 203–218.

[15] J. H. Kent, D. Honnery, Modeling sooting turbulent jet flames using an extended flamelet technique, Combust Sci Technol 54 (1987) 383–397.

[16] L. Wang, N. E. Endrud, S. R. Turns, M. D. D'Agostini, A. G. Slavejkov, A study of the influence of oxygen index on soot, radiation, and emission characteristics of turbulent jet flames, Combust Sci Technol 178 (8) (2002) 45–72.

[17] K. L. Cashdollar, Three-wavelength pyrometer for measuring flame temperatures, Applied Optics 18 (15) (1979) 2595–2597.

[18] S. M. Hwang, R. Kurose, F. Akamatsu, H. Tsuji, H. Makino, M. Katsuki, Application of optical diagnostics techniques to a laboratory-scale turbulent pulverized coal flame, Energy and Fuels 19 (2005) 382–392.

[19] J. Cai, M. Handa, M. F. Modest, Eulerian–eulerian multi-fluid methods for pulverized coal flames with nongray radiation, Combustion and Flame.

[20] N. Chigier, Combustion measurements, CRC Press, 1991.

[21] F. Fuest, R. S. Barlow, J.-Y. Chen, A. Dreizler, Raman/rayleigh scattering and co-lif measurements in laminar and turbulent jet flames of dimethyl ether, Combustion and Flame 159 (8) (2012) 2533–2562.

[22] A. Sevault, M. Dunn, R. S. Barlow, M. Ditaranto, On the structure of the near field of oxy-fuel jet flames using raman/rayleigh laser diagnostics, Combustion and Flame 159 (11) (2012) 3342–3352.

[23] F. LaPlant, G. Laurence, D. Ben-Amotz, Theoretical and experimental uncertainty in temperature measurement of materials by raman spectroscopy, Applied spectroscopy 50 (8) (1996) 1034–1038.

[24] P. Childs, J. Greenwood, C. Long, Review of temperature measurement, Review of scientific instruments 71 (8) (2000) 2959–2978.

[25] G. Bianchini, U. Cortesi, L. Palchetti, Emission fourier transform spectroscopy for the remote sensing of the atmosphere, Optics and Lasers in Engineering 37 (2002) 187–202.

[26] A. Soufiani, J.-P. Martin, J.-C. Rolon, L. Brenez, Sensitivity of temperature and concentration measurements in hot gases from ftir emission spectroscopy, J Quant Spectrosc Radiat Transf 73 (2002(2–5)) 317–327.

[27] L. A. Kranendonk, A. W. Caswell, S. T. Sanders, Robust method for calculating temperature, pressure, and absorber mole fraction from broadband spectra, Applied optics 46 (19) (2007) 4117–4124.

[28] R. J. Hall, P. A. Bonczyk, Sooting flame thermometry using emission/absorption tomography, Applied optics 29 (31) (1990) 4590–4598.

[29] H. Uchiyama, M. Nakajima, S. Yuta, Measurement of flame temperature distribution by ir emission computed tomography, Applied optics 24 (23) (1985) 4111–4116.

[30] I. Ayrancı, R. Vaillon, N. Selçuk, F. André, D. Escudié, Determination of soot temperature, volume fraction and refractive index from flame emission spectrometry, J Quant Spectrosc Radiat Transf 104 (2) (2007) 266–276.

[31] I. Ayrancı, R. Vaillon, N. Selçuk, Near-infrared emission spectrometry measurements for nonintrusive soot diagnostics in flames, Journal of Quantitative Spectroscopy and Radiative Transfer 109 (2) (2008) 349–361.

[32] L. S. Rothman, I. E. Gordon, A. Barbe, D. C. Benner, P. F. Bernath, M. Birk, V. Boudon, L. R. Brown, A. Campargue, J.-P. Champion, K. Chance, L. H. Coudert, V. Dana, V. M. Devi, S. Fally, J.-M. Flaud, R. R. Gamache, A. Goldman, D. Jacquemart, I. Kleiner, N. Lacome, W. J. Lafferty, J.-Y. Mandin, S. T. Massie, S. N. Mikhailenko, C. E. Miller, N. Moazzen-Ahmadi, O. V. Naumenko, A. V. Nikitin, J. Orphal, V. I. Perevalov, A. Perrin, A. Predoi-Cross, C. P. Rinsland, M. Rotger, M. Simeckova, M. A. H. Smith, K. Sung, S. A. Tashkun, J. Tennyson, R. A. Toth, A. C. Vandaele, J. V. Auwera, The HITRAN 2008 molecular spectroscopic database, J Quant Spectrosc Radiat Transf 110 (2009) 533–572.

[33] L. S. Rothman, I. E. Gordon, R. J. Barber, H. Dothe, R. R. Gamache, A. Goldman, V. I. Perevalov, S. A. Tashkun, J. Tennyson, HITEMP, the high-temperature molecular spectroscopic database, J Quant Spectrosc Radiat Transf 111 (15) (2010) 2139–2150.

[34] L. Rothman, I. Gordon, Y. Babikov, A. Barbe, D. C. Benner, P. Bernath, M. Birk, L. Bizzocchi, V. Boudon, L. Brown, et al., The HITRAN2012 molecular spectroscopic database, Journal of Quantitative Spectroscopy and Radiative Transfer 130 (2013) 4–50.

[35] M. Abu-Romia, C. L. Tien, Appropriate mean absorption coefficients for infrared radiation of gases, Journal of Heat Transfer 89 (4) (1967) 321–327.

[36] C. Ludwig, W. Malkmus, J. Reardon, J. Thomson, R. Goulard, Handbook of infrared radiation from combustion gases. nasa sp-3080, NASA Special Publication 3080.

[37] T. Smith, Z. Shen, J. Friedman, Evaluation of coefficients for the weighted sum of gray gases model, Journal of Heat Transfer 104 (4) (1982) 602–608.

[38] M. F. Modest, Radiative Heat Transfer, 3rd Edition, Academic Press, New York, 2013.

[39] R. J. Anderson, P. R. Griffiths, Determination of rotational temperatures of diatomic molecules from absorption spectra measured at moderate resolution, J Quant Spectrosc Radiat Transf 17 (1977) 393–401.

[40] L. A. Gross, P. R. Griffiths, Temperature estimation of carbon dioxide by infrared absorption spectrometry at medium resolution, J Quant Spectrosc Radiat Transf 39 (2) (1988) 131–138.

[41] R. J. Anderson, P. R. Griffiths, Errors in absorbance measurements in infrared Fourier transform spectrometry because of limited instrument resolution, Analytical Chemistry 47 (14) (1975) 2339–2347.

[42] P. R. Solomon, P. E. Best, R. M. Carangelo, J. R. Markham, P.-L. Chien, R. J. Santoro, H. G. Semerjian, Ft-ir emission/transmission spectroscopy for in situ combustion diagnostics, Proc Comb Inst 21 (1987) 1763–1771.

[43] P. E. Best, P. L. Chien, R. M. Carangelo, P. R. Solomon, M. Danchak, I. Ilovici, Tomographic reconstruction of ft-ir emission and transmission spectra in a sooting laminar diffusion flame: Species concentrations and temperatures, Combust Flame 85 (1991) 309–314.

[44] L. S. Rothman, R. R. Gamache, R. H. Tipping, C. P. Rinsland, M. A. H. Smith, D. C. Benner, V. M. Devi, J.-M. Flaud, C. Camy-Peyret, A. Perrin, A. Goldman, S. T. Massie, L. R. Brown, R. A. Toth, The HITRAN molecular database: Editions of 1991 and 1992, J Quant Spectrosc Radiat Transf 48 (5/6) (1992) 469–507.

[45] L. S. Rothman, C. P. Rinsland, A. Goldman, S. T. Massie, D. P. Edwards, J.-M. Flaud, A. Perrin, C. Camy-Peyret, V. Dana, J.-Y. Mandin, J. Schroeder, A. McCann, R. R. Gamache, R. B. Wattson, K. Yoshino, K. V. Chance, K. W. Jucks, L. R. Brown, V. Nemtchinov, P. Varanasi, The HITRAN molecular spectroscopic database and HAWKS (HITRAN atmospheric workstation): 1996 edition, J Quant Spectrosc Radiat Transf 60 (1998) 665–710.

[46] L. S. Rothman, A. Barbe, D. C. Benner, L. R. Brown, C. Camy-Peyret, M. R. Carleer, K. Chance, C. Clerbaux, V. Dana, V. M. Devi, A. Fayt, J.-M. Flaud, R. R. Gamache, A. Goldman, D. Jacquemart, K. W. Jucks, W. J. Lafferty, J.-Y. Mandin, S. Massie, V. Nemtchinov, D. Newnham, A. Perrin, C. P. Rinsland, J. Schroeder, K. M. Smith, M. A. H. Smith, K. Tang, R. A. Toth, J. V. Auwera, P. Varanasi, K. Yoshino, The HITRAN spectroscopic molecular database: Edition of 2000 including updates through 2001, J Quant Spectrosc Radiat Transf 82 (1–4) (2003) 5–44.

[47] L. S. Rothman, D. Jacquemart, A. Barbe, D. C. Benner, M. Birk, L. R. Brown, M. R. Carleer, C. Chackerian, Jr., K. Chance, L. H. Coudert, V. Dana, V. M. Devi, J.-M. Flaud, R. R. Gamache, A. Goldman, J.-M. Hartmann, K. W. Jucks, A. G. Maki, J.-Y. Mandin, S. T. Massie, J. Orphal, A. Perrin, C. P. Rinsland, M. A. H. Smith, J. Tennyson, R. N. Tolchenov, R. A. Toth, J. V. Auwera, P. Varanasi, G. Wagner, The HITRAN 2004 molecular spectroscopic database, J Quant Spectrosc Radiat Transf 96 (2005) 139–204.

[48] M. Hilton, A. H. Lettington, I. M. Mills, Quantitative-analysis of remote gas temperatures and concentrations from their infrared-emission spectra, Measurement Science & Technology 6 (9) (1995) 1236–1241.

[49] M. Hilton, A. H. Lettington, C. W. Wilson, Gas turbine exhaust emissions monitoring using nonintrusive infrared spectroscopy, ASME Journal of Engineering for Gas Turbines and Power 120 (3) (1998) 514–518.

[50] F. Yousefian, M. Lallemand, Inverse radiative analysis of high-resolution infrared emission data for temperature and species profiles recoveries in axisymmetric semi-transparent media, J Quant Spectrosc Radiat Transf 60 (6) (1998) 921–931.

[51] F. Yousefian, M. Sakami, M. Lallemand, Recovery of temperature and species concentration profiles in flames using low-resolution infrared spectroscopy, ASME J Heat Transfer 121 (2) (1999) 268–279.

[52] C. F. Mallery, S. T. Thynell, Line-of-sight temperature and species profiles determined from spectral transmittances, J Thermoph Heat Transfer 11 (3) (1997) 367–374.

[53] C. F. Mallery, S. T. Thynell, Line-of-sight variations of temperature and species in solid propellant flames, Journal of Propulsion and Power 16 (3) (2000) 505–512.

[54] H. H. Richardson, V. W. Pabst, J. A. Butcher, A novel infrared spectrometer using a linear array detector, Appl Spectr 44 (5) (1990) 822–825.
URL http://as.osa.org/abstract.cfm?URI=as-44-5-822

[55] S. M. Alawi, T. Krug, H. H. Richardson, Characterization and application of an infrared linear array spectrometer for time-resolved infrared spectroscopy, Appl Spectr 47 (10) (1993) 1626–1630.
URL http://as.osa.org/abstract.cfm?URI=as-47-10-1626

[56] B. A. Rankin, G. Magnotti, R. S. Barlow, J. P. Gore, Radiation intensity imaging measurements of methane and dimethyl ether turbulent nonpremixed and partially premixed jet flames, Combustion and Flame 161 (11) (2014) 2849–2859.

[57] B. A. Rankin, M. Ihme, J. P. Gore, Quantitative model-based imaging of mid-infrared radiation from a turbulent nonpremixed jet flame and plume, Combustion and Flame.

[58] J. L. Harley, B. A. Rankin, D. L. Blunck, J. P. Gore, K. C. Gross, Imaging fourier-transform spectrometer measurements of a turbulent nonpremixed jet flame, Optics letters 39 (8) (2014) 2350–2353.

[59] P. R. Griffiths, B. L. Hirsche, C. J. Manning, Ultra-rapid-scanning fourier transform infrared spectrometry, Vibrational Spectroscopy 19 (1) (1999) 165–176.

[60] G. D. Smith, R. A. Palmer, Fast time-resolved mid-infrared spectroscopy using an interferometer, Handbook of vibrational spectroscopy.

[61] J. Ji, J. P. Gore, Y. R. Sivathanu, J. Lim, Fast infrared array spectrometer with a thermoelectrically cooled 160-element pbse detector, Review of scientific instruments 75 (2) (2004) 333–339.

[62] A. J. Ricks, T. K. Blanchat, Hydrocarbon characterization experiments in fully turbulent fires, SANDIA Report, SAND2007-2391, Albuquerque, New Mexico.

[63] J. M. Suo-Anttila, T. K. Blanchat, A. J. Ricks, A. L. Brown, Characterization of thermal radiation spectra in 2m pool fires, Proceedings of the Combustion Institute 32 (2) (2009) 2567–2574.

[64] J. M. Suo-Anttila, T. K. Blanchat, Hydrocarbon characterization experiments in fully turbulent fires: results and data analysis., Tech. rep., Sandia National Laboratories (2011).

[65] Y. Zheng, R. S. Barlow, J. P. Gore, Spectral radiation properties of partially premixed turbulent flames, ASME J Heat Transfer 125 (2003) 1065–1073.

[66] Y. Zheng, R. S. Barlow, J. P. Gore, Measurements and calculations of spectral radiation intensities for turbulent non-premixed and partially premixed flames, ASME J Heat Transfer 125 (2003) 678–686.

[67] Y. Zheng, J. P. Gore, Measurements and inverse calculations of spectral radiation intensities of a turbulent ethylene/air jet flame, in: Thirtieth Symposium (International) on Combustion, The Combustion Institute, 2005, pp. 727–734.

[68] S. A. Tashkun, V. I. Perevalov, Carbon dioxide spectroscopic databank (CDSD): updated and enlarged version for atmospheric applications, in: Tenth HITRAN conference, Cambridge, MA; Paper T2.3, 2008, available from ftp://ftp.iao.ru/pub/CDSD-2008.

[69] M. F. Modest, S. P. Bharadwaj, High-resolution, high-temperature transmissivity measurements and correlations for carbon dioxide–nitrogen mixtures, J Quant Spectrosc Radiat Transf 73 (2–5) (2002) 329–338.

[70] S. P. Bharadwaj, M. F. Modest, Medium resolution transmission measurements of CO_2 at high temperature – an update, J Quant Spectrosc Radiat Transf 103 (2007) 146–155.

[71] V. Evseev, A. Fateev, S. Clausen, High-resolution transmission measurements of CO_2 at high temperatures for industrial applications, J Quant Spectrosc Radiat Transf 113 (2012) 2222–2233.

[72] S. P. Bharadwaj, M. F. Modest, R. J. Riazzi, Medium resolution transmission measurements of water vapor at high temperature, ASME J Heat Transfer 128 (2006) 374–381.

[73] A. Fateev, S. Clausen, On-line non-contact gas analysis, Danmarks Tekniske Universitet, Risø Nationallaboratoriet for Bæredygtig Energi, 2008.

[74] A. D. Klose, U. Netz, J. Beuthan, A. H. Hielscher, Optical tomography using the time-independent equation of radiative transfer — part 1: forward model, J Quant Spectrosc Radiat Transf 72 (2002) 691–713.

[75] A. D. Klose, A. H. Hielscher, Optical tomography using the time-independent equation of radiative transfer — part 2: Inverse model, J Quant Spectrosc Radiat Transf 72 (2002) 715–732.

[76] A. Charette, J. Boulanger, H. K. Kim, An overview on recent radiation transport algorithm development for optical tomography imaging, J Quant Spectrosc Radiat Transf 109(17-18) (2008) 2743–2766.

[77] J. Nocedal, S. J. Wright, Numerical optimization, 2nd Edition, Springer Verlag, Berlin, 2006.

[78] W. H. Press, S. A. Teukolsky, W. T. Vetterling, B. P. Flannery, Numerical Recipies in FORTRAN – The Art of Scientific Computing, 2nd Edition, Cambridge University Press, Cambridge, 1992.

[79] P. J. Hommert, R. Viskanta, A. M. Mellor, Flame temperature measurements by spectral remote sensing, Combust Flame 30 (1977) 295–308.

[80] P. Hommert, R. Viskanta, High temperature gas diagnostics by spectral remote sensing, International Journal of Heat and Mass Transfer 21 (6) (1978) 769–781.

[81] J. Lim, Y. Sivathanu, J. Ji, J. Gore, Estimating scalars from spectral radiation measurements in a homogeneous hot gas layer, Combust Flame 137 (2004) 222–229.

[82] W. L. Grosshandler, Radiative transfer in nonhomogeneous gases: A simplified approach, Intl J Heat Mass Transfer 23 (1980) 1447–1457.

[83] J. Ji, Experimental and theoretical study of the spectral radiation characteristics of lean premixed flames, Ph.D. thesis, Purdue University, West Lafayette, IN (2000).

[84] D. R. Buchele, Computer program for calculation of a gas temperature profile by infrared emission: Absorption spectroscopy, NASA-TM-73848.

[85] S.-W. Woo, T.-H. Song, Measurement of gas temperature profile using spectral intensity from co_2 4.3 μm band, International journal of thermal sciences 41 (9) (2002) 883–890.

[86] H. K. Kim, T.-H. Song, Characteristics of srs inversion for measurement of temperature and co_2 concentration profile of a combustion gas layer, J Quant Spectrosc Radiat Transf 86 (2) (2004) 181–199.

[87] H. K. Kim, T.-H. Song, Determination of the gas temperature profile in a large-scale furnace using a fast/efficient inversion scheme for the SRS technique, J Quant Spectrosc Radiat Transf 93 (2005) 369–381.

[88] T.-H. Song, Spectral remote sensing for furnaces and flames, Heat Transfer Engineering 29 (4) (2008) 417–428.

[89] S.-S. Yang, T.-H. Song, An improved wsggm-based narrow band model for the co 2 4.3 μm band, International journal of thermal sciences 38 (3) (1999) 228–238.

[90] C. J. Dash, One-dimensional tomography: a comparison of abel, onion-peeling, and filtered backprojection methods, Appl Opt 31 (1992) 1146–1152.

[91] K. J. Daun, K. A. Thomson, F. Liu, G. J. Smallwood, Deconvolution of axisymmetric flame properties using tikhonov regularization, Appl Opt 45 (2006) 4638–4646.

[92] E. O. Åkesson, K. J. Daun, Parameter selection methods for axisymmetric flame tomography through tikhonov regularization, Appl Opt 47 (2008) 407–416.

[93] N. Terzija, J. L. Davidson, C. A. Garcia-Stewart, P. Wright, K. B. Ozanyan, S. Pegrum, T. J. Litt, H. McCann, Quantitative-analysis of remote gas temperatures and concentrations from their infrared-emission spectra, Measurement Science & Technology 19 (2008) 09400.

[94] A. A. Townsend, The effects of radiative transfer on turbulent flow of a stratified fluid, J Fluid Mech 4 (1958) 361–375.

[95] T.-H. Song, R. Viskanta, Interaction of radiation with turbulence: Application to a combustion system, J Thermoph Heat Transfer 1 (1987) 56–62.

[96] A. Soufiani, P. Mignon, J. Taine, Radiation–turbulence interaction in channel flows of infrared active gases, in: Proceedings of the International Heat Transfer Conference, Vol. 6, ASME, 1990, pp. 403–408.

[97] R. J. Hall, A. Vranos, Efficient calculations of gas radiation from turbulent flames, Intl J Heat Mass Transfer 37 (17) (1994) 2745–2750.

[98] S. Tieszen, On the fluid mechanics of fires, Ann. Rev. Fluid Mech. 33 (2001) 67–92.

[99] S. M. Jeng, M. C. Lai, G. M. Faeth, Nonluminous radiation in turbulent buoyant axisymmetric flames, Combust Sci Technol 40 (1984) 41–53.

[100] J. P. Gore, G. M. Faeth, Structure and spectral radiation properties of turbulent ethylene/air diffusion flames, in: Proceedings of the Twenty-First Symposium (International) on Combustion, 1986, pp. 1521–1531.

[101] J. P. Gore, S. M. Jeng, G. M. Faeth, Spectral and total radiation properties of turbulent carbon monoxide/air diffusion flames, AIAA J 25 (2) (1987) 339–345.

[102] J. P. Gore, S. M. Jeng, G. M. Faeth, Spectral and total radiation properties of turbulent hydrogen/air diffusion flames, ASME J Heat Transfer 109 (1987) 165–171.

[103] M. E. Kounalakis, J. P. Gore, G. M. Faeth, Turbulence/radiation interactions in nonpremixed hydrogen/air flames, in: Twenty-Second Symposium (International) on Combustion, The Combustion Institute, 1988, pp. 1281–1290.

[104] M. E. Kounalakis, J. P. Gore, G. M. Faeth, Mean and fluctuating radiation properties of nonpremixed turbulent carbon monoxide/air flames, ASME J Heat Transfer 111 (1989) 1021–1030.

[105] Y. R. Sivathanu, M. E. Kounalakis, G. M. Faeth, Soot and continuous radiation statistics of luminous turbulent diffusion flames, in: Twenty-Third Symposium (International) on Combustion, The Combustion Institute, 1990, pp. 1543–1550.

[106] M. Klassen, Y. R. Sivathanu, J. P. Gore, Simultaneous emission absorption-measurements in toluene-fueled pool flames – mean and rms properties, Combust Flame 90 (1992) 34–44.

[107] Y. R. Sivathanu, J. P. Gore, Transient structure and radiation properties of strongly radiating buoyant flames, ASME J Heat Transfer 114 (1992) 659–665.

[108] D. L. Blunck, M. E. H. C. L. Merkle, J. P. Gore, Influence of turbulent fluctuations on the radiation intensity emitted from exhaust plumes, J Thermoph Heat Transfer 26 (4) (2012) 581–589.

[109] D. Blunck, M. Harvazinski, B. Rankin, C. Merkle, J. Gore, Turbulent radiation statistics of exhaust plumes exiting from a subsonic axisymmetric nozzle, J Thermoph Heat Transfer 26 (2) (2012) 286–293.

[110] S. Mazumder, M. F. Modest, PDF modeling of turbulence radiation interactions, in: 1997 National Heat Transfer Conference, Baltimore, MD, ASME, 1997.

[111] S. Mazumder, M. F. Modest, Turbulence–radiation interactions in nonreactive flow of combustion gases, ASME J Heat Transfer 121 (1999) 726–729.

[112] G. Li, M. F. Modest, A PDF method to capture sharp gradients in turbulent heat transfer, in: Proceedings of the 2000 National Heat Transfer Conference, ASME, Pittsburgh, PA, 2000.

[113] G. Li, M. F. Modest, Application of composition PDF methods in the investigation of turbulence–radiation interactions, J Quant Spectrosc Radiat Transf 73 (2002) 461–472.

[114] A. Gupta, D. C. Haworth, M. F. Modest, Turbulence-radiation interactions in large-eddy simulations of luminous and nonluminous nonpremixed flames, Proc Comb Inst 34 (2013) 1281–1288.

[115] P. J. Coelho, Numerical simulation of the interaction between turbulence and radiation in reactive flows, Progr Energy Combust Sci 33 (4) (2007) 311–383.

[116] V. P. Kabashinikov, G. I. Myasnikova, Thermal radiation in turbulent flows—temperature and concentration fluctuations, Heat Transfer-Soviet Research 17 (6) (1985) 116–125.

[117] J. Y. Ko, H. K. Kim, T.-H. Song, Inversion of combustion gas temperature/concentration profile with radiation/turbulence interaction using SRS, J Quant Spectrosc Radiat Transf 110 (13) (2009) 1199–1206.

[118] P. Foster, Relation of time-mean transmission of turbulent flames to optical depth, Journal of the Institute of Fuel 42 (340) (1969) 179.

[119] P. R. Griffiths, J. A. de Haseth, Fourier Transform Infrared Spectrometry, Vol. 83 of Chemical Analysis, John Wiley & Sons, New York, 1986.

[120] T. A. Reeder, M. F. Modest, Instrument lineshape analysis for a low-resolution FTIR spectrometer, in: Paper No. HT2012-58365, Proceedings of the 2012 ASME Summer Heat Transfer Conference, Rio Grande, Puerto Rico, 2012.

[121] T. Ren, M. F. Modest, Temperature profile inversion from CO_2 spectral intensities through levenberg-marquardt optimization and tikhonov regularization, in: Paper No.1896725, 11th AIAA/ASME Joint Thermophysics and Heat Transfer Conference, Atlanta, GA, 2014.

[122] T. Ren, M. F. Modest, A. Fateev, S. Clausen, An inverse radiation model for optical determination of temperature and species concentration: development and validation, J Quant Spectrosc Radiat Transf 151 (0) (2015) 198–209.

[123] Hamilton company.
URL http://www.hamiltoncompany.com/item/view/c/785/p/1350/

[124] S. P. Bharadwaj, Medium resolution transmission measurements of CO_2 and H_2O at high temperature and a multiscale Malkmus model for treatment of inhomogeneous gas paths, Ph.D. thesis, The Pennsylvania State University, Department of Mechanical Engineering, University Park, PA (2005).

[125] A. Fateev, personal communication (2013-12-16).

[126] H. W. Engl, W. Grever, Using the l–curve for determining optimal regularization parameters, Numerische Mathematik 69 (1) (1994) 25–31.

[127] O. Scherzer, The use of morozov's discrepancy principle for tikhonov regularization for solving nonlinear ill-posed problems, Computing 51 (1) (1993) 45–60.

[128] T. Viklands, M. Gulliksson, Optimization tools for solving nonlinear ill-posed problems, in: Fast Solution of Discretized Optimization Problems, Springer, 2001, pp. 255–264.

[129] F. Kritzstein, A. Soufiani, Infrared gas radiation from a homogeneously turbulent medium, Intl J Heat Mass Transfer 36 (7) (1993) 1749–1762.

[130] L. Soucasse, P. Rivière, A. Soufiani, Subgrid-scale model for radiative transfer in turbulent participating media, J Comp Phys 257 (2014) 442–459.

[131] Y. Talmi, R. Simpson, Self-scanned photodiode array: a multichannel spectrometric detector, Applied Optics 19 (9) (1980) 1401–1414.

[132] S. B. Pope, Turbulent Flows, Cambridge University Press, Cambridge, 2000.

[133] C. B. da Silva, I. Malico, P. J. Coelho, Radiation statistics in homogeneous isotropic turbulence, New Journal of Physics 11 (9) (2009) 093001.

[134] R. S. Barlow, International workshop on measurement and computation of turbulent nonpremixed flames (TNF), website: http://www.sandia.gov/TNF/abstract.html.

[135] M. R. H. Sheikhi, T. G. Drozda, P. Givi, F. A. Jaberi, S. B. Pope, Large eddy simulation of a turbulent nonpremixed piloted methane jet flame (Sandia Flame D), Proceedings of The Combustion Institute 30 (2005) 549–556.

[136] R. Mustata, L. Valiño, C. Jiménez, W. Jones, S. Bondi, A probability density function eulerian monte carlo field method for large eddy simulations: application to a turbulent piloted methane/air diffusion flame (Sandia D), Combustion and Flame 145 (1) (2006) 88–104.

[137] W. Jones, V. Prasad, Large eddy simulation of the Sandia flame series (D–F) using the Eulerian stochastic field method, Combustion and Flame 157 (9) (2010) 1621–1636.